

Initial steady-state core simulation capability for thermal and pool-type molten salt reactors, coupling reactor physics, thermal-hydraulics, and evolving chemistry

INL/RPT-25-88048
Revision 0

M2 Report

SEPTEMBER 2025

Mauricio Tano, Ramiro Freile, Rodrigo de Oliveira,
Samuel Walker, Parikshit Bajpai, Olin Calvin, Chaitanya Bhave

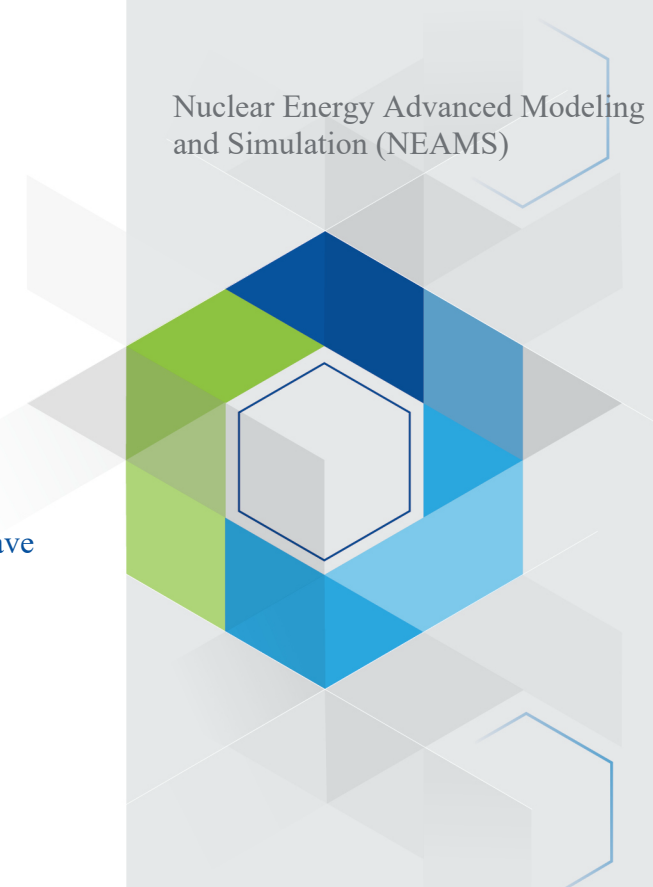
Idaho National Laboratory

Tingzhou Fei, Jun Fang, Andres Fierro, Trinaty Unruh,
Travis Mui, Shayan Shahbazi

Argonne National Laboratory

Donny Hartanto, Eva Davidson

Oak Ridge National Laboratory



DISCLAIMER

This information was prepared as an account of work sponsored by an agency of the U.S. Government. Neither the U.S. Government nor any agency thereof, nor any of their employees, makes any warranty, expressed or implied, or assumes any legal liability or responsibility for the accuracy, completeness, or usefulness, of any information, apparatus, product, or process disclosed, or represents that its use would not infringe privately owned rights. References herein to any specific commercial product, process, or service by trade name, trade mark, manufacturer, or otherwise, does not necessarily constitute or imply its endorsement, recommendation, or favoring by the U.S. Government or any agency thereof. The views and opinions of authors expressed herein do not necessarily state or reflect those of the U.S. Government or any agency thereof.

**Initial steady-state core simulation capability for thermal
and pool-type molten salt reactors, coupling reactor physics,
thermal-hydraulics, and evolving chemistry**

M2 Report

**Mauricio Tano, Ramiro Freile, Rodrigo de Oliveira,
Samuel Walker, Parikshit Bajpai, Olin Calvin, Chaitanya Bhave**

Idaho National Laboratory

Tingzhou Fei, Jun Fang, Andres Fierro, Trinaty Unruh,

Travis Mui, Shayan Shahbazi

Argonne National Laboratory

Donny Hartanto, Eva Davidson

Oak Ridge National Laboratory

SEPTEMBER 2025

**Idaho National Laboratory
Originating Organization
Idaho Falls, Idaho 83415**

<http://www.inl.gov>

Prepared for the
U.S. Department of Energy
Office of Nuclear Energy
Under DOE Idaho Operations Office
Contract DE-AC07-05ID14517

Page intentionally left blank

ABSTRACT

This report presents the development and validation of an initial steady-state multiphysics capability for molten salt reactors (MSRs) under the Nuclear Energy Advanced Modeling and Simulation (NEAMS) program in Fiscal Year 2025. This framework integrates neutronics, thermal-hydraulics, species transport, and thermochemistry to capture the coupled dynamics of liquid-fueled systems. Implementation and testing were performed on two representative designs: the Molten Salt Reactor Experiment (MSRE), a thermal-spectrum, channeled-flow reactor, and the Lotus Molten Salt Reactor (L-MSR), a fast-spectrum, pool-type reactor. The modeling suite employs Griffin for reactor physics and depletion, Pronghorn and SAM for thermal-hydraulics, Thermochimica for chemistry, and Saline for thermophysical properties, with benchmarking and validation carried out against historical MSRE data, experimental flow-loop measurements, and reference depletion calculations from Monte Carlo codes. The framework demonstrated the ability to reproduce key reactor behaviors including temperature feedback, reactivity losses, delayed neutron precursor transport, xenon poisoning, and redox potential evolution.

The results confirm the feasibility and accuracy of the coupled models in predicting steady-state and selected transient MSR behaviors. The latter results and transient behavior are used in this report as a proxy indicating that the steady-state models from which the transient starts are accurate. For MSRE, validation showed good agreement with pump start-up and natural circulation tests, while for the L-MSR, benchmarking confirmed hydraulic calibration and consistency of neutronics–thermal coupling. The tools also provided new insights into species transport, noble metal deposition, and salt solidification dynamics. On the Xenon transport front, the code is validated against the steady state Xenon poisoning measurement and showed good agreement with the experimental value. Identified areas for future work include advanced void transport modeling, three-dimensional simulations, improved alloy corrosion models, and tighter integration with high-fidelity Monte Carlo codes. These developments provide a foundation for high-fidelity MSR simulations that can support reactor design optimization, safety assessments, and long-term operational strategies.

ACKNOWLEDGMENTS

This report was authored by a contractor of the U.S. Government under Contract DE-AC07-05ID14517. Accordingly, the U.S. Government retains a non-exclusive, royalty-free license to publish or reproduce the published form of this contribution, or allow others to do so, for U.S. Government purposes.

This research made use of the resources of the High Performance Computing Center at Idaho National Laboratory, which is supported by the Office of Nuclear Energy of the U.S. Department of Energy and the Nuclear Science User Facilities under Contract No. DE-AC07-05ID14517.

Page intentionally left blank

CONTENTS

ABSTRACT	v
ACRONYMS.....	x
1. INTRODUCTION	1
2. Description of the Multiphysics Capability	3
2.1. Short-term Coupling	8
2.2. Long-term Coupling	8
3. Single-Physics Modeling and Preliminary Validation.....	10
3.1. Neutronics Modeling	10
3.1.1. Deterministic Neutronics Modeling	10
3.1.2. Cross Section Generation	10
3.1.3. Depletion Modeling.....	10
3.2. Thermal-Hydraulics Modeling	11
3.2.1. Systems Code Modeling.....	11
3.2.2. Systems-Level Two-phase Validation.....	11
3.2.3. Coarse-Mesh Thermal Hydraulics Modeling	19
3.2.4. Salt Solidification and Melting.....	21
3.3. Species Tracking, Chemistry, and Thermal Properties.....	22
3.3.1. Thermochemistry modeling.....	22
3.3.2. High-Fidelity Modeling of Species Transport.....	22
3.3.3. Phase Diagram Verification.....	23
3.3.4. Saline	24
3.3.5. Chemistry-Informed Neural-Network Predictions of Thermophysical Properties	25
4. Integral Effects Modeling of the Thermal-Spectrum Molten Salt Reactor Experiment.....	34
4.1. Introduction.....	34
4.2. Description of the MSRE Models.....	34
4.2.1. SAM-based MSRE Model.....	36
4.2.2. Pronghorn-based MSRE Model.....	39
4.3. Preliminary Verification and Validation.....	40
4.3.1. Depletion Modeling and Validation	40
4.3.2. Radiochemical Transport Analysis Using Multi-Region Depletion.....	45
4.3.3. Analysis of Steady-State Pronghorn-Griffin Multiphysics Results.....	46
4.3.4. Pump Start-Up and Coast-Down	49
4.3.5. Pump Start-Up with Added Void Transport.....	51
4.3.6. Natural Circulation Test	52
4.3.7. Testing Coupled Thermal-Hydraulics and Chemistry	53

4.3.8.	Evolution of the Redox Potential.....	54
4.3.9.	Xe Transport	55
4.3.10.	Noble Metal Transport.....	62
5.	Integral Effects Modeling of the Fast-Spectrum Lotus Molten Salt Reactor	67
5.1.	Introduction.....	67
5.2.	Description of the L-MSR Model.....	67
5.3.	Multiphysics Demonstrations and Benchmarking.....	69
5.3.1.	Benchmarking of the Hydraulics Flow Modeling for L-MSR	69
5.3.2.	Improvements in Microscopic Depletion in Griffin for L-MSR	72
5.3.3.	Steady-State Results Analyses.....	77
5.3.4.	Unprotected Pump-Driven Transients	89
5.3.5.	Natural Circulation Operation	93
5.3.6.	Flow Stop with Long-Term Salt Solidification and Re-Melting	96
6.	Conclusions and Future Work	105
6.1.	Conclusions and Future Work for MSRE Integral Modeling.....	105
6.1.1.	Summary and Future Work for Xenon Transport.....	106
6.2.	Future Work for L-MSR Integral Modeling	107
6.3.	Conclusions and Future Work for Depletion Modeling	107
7.	REFERENCES	108

Page intentionally left blank

ACRONYMS

DNP	Delayed Neutron Precursors
DOE	U.S. Department of Energy
DOE-ID	U.S. Department of Energy-Idaho Operations Office
INL	Idaho National Laboratory
L-MSR	Lotus Molten Salt Reactor
MCRE	Molten Chloride Reactor Experiment
MSR	Molten Salt Reactor
MSRE	Molten Salt Reactor Experiment
NEAMS	Nuclear Energy Advanced Modeling and Simulation
PI	Proportional-Integral controller

Page intentionally left blank

Initial steady-state core simulation capability for thermal and pool-type molten salt reactors, coupling reactor physics, thermal-hydraulics, and evolving chemistry

1. INTRODUCTION

The growing interest in advanced nuclear technologies has driven significant research and development toward the implementation of molten salt reactors (MSRs), which promise enhanced safety, sustainability, and efficiency. This report presents the initial steady-state core simulation capabilities for thermal and pool-type molten salt reactors, emphasizing the integration of reactor physics, thermal-hydraulics, and evolving chemistry. The work conducted under the Nuclear Energy Advanced Modeling and Simulation (NEAMS) program in Fiscal Year 2025 focuses on developing a robust framework for modeling MSRs, particularly the Molten Salt Reactor Experiment (MSRE) and the Lotus Molten Salt Reactor (L-MSR).

The integration of various physical phenomena is required for accurately simulating the behavior of MSRs. This report outlines the coupling of neutronics, thermal-hydraulics, and thermochemistry, providing a comprehensive view of the interactions that govern reactor operation. The methodology includes short-term and long-term coupling approaches that account simultaneously for the coupled neutronics and thermal-hydraulics reactor response with the depletion of fuel salt and changes in thermochemical equilibrium, which are essential for understanding reactor dynamics.

Validation of the modeling framework is a key component of this research. The report details the verification and validation process. Through the use of a representative model for a thermal-spectrum, channeled flow MSR (Molten Salt Reactor Experiment -MSRE-) and a fast-spectrum, pool-type one (Lotus Molten Salt Reactor -L-MSR-), the capabilities of the developed tools are thoroughly assessed against benchmarking and experimental data, confirming their reliability for predicting reactor behavior.

Furthermore, the implications of this work extend beyond mere simulation; it provides a foundation for future research in MSR technology and highlights the potential for optimizing reactor design and operational strategies via multiphysics modeling and simulation. By advancing the understanding of MSR dynamics, this report contributes to the ongoing efforts to harness the benefits of liquid-fueled reactors in meeting energy demands sustainably and safely.

In conclusion, this report serves as a comprehensive overview of the initial steady-state core simulation capabilities for thermal and pool-type molten salt reactors, detailing the integration of various physical models and the validation of these tools against experimental data. The findings underscore the importance of continued development and refinement of MSR modeling techniques as we move toward the next generation of nuclear power technologies.

Under NEAMS Molten Salt Reactor Multiphysics Applications, INL, ANL, and ORNL have collaborated towards developing a reference MSR capability using NEAMS tools for steady-state analyses, which is compiled and documented in this report. The two main tasks completed by each laboratory are summarized below.

ORNL completed two specific tasks aimed at establishing initial steady-state core modeling capabilities for a thermal, pool-type molten salt reactor (MSR).

- *Task 1:* Set up a depletion model in Griffin and generating suitable multi-group cross sections using computational tools such as Shift, Serpent, or OpenMC under steady-state reactor conditions.
- *Task 2:* Test SAM/MSTDB-TP coupling for the reference MSR model to ensure the correct parameters and coefficients of interest are being used in the coupled steady state simulations.

The main ANL tasks focused on demonstrating steady state MSR simulation. Specifically, ANL prioritized validating and demonstrating the species transport capability at the steady state that couples neutronics, thermal hydraulics, and species transport. These tasks are listed below:

- *Task 1*: Demonstrate the capability of the NEAMS tool for simulating species transport of important fission products.
- *Task 2*: Validate the model against experimental measurements.

The INL tasks focused on the development, demonstration, and validation of the general multiphysics capability for thermal- and fast-spectrum MSR modeling that is presented in this work. In particular, the two main completed task were:

- *Task 1*: Develop the models and validate the multiphysics capability for the homogeneous core MSRE.
- *Task 2*: Develop, demonstrate, and, whenever possible, benchmark the models for the L-MSR.

The rest of this report is organized as follows. In Section 2, a description of the developed multiphysics capability using NEAMS tools is provided. This section provides details about the transferred fields for steady-state MSR modeling. In Section 3, the modeling of each of the single physics in this multiphysics capability is provided along with independent verification exercises for each of these physics. In Section 4, the integral modeling of the MSRE is developed. This section benchmarks depletion modeling, validate transients as a proxy demonstrating the performance of the steady-state model, and presents several transient applications including computations on the evolution of the redox potential and xenon and noble metal transport. Then, Section 5 presents the integral model for the pool-type L-MSR. This section benchmark depletion and the hydraulics modeling in this reactor, analyze in detail the steady-state fields obtained, and demonstrate pump-driven transients, natural circulation operation, and long-term shutdown conditions with solidification. Each of the individual studies performed presents conclusions on those studies; however, Section 6 finally presents the general conclusions and future work proposed.

2. Description of the Multiphysics Capability

The work conducted in Fiscal Year 2025 under the NEAMS Multiphysics Applications Molten Salt Reactor (MSR) work-package focuses on developing an initial capability for steady-state multiphysics modeling of MSRs. This capability integrates neutronics, thermal-hydraulics, solid mechanics, and thermochemistry as schematically depicted in Figure 2-1. The following paragraphs describe this capability in further detail.

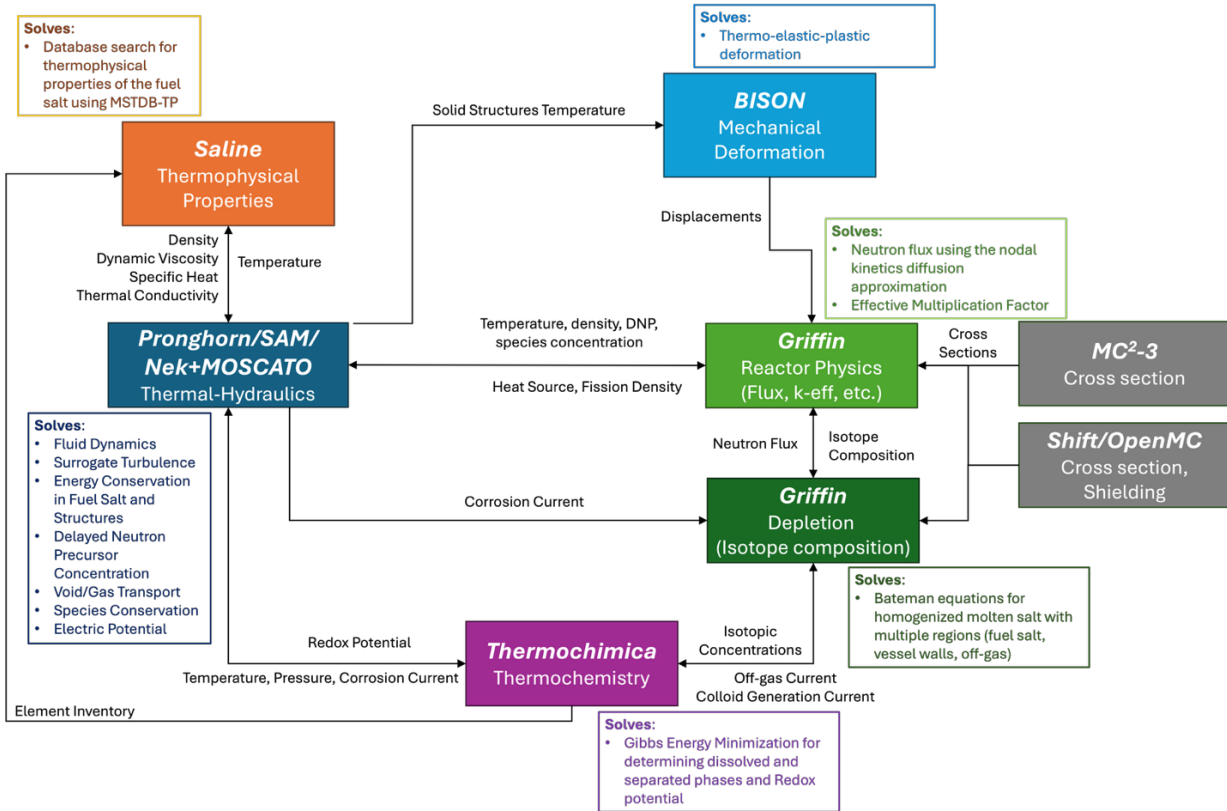


Figure 2-1. Schematic representation of the initial steady-state capability being developed during Fiscal Year 2025.

The following applications have been leveraged in the multiphysics framework developed:

- **Saline (Thermophysical Properties)**. No PDEs are solved; Saline evaluates temperature-/composition-dependent correlations from MSTDB-TP to return liquid-salt density, viscosity, thermal conductivity, heat capacity, and enthalpy (plus derivatives) for use by the other solvers, namely Pronghorn and SAM.
- **Pronghorn/SAM/Nek+MOSCATO (Thermal-Hydraulics)**. Pronghorn solves volume-averaged two-phase mixture equations: continuity for dispersed and mixture phases, a momentum equation with viscous + turbulent stresses and porous (Darcy–Forchheimer) resistance, and energy equations for fluid and solid; it also advances transport equations for delayed-neutron precursors, chemical species, interfacial area concentration, and (when enabled) the Poisson–Nernst–Planck system for ionic species and electric potential with mixed-control (Butler–Volmer + mass-transfer) boundary kinetics. SAM solves an equivalent formulation for 1D system components. Nek5000/NekRS solve the Navier Stokes with high fidelity and MOSCATO implements an equivalent Poisson–Nernst–Planck model than the Pronghorn one.

- **BISON (Solid Mechanics).** Solves quasi-static mechanical equilibrium with small (or finite) strain thermo-elastic–plastic constitutive laws (J2 yield, associative flow, isotropic hardening), where thermal strain is driven by the solid-temperature field from TH.
- **Griffin (Reactor Physics).** Solves the multigroup neutron diffusion eigenvalue/transient equations with scattering, absorption, and fission sources, including a delayed-neutron source term built from circulating precursor concentrations and cross sections interpolated from local temperature/density.
- **Griffin–Depletion (Depletion).** Solves the Bateman ODE system for nuclide inventories (production, decay, transmutation, removal) using transmutation rates derived from the neutron flux and advanced with a stiff solver (e.g., CRAM), optionally augmented by off-gas/plate-out source terms.
- **MC2-3, Shift, and OpenMC.** Solve the neutron transport problem using the Monte Carlo methods. They also tally the multigroup cross sections to be used in the Griffin reactor physics calculations and can be used for shielding calculations.
- **Thermochimica (Thermochemistry).** Performs constrained Gibbs-energy minimization at given (T, P) and elemental totals to determine equilibrium phase assemblages, species activities, and redox potentials, which then provide thermochemical sources/sinks and electrochemical reference states to the transport and electrochemistry models.

As depicted in Figure 2-1, each of these individual physics are coupled in the multiphysics framework. In the following paragraphs the main online couplings affecting the steady-state operations of MSRs is described in further detail.

Pronghorn/SAM \leftrightarrow Saline (thermal-hydraulics \leftrightarrow thermophysical properties)

Pronghorn/SAM \rightarrow Saline Transfers: The fuel-salt temperature at the nodes (T) and, when composition evolves, the current elements mole fractions used as Saline’s composition vector (\mathbf{x}_c) at every node. This is a read-only query, i.e., TH provides the independent variables at the points where material properties are needed.

Saline \rightarrow Pronghorn/SAM Transfers: Saline returns density $\rho(T, \mathbf{x}_c)$, dynamic viscosity $\mu(T, \mathbf{x}_c)$, thermal conductivity $k(T, \mathbf{x}_c)$, specific heat at constant pressure $c_p(T, \mathbf{x}_c)$, and enthalpy $h(T, \mathbf{x}_c)$. In the mixture momentum equation these determine the inertial and viscous terms (ρ in the transient and convective terms, μ in the viscous stress and porous drag); in the energy equation they set the storage term (ρc_p), heat thermal conductivity (k), and the turbulent heat diffusivity via $\alpha_t = v_t/Pr_t$ with $v_t = \mu_t/\rho$ computed via the turbulence model. Enthalpy is used for variable-set conversions when needed (e.g., $(p, h) \rightarrow (p, T)$ in MOOSE materials).

Saline is queried at TH quadrature points (point sampling/interpolation). Units are SI; no rescaling is needed. When composition changes because of chemistry or depletion, the same composition vector used in the transport model is passed to Saline to keep properties consistent with species transport. The coupling iterations are performed every TH nonlinear iteration in every time step; properties are considered “frozen” only within a residual evaluation. No direct exchanges exist between Saline and BISON/Griffin/Depletion/Thermochimica; those physics see Saline’s influence only indirectly via TH’s fields.

Pronghorn/SAM → BISON (thermal-hydraulics drives solid mechanics)

Pronghorn/SAM → BISON Transfer: The solid temperature field $T_s(x)$ of the reflector and any other structural regions. Optionally, pressure can be passed if a pressure-dependent constitutive model were enabled (not used here). In BISON the thermal strain $\boldsymbol{\epsilon}^{\text{th}} = \alpha (T_s - T_{ref}) \mathbf{I}$ is added to the elastic-plastic strain split. Through this, T_s modifies the stress solution by “imposing” free expansion/contraction; temperature-dependent elastic moduli or yield data can be enabled but are kept constant in this study.

In the transfers, the temperature is projected from the TH mesh to the mechanics mesh with an L^2 -conservative volume map for cell-centered materials, or nodal interpolation when the constitutive object consumes nodal values. Units are unchanged. If multiple solid subdomains exist, each receives its own T_s field. Transfer are performed every outer coupling iteration and every time step. BISON does not send anything back directly to TH in this configuration (no contact heat resistance or stress-dependent conductivity is modeled).

BISON → Griffin (solid mechanics deforms neutronics geometry)

BISON → Griffin Transfer: the displacements computed in BISON ($\mathbf{u}(x)$) are sent to Griffin, where they are used to deform the mesh of the solid structures, thus updating the nodes in the neutronics calculations. Griffin rebuilds the diffusion operator and boundary locations on the deformed mesh. Changes in reflector-to-fuel geometry modify leakage (strong effect for small cores) and move vacuum/reflector interfaces, which changes boundary currents and therefore k_{eff} and the power distribution.

In the transfer, mesh nodal coordinates are mapped one-to-one with no unit conversion. Mesh quality is checked (positive Jacobians, limited skewness) before Griffin proceeds. Transfers are performed each outer iteration; if the thermal field changes little, the displacement field also changes little and Griffin sees tiny geometric updates.

No direct feedback from Griffin to BISON is modeled (e.g., no radiation swelling or neutron-damage-driven strains).

Pronghorn/SAM ↔ Griffin (thermal-hydraulics and reactor physics)

TH → Griffin Reactor State Transfers:

1. *Thermal state for cross sections:* the fluid temperature/density (T, ρ_m) and the solid temperature/density (T_s, ρ_s) are passed on Griffin’s material map. Griffin uses these to interpolate the multigroup cross sections and diffusion coefficients ($D_g, \Sigma_{a,g}, \Sigma_{s,g' \rightarrow g}, \nu \Sigma_{f,g}, \chi_{p,g}, \chi_{d,g}$).
2. *Delayed precursor fields:* the advected/diffused precursor concentrations $c_i(x)$ computed in TH enter the delayed neutron source term as $\chi_{d,g} \sum_i \lambda_i c_i$.
3. *Void fraction:* the local void (α_d) is supplied to Griffin where a homogenized salt/void treatment is used or where removing salt from a cell affects moderation/leakage.
4. *Species concentration:* the species concentration evaluated in the TH code is transferred to Griffin as the isotopic composition.

Griffin → TH Power Coupling Transfers:

1. *Volumetric fission heat source $q_f''(x)$:* injected into the fluid energy equation as a volumetric heat source.

2. *Fission density* $R_f(\mathbf{x})$: used for diagnostics or heat partitioning if gamma deposition in structures is modeled.

All of these are volumetric fields. We use conservative cell-to-cell projections (L^2) so that the integral of q_f''' matches the target reactor power. Griffin normalizes the neutron flux to the requested power each outer iteration, while TH checks the energy balance by integrating q_f''' over the domain. Temperatures and densities passed to Griffin are clamped to the valid ranges of the XS libraries. Precursor fields and void fractions are transferred as cell averages (no rescaling needed). Transfers are bidirectionally every outer iteration and time step. This is the main feedback loop (power → temperature/density → cross sections → power). We apply Aitken relaxation to q_f''' and to the delayed-source fields when transients are stiff.

Griffin → Griffin-Depletion (neutronics drives depletion)

Griffin → Griffin-Depletion Transfer: The multigroup flux $\phi_g(\mathbf{x})$ is transferred to the depletion mesh. Reaction rates are computed by taking into account the spatial shape of the neutron flux. The neutron flux acts in the Bateman ODE system for nuclide inventories, via the transmutation/production operator $M(\phi)$. Stiff advancement is performed (CRAM) over depletion substeps.

Transfers are performed via conservative volume projection. The flux is already power-normalized by Griffin, so depletion sees a physically consistent reaction rate field. If depletion is subcycled, i.e., using larger timesteps than TH, the same mapped rates are used across those substeps. Transfers are performed every m TH steps, which is configurable via the *MultiApp* system in MOOSE; during the $m - 1$ intermediate TH steps, the nuclide vector is treated as frozen.

Griffin-Depletion does not send XS feedback directly to Griffin in this study (low power/short exposure), but the pathway exists to update cross sections from changing composition if needed.

Griffin-Depletion ↔ Thermochimica (inventories ↔ equilibrium chemistry)

Depletion → Thermochimica Transfer: The vector of nuclide number densities N_k is converted to element totals b_j through the nuclide stoichiometry and Avogadro's number. Those totals, together with local T and p , define the elemental constraints for a Gibbs-energy minimization.

Thermochimica → Depletion Transfer: Chemistry returns removal/addition terms that alter the Bateman equations: off-gas (volatile) removal, plate-out/colloid deposition on walls, and any re-entrainment sources for colloids. These can be provided as (i) volumetric rates (s^{-1}) directly applied to N_k or (ii) interfacial currents converted to molar flux by Faraday's law and then to a volumetric sink using the local surface-to-volume ratio.

The transfers are scaled from atoms in depletion to moles in thermochemistry using Avogadro's number. In this way interfacial currents in $A \text{ m}^{-2}$ become mol $\text{m}^{-2} \text{ s}^{-1}$ by $j/(nF)$, then mol $\text{m}^{-3} \text{ s}^{-1}$ by multiplying with area over volume ratio for the target cell. To avoid issues with signs, we follow outward normal convention, i.e., loss from the fluid is a sink. Transfers occur at each depletion block, or each TH step if chemistry is active and fast (e.g., strong interfacial currents). Between calls, the removal rates are held constant.

Pronghorn/SAM ↔ Thermochimica (transport ↔ equilibrium/redox)

TH → Thermochimica Transfers:

1. *Thermodynamic state*: local temperature and pressure at each cell as computed from the TH solve.

2. *Element inventories*: the element totals carried by the transport model, augmented by Depletion outputs, define the composition constraint used by the equilibrium solve.
3. *Interfacial corrosion currents*: the mixed-control PNP boundary condition gives a current density j at reactive surfaces. Using Faraday's law and the stoichiometry of the dissolving metal, these currents are converted into elemental removal rates and included in the element balance before the TC call; this ensures that electrochemical mass transfer alters the equilibrium problem consistently.

Thermochimica → TH Transfers:

1. *Redox potential E_{eq}* : used as the reference potential in the overpotential definition for the Butler–Volmer kinetics; this closes the electrochemical boundary condition consistently with the current chemistry state.
2. *Activities and thermodynamic factors*: activity coefficients and thermodynamic factors update the Nernst–Planck transport coefficients in the electrolyte transport equations, so that diffusion and migration respond to non-ideality.
3. *Phase appearance*: when equilibrium predicts a gas phase or solid precipitate, TH's void fraction and, when enabled, interfacial area equations receive corresponding source terms.

In the transfers temperatures and pressures are passed cellwise; E_{eq} is returned in volts for every cell; activities are dimensionless; currents in $A\ m^{-2}$ are mapped from faces to volumes as molar sinks using surface-to-volume ratios. Care is taken to use the same standard states in both TC and PNP; otherwise E_{eq} would be inconsistent with the activity convention used in transport. In transients with active electrochemistry, transfers are performed every TH iteration; otherwise at a slower chemistry time scale (e.g., every m steps) with the returned rates and potentials frozen in between.

It is worth noticing that are pair of physics that are not coupled directly. These are briefly addressed below:

- **Saline ↔ BISON / Griffin / Depletion / Thermochimica.** Saline provides liquid properties only; solids and neutronics do not query Saline directly, and chemistry uses its own activity models. All property influences reach those physics via TH.
- **BISON ↔ Depletion / Thermochimica.** We do not model chemomechanical swelling or deposition-induced layer growth in the reflector; therefore, mechanics does not exchange fields with depletion or chemistry.
- **Griffin ↔ Thermochimica.** Neutronics does not consume chemistry outputs directly; the link is through Depletion (inventories) and TH/PNP (redox setting interfacial kinetics).

All volumetric fields ($q''_f, R_f, c_i, \alpha_d, T, \rho$) are exchanged with conservative cell-to-cell projections so that integrals (e.g., total power, total nuclide amount) are preserved to machine precision across meshes. Pointwise quantities (Saline properties, displacements) are evaluated/interpolated at the receiving quadrature points or nodes. Surface currents are turned into volumetric sources by multiplying the face-average by the local surface-to-volume ratio; when those currents represent electrons, Faraday's law converts to molar flux before the surface-to-volume conversion. Cross sections are always interpolated within their tabulated (T, ρ) bounds; values are clamped at the boundaries to avoid extrapolation. Griffin normalizes power at every outer iteration; TH checks the integral of q'' against the target and rejects the iteration if the mismatch exceeds tolerance. Where feedback is strong (power↔temperature, redox↔current), we apply Aitken Δ^2 relaxation to the exchanged fields to ensure monotone convergence of the outer fixed-point loop.

TH, Saline, BISON, and Griffin are called every global time step. Depletion subcycles with a larger step (e.g., every m TH steps) using a stiff matrix exponential (CRAM) with the latest flux; its inventories are held piecewise constant between calls. Thermochimica is called every TH step when interfacial electrochemistry is active; otherwise at a slower chemistry cadence with returned rates and potentials frozen in between. Geometry updates from BISON are propagated to Griffin at every outer iteration, so leakage effects are always in sync with the current temperature field.

Convergence of the outer fixed-point loop is declared only when: (i) the sup-norm change of every exchanged field ($q_f''', \phi_g, c_i, \alpha_d, T, T_s, \rho, u, E_{eq}, N_k, b_j$) drops below a tight relative tolerance; (ii) the integrated power equals the target to within 10^{-8} of relative accuracy; (iii) k_{eff} and flux settle (e.g., for our examples, $|\Delta k_{eff}| < 5 \times 10^{-7}$ and relative flux change $< 10^{-6}$); (iv) the redox potential and interfacial current stabilize; and (v) depletion inventories change less than 10^{-4} in relative L¹ norm over a depletion block. Energy, element, and charge audits close the loop: the integral of q''' equals the thermal removal; the change in elemental totals equals the applied interfacial fluxes plus depletion sources/sinks; and the integral of ionic flux at electrochemical boundaries equals the electronic current by Faraday's law.

Although the coupled framework can be used to model most steady-state and transient conditions, in practice, one may want to avoid constantly paying the computational cost associated to the complete multiphysics framework. Hence, a distinction is developed between the short-term coupling, i.e., phenomena that will affect reactivity or flow driven reactor transients, and long-term coupling, i.e., phenomena that will affect longer term evolution in the MSR performance.

2.1. Short-term Coupling

Pronghorn has been chosen as the engineering thermal-hydraulics solver for MSRs. Pronghorn solves the equations of conservation of mass, linear momentum, and energy in the liquid salt using a weakly compressible formulation. Additionally, Pronghorn integrates models of the solid components of MSRs and allows for either bulk or fluid-to-wall conjugate heat transfer with the liquid salt. It also tracks the concentrations of delayed neutron precursors in the circulating liquid nuclear fuel and the void fraction.

For reactor performance calculations, the temperature and void fraction computed by Pronghorn are read by Griffin, the reactor physics code. In our MSR models, Griffin solves the conservation equations of the neutron flux using nodal diffusion kinetics, coupled with circulating volumetric concentrations of delayed neutron precursors. Griffin develops homogeneous models, where the moderator and fuel salt are homogenized per computational cell. This approach is similar to that used in fast-spectrum MSR modeling. For steady-state models, Griffin solves the k-eigenvalue problem. Transients are solved with the fission source normalized by the eigenvalue obtained in the previous steady-state problem. Griffin computes the power density and the fission rate density, which are then passed to Pronghorn for solving the energy conservation equation and tracking the delayed fission products, respectively. Coupling iterations between Pronghorn and Griffin determine the steady-state operation at various power levels and solve for short-term transients.

2.2. Long-term Coupling

Long-term coupling must account for (i) depletion of the fuel salt, (ii) changes in thermochemical equilibrium, which can lead to phase separation, precipitation, plating, and leaching, among others, and (iii) resulting changes in the thermophysical properties of the fuel salt. These issues are addressed by coupling the Pronghorn-Griffin model with the depletion capabilities in Griffin, Thermochimica, and Saline.

The depletion calculations in Griffin use the flux-averaged results computed with Griffin-neutronics. The power density during operation is directly set in the depletion functionality to accommodate longer-term transients. For species separation modeling in depletion, the Griffin-depletion functionality is coupled with Pronghorn and Thermochimica. Pronghorn uses its Poisson-Nernst-Planck corrosion model to solve for electrochemical corrosion in the molten salt, leading to corrosion currents that determine element exchange between the fuel salt and the solid walls. The element current is converted to isotopic currents based on the average isotopic concentration in the fuel salt or structures from which the elemental corrosion current originates. Additionally, Thermochimica solves the chemical equilibrium in the salt, determining the phases and speciation of elements. From this speciation, some phases separate from the fuel salt as gases (off-gassing) or precipitate as solids via a flocculation process. The volumetric currents of off-gassing and precipitation are computed by Thermochimica and passed to Griffin depletion to correct depletion calculations due to phase separation.

Thermochimica requires the element concentration per computational cell and the temperature and pressure of this cell to solve for phase equilibrium via Gibbs energy minimization. The elemental compositions are computed by transforming Griffin's isotopic inventory into elements and assuming uniform mixing across the fuel salt. The temperature and pressure per computational cell are provided by Pronghorn. Once Thermochimica computes the equilibrium concentrations, the dissolved element compositions in the liquid salt are provided to Saline.

Saline is used to compute the evolution of the thermophysical properties of the fuel salt. In addition to the dissolved element compositions provided by Thermochimica, Saline receives the temperature and pressure per computational cell from the Pronghorn simulation. Saline then computes the density, dynamic viscosity, thermal conductivity, and specific heat of the fuel salt, which are passed to Pronghorn as Eulerian fields for the thermal-hydraulics calculations.

This section has introduced the main physics solved in the reference multiphysics modeling framework developed for MSR steady-state analyses. In the next section, each of the modeled physics is addressed in further detail and, when required, individual verification or validation exercises are provided.

3. Single-Physics Modeling and Preliminary Validation

3.1. Neutronics Modeling

3.1.1. Deterministic Neutronics Modeling

This section details the Griffin-Pronghorn modeling approach applied to the Molten Salt Reactor Experiment (MSRE) and the Lotus Molten Salt Reactor (L-MSR). The approach integrates coupled neutron transport and depletion modeling with thermal hydraulics, including two-phase flow, and species tracking. This approach is the same one than the one implemented in FY24. Hence, the reader is referred to our previous report ([Shahbazi et al., 2024](#)) for details about equations solved and its numerical solution.

3.1.2. Cross Section Generation

Currently, Griffin relies on external codes to provide accurate multigroup neutron cross sections for simulating MSRs. Although Griffin possesses internal capabilities for cross section generation, this functionality is not yet implemented for MSRs. Griffin solves multigroup neutron diffusion equations using either macroscopic or microscopic cross section datasets. Typically, the necessary cross sections include transport or diffusion, absorption, removal, scattering, and fission, among others. These cross sections should account for energy dependence, resonances, temperature effects, and spatial heterogeneities specific to reactor cores.

Depending on the type of calculations, Griffin can use either macroscopic or microscopic cross sections for performing radiation transport calculations. Microscopic cross sections are typically required for depletion simulations, while macroscopic cross sections are sufficient for eigenvalue transport problems. Both types of cross sections can be generated through external lattice physics or Monte Carlo neutron transport codes, such as OpenMC ([Romano et al., 2015](#)) and Shift ([Pandya et al., 2016](#)). Utilizing Monte Carlo methods for cross section generation offers advantages, primarily because they simulate neutron transport at the continuous-energy level, capturing detailed energy-dependent neutron flux distributions. This detailed flux information is important for accurate calculations of resonance self-shielding effects and reaction rates. Then, the multigroup cross sections are typically generated through flux-weighted averaging of reaction cross sections within defined energy groups, as shown in Eq. (2-6). It is important to note, however, that different Monte Carlo codes employ varying approaches to tally and generate the multigroup cross sections ([Boyd et al., 2019; Pandya et al., 2022](#)).

$$\Sigma_{x,k,g} = \frac{\int_r dr \int_{E_g}^{E_{g-1}} \Sigma_x(r, E') \varphi(r, E') dE'}{\int_r dr \int_{E_g}^{E_{g-1}} \varphi(r, E') dE'} \quad 3-6$$

Griffin reads cross section data in ISOXML format. For this purpose, it includes a utility tool that can process OpenMC output files and convert generated multigroup cross sections into the required ISOXML file. For Shift, the code provides its own utility to generate cross section files directly in ISOXML format. These utilities streamline the integration of Monte Carlo cross section data into Griffin's deterministic simulation workflow.

3.1.3. Depletion Modeling

Depletion modeling is inherently more complex in liquid-fueled MSRs compared to solid-fueled reactors. This complexity arises primarily because the isotopic composition of circulating fuel salt evolves continuously due to ongoing nuclear reactions, active removal of specific fission products, and continuous or batch-wise addition of makeup fuel. For instance, gaseous fission products such as Kr and Xe must be promptly removed because Xe-135 has a very high thermal neutron absorption cross-section, which, if accumulated, significantly reduces reactor reactivity. Similarly, noble-metal fission products must also be

periodically extracted, as their deposition onto reactor components can cause localized radiation hotspots, reduce heat exchanger efficiency, and accelerate corrosion. In parallel with fission-product removal, fresh fissile material must be continuously introduced to compensate for fuel consumption and maintain criticality throughout reactor operation. Furthermore, careful redox control through controlled addition of Be or U species is necessary to maintain optimal chemical conditions and minimize structural alloy corrosion.

Unlike solid-fueled reactors, spatially explicit region-wise depletion calculations are unsuitable for MSRs because of continuous circulation and mixing of the fuel salt. Instead, the depletion analysis for MSRs commonly employs a 0-D, point-depletion approach, approximating the fuel as being uniformly mixed. To accurately represent spatial variations of neutron flux due to the fuel salt's residence time in the high-flux core region and low or negligible flux out of core region, a flux-scaling technique is applied, ([Betzler, 2021](#)).

In Griffin, depletion modeling can be conducted using two distinct approaches: macroscopic depletion and microscopic depletion. In macroscopic depletion modeling, macroscopic cross sections must first be prepared and tabulated at a grid of burnup points, alongside other parameter grids such as fuel and coolant temperatures. The macroscopic depletion modeling for MSRs, specifically for the Molten Salt Reactor Experiment (MSRE), has been successfully demonstrated during FY23 ([Hartanto et al., 2023](#)). In this macroscopic approach, Griffin solves the neutron transport equation using the provided multi-group macroscopic cross sections. The resulting neutron flux is collapsed into a one-group flux, and then transferred to [VectorPostProcessors/BatemanVPP] block ([Walker et al., 2022](#)) that is available in Griffin's experimental branch. This block calculates isotopic number densities at each depletion step using the Bateman equation solver and requires user-provided initial fuel salt number densities, a decay and transmutation library, and one-group microscopic reaction cross sections, in addition to the previously prepared macroscopic cross sections. Importantly, this block supports fractional fission-product removals and continuous fuel feed for accurate MSR depletion modeling. Conversely, microscopic depletion modeling directly employs microscopic cross sections tabulated over grids of burnup, temperature, and other parameters. In this approach, Griffin calculates isotopic number densities explicitly using the Bateman solver. These calculated densities directly update macroscopic cross sections at each depletion step. Unlike macroscopic modeling, microscopic depletion requires initial isotope number densities to be explicitly defined within Griffin's input file. Currently, Griffin's microscopic depletion method is limited to solid-fuel reactors because it does not yet incorporate essential MSR-specific features, such as fractional removal of fission products or continuous fuel feed. However, in this study, the microscopic depletion method was evaluated to assess its feasibility and to identify potential limitations of extending Griffin's microscopic depletion approach to future MSR analyses.

3.2. Thermal-Hydraulics Modeling

3.2.1. Systems Code Modeling

The systems-level code modeling relies on the SAM code. Based on the work from the previous year, recent SAM updates have resolved most of the issues identified, including the salt-to-bubble and salt-to-graphite species mass transfer. More details about the physical models implemented in SAM are documented in Mui et al., 2024 and Mui et al., 2025.

3.2.2. Systems-Level Two-phase Validation

To evaluate the fidelity of SAM's thermal-hydraulic modeling capabilities, we performed a detailed validation study using the Texas A&M University (TAMU) Molten Salt Flow Loop (MSFL) as a reference system. This loop serves as an experimental platform for investigating steady-state and transient

behavior in high-Prandtl-number molten salts, and includes instrumentation for measuring pressure, and temperature at multiple locations. Velocity profile and magnitude can be gathered from the transparent test section. Our objective was to assess SAM's readiness for advanced modeling of molten salts by reproducing experimentally observed behavior in both single-phase and two-phase flow regimes.

The natural circulation molten salt flow loop (MSFL) at TAMU, constructed in the Fall of 2022, has unique flow visualization capabilities ([Reis et al., 2014](#)). A heated quartz transparent test section in the left vertical leg allows for Particle Image Velocimetry (PIV) without disruption to the velocity profile nor heat losses.

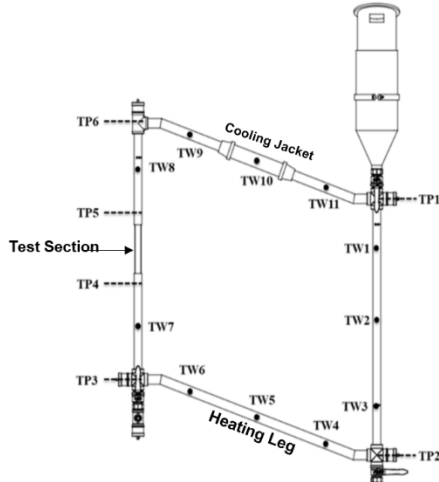


Figure 3-1. TAMU MSFL.

The heated quartz test section is 0.025 meters in diameter and 0.186 meters long, with three layers of fiberglass insulation to mitigate heat losses. As for the rest of the loop, each leg has a length of 0.9144 meters, an outer diameter of 0.0254 meters, and an inner diameter of 0.0221 meters. The upper and lower legs have an inclination of 20° from the horizontal, and the entire loop is insulated. The cooling jacket has a length of 0.305 meters, an outer diameter of 0.0508 meters, and an adjustable air volumetric flow rate of up to 300 liters per minute. These values are summarized by Table 3-1. The bottom leg is heated by high-temperature tape ([Reis et al., 2014](#)). The experimenters allowed the flow to develop for more than 24 hours, after which the system was at steady state.

Table 3-1. TAMU MSFL Geometry.

MSFL Geometry	
Leg Length	0.9144 meters
Outer Diameter	0.0254 meters
Inner Diameter	0.0221 meters
Inclination from Horizontal	20°
Test Section Length	0.186 meters
Cooling Jacket Length	0.305 meters
Cooling Jacket Outer Diameter	0.0508 meters

Five kilograms of HITEC, approximately 7% NaNO₃, 49% NaNO₂, and 44% KNO₃, were prepared for the loop. The correlations for viscosity, μ (N * s / m²), density, ρ (kg / m³), and specific heat, c_p (J / kg - K), in equations 3-1 through 3-3 come from the INL thermophysical properties database of molten salts (Sohal et al., 2010), and the equation for the heat conduction coefficient, k (W / m - K), comes from Santini et al. (Santini et al., 2014).

$$\mu = 0.4737 - 2.297 \times 10^{-3} T + 3.731 \times 10^{-6} T^2 - 2.019 \times 10^{-9} T^3 \quad 3-1$$

$$\rho = 2293.6 - 0.7497 T \quad 3-2$$

$$c_p = 5806 - 10.833 T + 7.2413 \times 10^{-3} T^2 \quad 3-3$$

$$k = 0.78 - 1.25 \times 10^{-3} T + 1.6 \times 10^{-6} T^2 \quad 3-4$$

$$\sigma = 0.14928 - 55.6 \times 10^{-6} T \quad 3-5$$

Figure 3-2 and Figure 3-3 show bubbly flow in water and salt, respectively. The first photo in the series (i.e., black and white), corresponds to a photo with no processing, with the tube diameter for reference. The next two photos in the series use the PIV data to track corresponding velocity in the x-direction and y-direction, respectively. Finally, this data is used to calculate the vorticity, depicted in the final picture in each four-picture series with the arrows indicating direction and wake of the bubble.

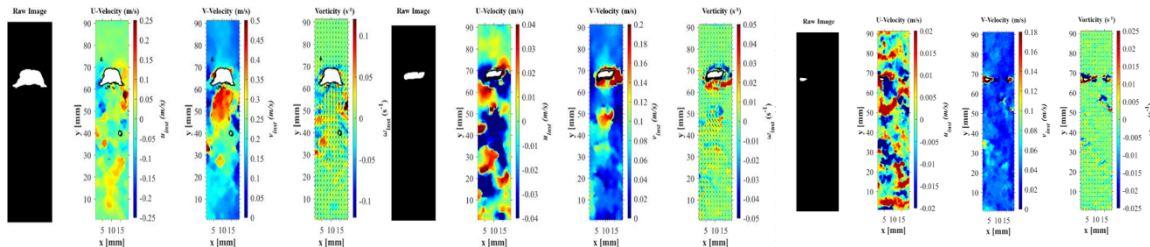


Figure 3-2. Water tests 1 through 3.

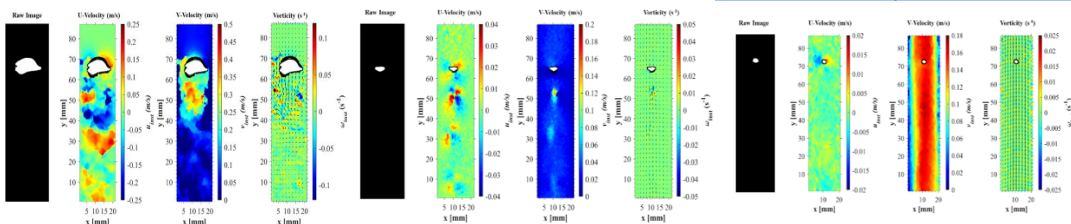


Figure 3-3. Salt tests 1 through 3.

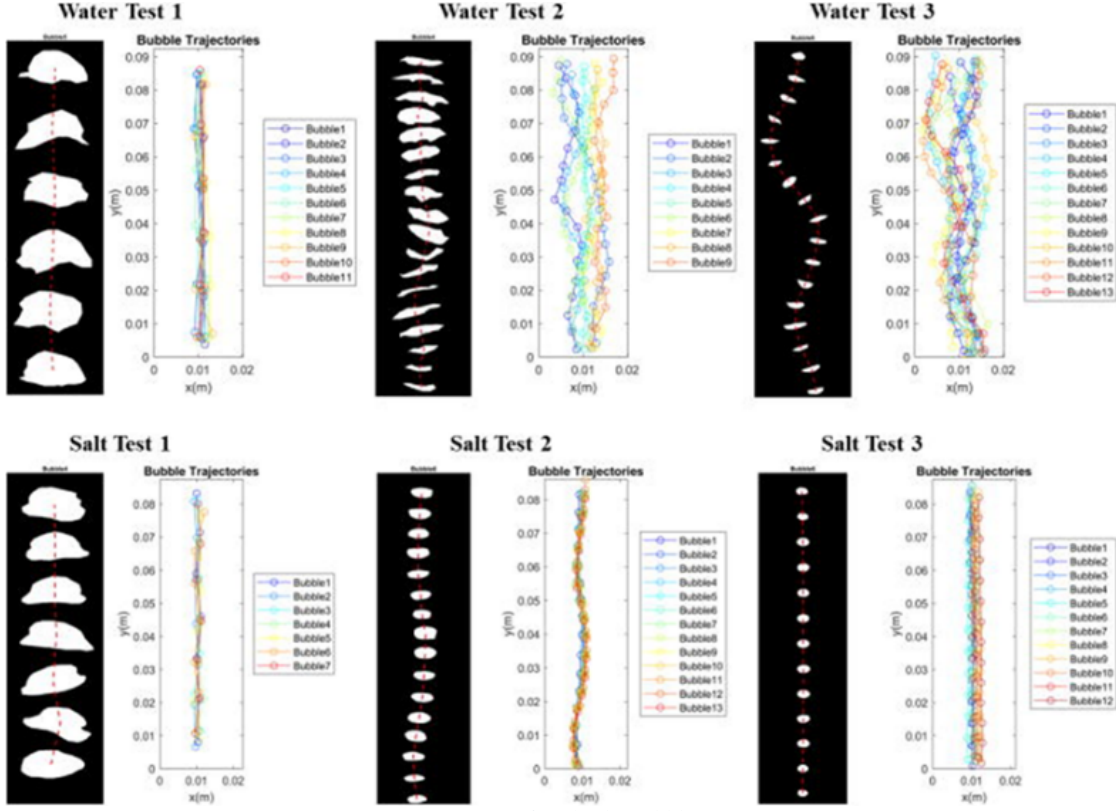


Figure 3-4. Summary of Multiple Bubble Experiments.

The SAM model was built to approximate the geometry and operating conditions of the TAMU loop using a 1D approximation. Boundary conditions included a fixed heat input on the hot leg, convective cooling on the cold leg, and appropriate mass flow rate or pressure pinning to stabilize the flow. To correctly capture heat removal in developing one dimensional flow, the convective cooling boundary employed an approach based on Zou et al. In this approach, an arbitrarily large convective heat transfer coefficient pins the requisite outlet temperature to the ambient temperature. Wall friction factors were defined as a global parameter based on experimental findings (Reis et al., 2014).

PTFluidPropertiesEOS were used for the argon gas phase, with a constant viscosity and coefficient of thermal conductivity defined at a representative temperature for the loop. To ease future modeling of HITEC salts, a HITEC option was added to the SaltEquationOfState to the SAM framework for the temperature range of 373 K to 773 K. A linearization of C_p was used around the temperature of 460 K for speed of simulation, specifically when calculating enthalpy. The rest followed the correlations in equations one through five.

The finite-element approach leveraged a first-order trapezoidal quadrature solved with an implicit-Euler numerical scheme.

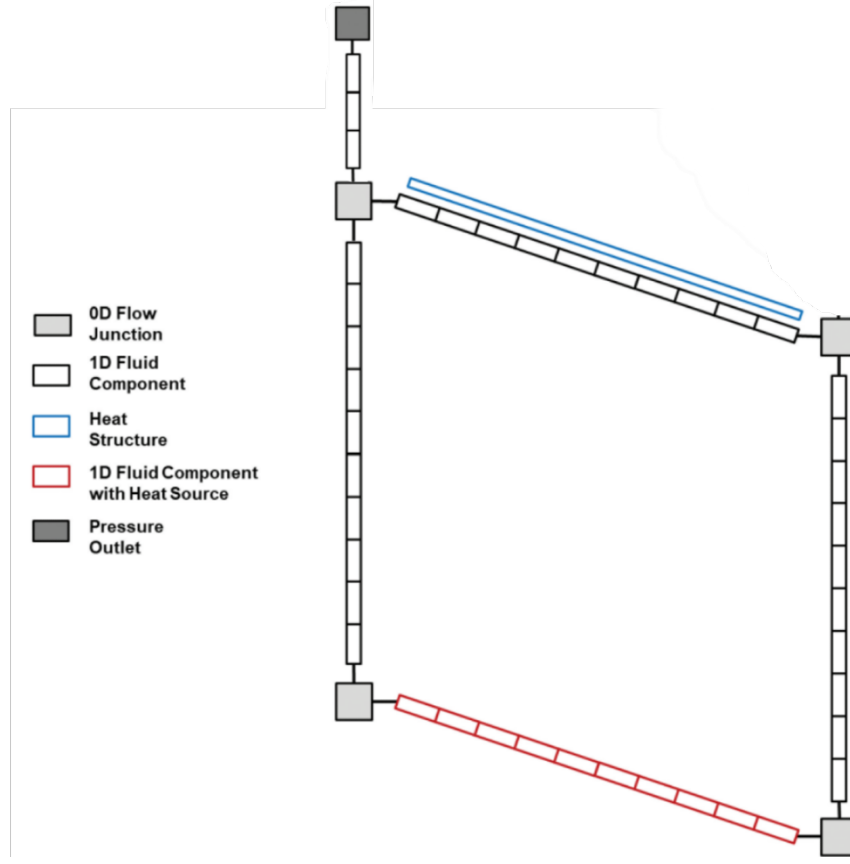


Figure 3-5. SAM Model of the TAMU MSFL.

Achieving close agreement between simulation and experiment required an iterative hand-tuning approach. The process began by adjusting the imposed heat input to match the observed temperature rise (ΔT) across the loop. Next, the cold leg temperature (T_c) was adjusted to achieve a Prandtl number at the test section consistent with the experimental target. Finally, the friction factor was adjusted to yield a velocity profile within experimental uncertainty.

This tuning cycle was repeated until key thermal-hydraulic metrics—temperature, velocity, ΔT , and Prandtl number—were matched within acceptable error margins. A summary of the tuned values and corresponding experimental measurements are shown in Table 3-2 and Table 3-3.

Table 3-2. Salt Single-Phase Results.

	TP1	TP2	TP3	TP6	Velocity
Salt Test 3					
Exp	449.37	443.27	441.37	452.53	0.0185
SAM	442.15	442.15	447.58	447.58	0.0192
Salt Test 2					
Exp	453.26	446.63	446.67	456.72	0.0196
SAM	446.63	446.63	452.64	452.64	0.0191
Salt Test 3					
Exp	465.81	458.52	459.32	466.47	0.0205
SAM	459.00	459.00	464.93	464.93	0.0222
Salt Test 4					
Exp	481.34	475.74	475.95	481.36	0.0237
SAM	475.75	475.75	481.40	481.40	0.0265

Table 3-3. Water Single-Phase Results.

	TP1	TP2	TP3	TP6	Velocity
Water Test 1					
Exp	314.03	313.48	314.48	314.77	0.019
SAM	313.48	313.4	314.69	314.69	0.0232
Water Test 2					
Exp	320.02	319.04	320.06	320.47	0.023
SAM	319.04	319.04	320.41	320.41	0.0275
Water Test 3					
Exp	323.8	323.14	324.02	324.68	0.0277
SAM	323.14	323.14	324.72	324.72	0.0310
Water Test 4					
Exp	333.45	332.71	333.61	334.38	0.035
SAM	332.72	332.72	334.53	334.53	0.0370

Following single-phase validation, we extended the model to include two-phase flow using SAM's drift flux capability. Gas injection was implemented as a point source using a modified version of the `gas_point_source_drift.i` input structure. Argon was used as the injected gas, with an approximated experimental Weber number, the equivalent diameter calculated based on interfacial tension, viscosity, and injection conditions.

The injection profile was defined as a piecewise constant rate, where the first 5000 seconds allow the simulation to reach steady-state single phase before injecting a volumetric flow rate corresponding to the physical tests.

Drift flux terms were activated in SAM using default models unless otherwise specified. We employed the four-equation drift flux model implemented by [Salko et al., 2024](#) to compute drift velocity and void fraction.

Validation was conducted for three experimental configurations corresponding to distinct Prandtl numbers: approximately 15.6, 36.5, and 47.5 for the salt cases and 77.6 for the water cases. The water cases had identical starting thermal hydraulic conditions. For each case, the SAM model was tuned as described above and ran until a quasi-steady state was reached. Then, bubbles were injected at the specified volumetric injection rate for the second and third salt and water cases. It is possible that the first experimental case for both fluids likely overreports their injection rate by an order of magnitude based on the findings of the presently reported validation exercise. The conditions are summarized in Table 3-4. The two main inputs into the two-phase model are the argon injection and the Weber number. The equivalent diameter is calculated by rearranging the input Weber number and multiplying by the various properties evaluated at the test-section temperature.

Table 3-4. Initial Experimental Conditions.

	Salt Test 1	Salt Test 2	Salt Test 3	Water Test 1	Water Test 2	Water Test 3
Argon Injection (m³/s)	1.50E-05	3.50E-07	1.50E-07	3.20E-05	4.90E-07	4.80E-07
Weber Number	8.19	3.86	3.96	13.8	3.58	2.73
<u>Initial Condition before Ar injection</u>						
Heater Power (W)	550	551	555	77.6	77.6	77.6
Air flow (L/min)	0	182	300	188	188	188
Prandtl Number	15.6	36.5	47.5	3.78	3.78	3.78
Velocity (m/s)	0.032	0.030	0.028	0.026	0.026	0.026
ΔT (°C)	11.02	10.27	11.94	1.43	1.43	1.43

To quantify validation accuracy, we added custom postprocessors to track the evolution of key variables throughout the loop, with emphasis on the test section and loop corners. The primary quantities of interest included:

- Gas void fraction
- Gas terminal velocity
- Bubble diameter (D_{eq})

Values were extracted using SAM's integrated postprocessing system and visualized in Paraview for diagnostic purposes.

The results for water and salt cases are shown in Table 3-5 and Table 3-6, respectively. The bottom three rows are the initial thermal hydraulic conditions carefully tuned to minimize error. The focus of the results are the parameters calculated by SAM on the two-phase flow, shown in the first three rows.

The value reported for the experiment column corresponds to the mean result, followed by the range where applicable. The black text underneath each case title specifies the void injected in each case. Again, it seems that the experiment's report may have overestimated the void injected into each fluid's case 1 by an order of magnitude.

For water, we notice that the terminal velocity is overpredicted in all three cases. This has as direct consequence the underprediction of void fraction and equivalent diameter for water cases 1 and 2. The equivalent diameter is within the experimental range for all three water cases. The current drift flux

implementation is meant for smaller, spherical bubbles. Salt case 3 is the more resemblant of those conditions and consequently has a much lower error. It should be noted that the void injected to water cases 2 and 3 is almost identical. The principal difference is the Weber number.

Table 3-5. Water results.

	Water test 1			Water test 2			Water test 3		
	Void Injected: SAM	3.20E-06 Not E-05 Experiment	% Difference	Void Injected: SAM	4.90E-07 Experiment	% Difference	Void Injected: SAM	4.80E-07 Experiment	% Difference
D _{eq} (mm)	10	10.5 10.0–11.3	-4.76%	3.6	4 3.4–4.4	-8.85%	2.8	2.6 2.2–2.9	6.99%
Terminal Velocity (mm/s)	422.58	301.4 281.0–327.1	40.21%	307.7	248.3 228.1–267.2	23.91%	307.3	267.9 233.7–281.6	14.70%
Void fraction	0.020	0.06 0.0540–0.0690	-67.28%	0.0024	0.009 0.0065–0.0105	-73.45%	0.0025	0.0036 0.0026–0.0044	-29.91%
Pr	3.75	3.78	-0.76%	3.75	3.78	-0.76%	3.75	3.78	-0.76%
Fluid velocity (m/s)	0.026	0.026	0.06%	0.026	0.026	0.06%	0.026	0.026	0.06%
ΔT (K)	1.45	1.43	1.44%	1.45	1.43	1.32%	1.45	1.43	1.32%

The first two salt cases overpredict terminal velocity, and while their void fraction is underpredicted, salt case 3 does not follow this trend. Salt case 3 underpredicts both terminal velocity and void fraction. Salt case 1 was unstable and did not converge for many time steps. Salt cases 2 and 3, on the other hand, were very stable.

Table 3-6. Salt results.

	Salt test 1			Salt test 2			Salt test 3		
	Void Injected: SAM	1.50E-06 Not E-05 Experiment	% Difference	Void Injected: SAM	3.50E-07 Experiment	% Difference	Void Injected: SAM	1.50E-07 Experiment	% Difference
D _{eq} (mm)	10	10.5 10.3–10.7	-4.76%	3.5	3.5 3.4–3.6	-0.58%	2.3	2.3 1.9–2.7	0.16%
Terminal Velocity (mm/s)	422.6	221.4 186.8–240.2	90.87%	287.7	264.4 252.9–280.6	8.82%	283.7	326.7 298.5–346.9	-13.17%
Void fraction	0.0196	0.0504 0.0478–0.0529	-61.05%	0.0020	0.0060 0.0057–0.0063	-67.47%	0.0019	0.0027 0.0017–0.0035	-30.95%
Pr	15.7	15.6	0.81%	35.8	36.5	-1.97%	47.6	47.5	0.27%
Fluid velocity (m/s)	0.030	0.032	-6.64%	0.03	0.03	-0.05%	0.028	0.028	0.01%
ΔT (K)	11.09	11.02	0.64%	10.43	10.27	1.58%	10.81	11.94	-9.46%

Error trends were typically under 2% for thermodynamic variables, with larger variability in gas dynamics due to measurement uncertainty and the transient nature of bubble injection.

A series of numerical experiments were conducted to explore the sensitivity of the solution to mesh resolution, FEM order, and timestep size. While second-order FEM produced more accurate results theoretically, first-order FEM offered better convergence behavior in many cases, particularly for two-phase simulations. Dynamic timestep control frequently led to instability due to abrupt void fraction changes; thus, a fixed timestep upper limit was used for most runs.

Convergence was notably improved by:

- Using first-order FEM formulation
- Reducing timestep size
- Adjusting the Courant number limit
- Tuning boundary conditions

In conclusion, SAM was successfully validated against experimental data from the TAMU salt loop across three thermal-hydraulic conditions. By tuning power, friction factor, and cold leg ambient temperature, and by carefully managing numerical stability, the model achieved excellent agreement with key metrics such as ΔT , velocity, and Prandtl number. Extension to two-phase flow with gas injection produced results that captured void fraction and gas velocity trends in line with expectations. Additionally, SAM's post-processing framework was demonstrated to be useful for real-time tuning and diagnosing convergence behavior.

This validation campaign yielded several important insights. First, two-phase simulations in SAM are feasible but require careful initialization and tuning. Second, void fraction underprediction led to overprediction of gas velocity. Third, there is currently no way to capture two-phase flow vorticity or radial oscillations.

Future work could incorporate sensitivity coefficients into drift velocity model to verify if tuning improves overall predictions. Additionally, correlations over a greater domain of bubble sizes and conditions, such as machine-learning drift velocity models, could make predictions more accurate.

3.2.3. Coarse-Mesh Thermal Hydraulics Modeling

The thermal hydraulics model in MSRs solves for the conservation of mass, momentum, and energy within the fuel salt. Several specific modifications have been implemented to accurately track species in MSRs:

- Improvements of the porous media formulation, which is used to model to core internal structures.
- A two-phase flow mixture model, which is used to track void fraction in the reactor core.

The baseline of the thermal-hydraulics model has already been explained in our FY24 report ([Shahbazi et al., 2024](#)).

The two-phase flow balance equations for fluid mass, momentum, energy, and solid energy are coupled through momentum and energy exchanges described by correlations. A key advantage of this approach is the ability to seamlessly integrate porous flow regions with free-flow regions outside the core without altering the overall modeling framework. The porous flow equations for weakly compressible flow read as follows explains the modifications implemented in the weakly-compressible, porous media model for dealing with two-phase flows:

$$\begin{aligned} \frac{\partial \gamma \rho_m}{\partial t} + \nabla \cdot (\rho_m \mathbf{u}_m) &= 0, \quad \frac{\partial \gamma \rho_d}{\partial t} + \nabla \cdot (\rho_d \mathbf{u}_d) = \Gamma_d \\ \frac{\partial \gamma \rho_m}{\partial t} + \nabla \cdot (\gamma^{-1} \rho_m \mathbf{u}_m \mathbf{u}_m) + \nabla \cdot (\gamma^{-1} \alpha \rho_d \mathbf{u}_d \mathbf{u}_d) - \nabla \cdot [(\mu_m + \rho_m v_t) (\nabla u_m + \nabla u_m^T)] \\ &= -\gamma \nabla p_m + \gamma \rho_m \mathbf{g} + \mathbf{f} \\ \frac{\partial \gamma e_m}{\partial t} + \nabla \cdot (\gamma^{-1} \mathbf{u}_m H_m) - \nabla \cdot (\kappa \nabla T) - \nabla \cdot \left(\frac{v_t}{Pr_t} \nabla e_m \right) &= \dot{q}_i''' \end{aligned} \quad 3-6$$

where the following principles have been introduced:

- α : is the void fraction,
- ρ_m : is the mixture density,
- \mathbf{u}_m : is the mixture velocity,
- ρ_d : is the dispersed gas phase density,
- \mathbf{u}_d : is the drift velocity of the dispersed gas phase, which is computed by a closure model
- μ_m : is the mixture molecular viscosity,
- ν_t : is the turbulent viscosity, which is computed via a mixing length model
- p_m : is the mixture pressure,
- \mathbf{g} : is the acceleration of gravity,
- \mathbf{f} : is a volumetric force, which comes due to friction with internal structures or due to momentum sources added at the pumps,
- e_m : is the mixture internal energy,
- H_m : is the mixture enthalpy,
- κ : is the thermal conductivity in the fluid, which is frequently a tensor in the porous media,
- T : is the temperature of the liquid-gas mixture,
- Pr_t : is the turbulent Prandtl number,
- \dot{q}_l''' : is the volumetric heat source deposited directly in the fluid, which, during steady-state operation of the MSR, is the power source due to fission and delayed nuclear power

Each of the mixture variables, e.g., ρ_m , is computed by mixture average as follows:

$$\rho_m = \alpha \rho_g + (1 - \alpha) \rho_l, \quad 3-7$$

where ρ_l is the density of the liquid phase. The mixture velocity is computed by preserving mass flow rates as follows:

$$\mathbf{u}_m = \frac{\alpha \rho_g \mathbf{u}_g + (1 - \alpha) \rho_l \mathbf{u}_l}{\rho_m}, \quad 3-8$$

where \mathbf{u}_l is the velocity of the liquid phase.

Finally, for species tracking, it is important to compute the interface area between the liquid and gas phases. In this work, this interface area ξ_g is determined as follows:

$$\xi_g = \frac{6\alpha}{d_g}, \quad 3-9$$

where this model assumes spherical bubbles of diameter d_g . In this work we take $d_g \approx 1mm$, which was the average bubble diameter observed for MSRE.

3.2.4. Salt Solidification and Melting

We augment the existing thermal–hydraulics with a liquid fraction $f_L \in [0,1]$, a latent heat L (J/kg), and a porous penalization in momentum. Solidus and liquidus are denotes as T_s and T_ℓ , respectively. The model has been implemented using kernels and auxiliary kernels from Pronghorn. The liquid fraction is updated as follows:

$$f_L = \begin{cases} 0 & \text{if } T \leq T_s, \\ \frac{T - T_s}{T_\ell - T_s} & \text{if } T_s < T < T_{ell}, \\ 1 & \text{if } T \geq T_{ell}. \end{cases} \quad 3-10$$

Once the solid fraction bounds defined, the enthalpy is redefined to add the latent heat as follows:

$$\begin{aligned} h(T) &= \int_T c_p(\theta) d\theta + L f_L(T) \\ c_{p,eff}(T) &= \frac{dh}{dT} = c_p(T) + L \frac{df_L}{dT} \end{aligned} \quad 3-11$$

Hence, allows to use the energy formulation in equation 3-6 for the energy conservation but adding a source term

$$\dot{q}_l''' = \frac{\partial \gamma L f_L(T)}{\partial t} + \nabla \cdot (\gamma^{-1} \mathbf{u}_m L f_L(T)) = \left[L \frac{\partial \gamma T}{\partial t} + L \nabla \cdot (\gamma^{-1} \mathbf{u}_m T) \right] \frac{df_L}{dT} \quad 3-12$$

Via the definitions in equations 3-11 and 3-12 a mushy zone is defined thanks for temperature difference between the solidus and liquidus temperature. Then, we blend thermal properties across the mushy zone as follows:

$$\begin{aligned} (\rho c_p)_{eff} &= f_L(\rho_\ell c_{p,\ell}) + (1 - f_L)(\rho_s c_{p,s}) \\ k_{eff} &= f_L k_\ell + (1 - f_L) k_s \\ D_{C_i eff} &= f_L D_{C_i,\ell} + (1 - f_L) D_{C_i,s} \end{aligned} \quad 3-13$$

Then the linear momentum is penalized across the mush zone to effectively stop the flow in the solid. This is done via a Darcy-like sink to the mixture momentum as follows:

$$\begin{aligned} \mathbf{s}_{mush} &= -\frac{\mu_m}{K_{f_L}} \mathbf{u}_m, \\ K_{f_L} &= \frac{d_c^2}{C_{ck}} \frac{f_L^3}{(1 - f_L)^2 + \epsilon} \end{aligned} \quad 3-14$$

with μ_m being the mixture dynamic viscosity, d_c is a characteristic length, e.g., the dendrite spacing, $C_{ck} \approx 180$ and $\epsilon \approx 10^{-3}$. Turbulence is suppressed in the mushy zone via a potential weighting of the effective turbulent viscosity as follows:

$$\nu_{t,eff} = f_L^n \nu_t, \quad n \in [1,2]. \quad 3-15$$

Finally, for the mushy zone, advection and transport are frozen as the salt solidifies. This is achieved suppress convection where solid as follows:

$$\mathbf{u}_m \leftarrow f_L \mathbf{u}_m \text{ in the advective fluxes}$$

3-16

3.3. Species Tracking, Chemistry, and Thermal Properties

3.3.1. Thermochemistry modeling

MSR thermochemistry is modeled using the Gibbs energy minimization (GEM) solver and thermochemistry library Thermochimica within the Chemical Reactions Module of MOOSE. Here, Thermochimica uses what's known as the Calculation of Phase Diagrams (CALPHAD) method to perform global minimization searches for the system's Gibbs energy and determine the thermochemical equilibrium of a chemical system given its temperature, pressure, and elemental composition. Outputs of Thermochimica include the chemical potential of the elements in the system such as the fluorine potential of the fuel-salt (i.e., redox potential), phase equilibrium, and phase precipitation. The thermochemistry model uses Thermochimica, which was described in the report written in FY24 by the group ([Shahbazi et al., 2024](#)). The reader is referred to this report for further details about the solution process.

It is important to highlight that the Thermochimica solve relies upon a database of Gibbs energy formulations and subsequent phase diagrams phases. In this work the Molten Salt Thermal Properties Database - Thermochemical (MSTDB-TC) v4.1 serves as the database for all thermochemical calculations. MSTDB-TC v4.1 is the most up-to-date thermochemical database and has many validated thermodynamic treatments of molten salt systems including the incorporation of zirconium and iodine bearing fuel salts which is important for all MSRs given their prevalence as FPs, but especially for MSRE which utilized a Zr-bearing fuel carrier salt. Therefore, utilizing Thermochimica with MSTDB-TC v4.1 enables multiphysics informed thermochemistry modeling of MSR systems with regard to determining the evolving redox potential of the fuel salt due to depletion. This aids in determining the volatility of elements and chemical species throughout reactor operation.

3.3.2. High-Fidelity Modeling of Species Transport

Species are tracked within the Pronghorn finite volume mesh. In this one, the concentration of a species of type i for a state x , named c_i^x , is modeled as a function of space and time. Note that the state x can either be liquid or gas and i will represent an isotope into our models.

The equation solved for the transport of species in the Eulerian frame reads as follows:

$$\begin{aligned} \frac{\partial c_i^x}{\partial t} + \nabla \cdot \left(\frac{\mathbf{u}_m}{\gamma} c_i^x \right) - \nabla \cdot \left[\left(D_{c_i} + \frac{\nu_t}{S c_t} \right) \nabla c_i^x \right] \\ = -\lambda_i c_i^x + \sum_j \lambda_{j \rightarrow i} c_j^x + \Sigma_{f,i} \phi(t) c_i^x - \sum_k \Sigma_{ik} \phi(t) c_i^x - h^{xy} (c_i^x - c_i^y), \end{aligned} \quad 3-17$$

where the following principles have been introduced:

- D_{c_i} : is the void fraction,
- h^{xy} : is the mass transfer coefficient between the liquid and gas phases

The species tracking equation encompasses various physical processes, with terms representing the time derivative, convective transport, molecular and turbulent diffusion, natural decay, transmutation, production via fission, destruction by nuclear reactions, and losses due to phase transfer. In MSRs, thermal hydraulics modeling plays a critical role in predicting the transport and distribution of isotopic

species within the reactor. The flow field, temperature gradients, and phase changes significantly influence the movement and accumulation of species. For instance, the deposition of fission or corrosion products on solid surfaces, the buildup of radioactive nuclides in cooler regions, and their transport across reactor zones are all dictated by thermal hydraulic conditions.

Accurate species tracking requires the coupling of neutronics and thermal hydraulics models. Neutronics dictates where fission reactions—and thus new species—are generated, while thermal hydraulics governs the transport and potential deposition of these species. Temperature gradients can induce thermophoretic forces that drive species to specific regions, while flow patterns can either enhance or inhibit their mixing.

The enthalpy-porosity approach, used to model phase changes, is particularly important in MSRs, where transient events may cause solidification of the fuel salt. This solidification can trap species within solidified regions, affecting their transport and potentially leading to localized concentrations of radioactivity. Accurately capturing these phase changes and their impact on species distribution is essential for understanding the behavior of radioactive materials in the reactor and ensuring safe and efficient operation.

3.3.3. Phase Diagram Verification

The verification of the MOOSE-wrapped version of Thermochimica is performed for the NaCl-UCl₃ system, which is the fuel salt utilized in the L-MSR concept. The reference diagram is provided in Figure 3-6.

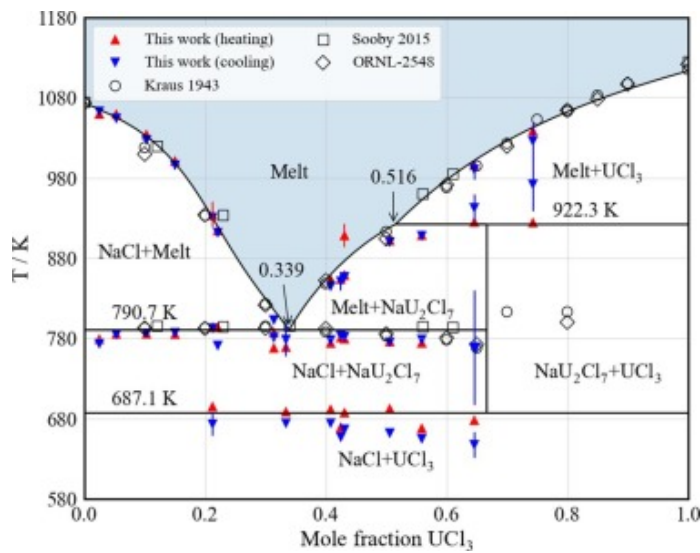


Figure 3-6. NaCl-UCl₃ phase diagram used for verification of the Thermochimica calculations (Yingling et al., 2023).

A MOOSE simulation is setup in a cartesian grid, varying the temperature in the y-axis and the UCl₃ concentration in the x-axis. Hence, each point in the grid corresponds to a different concentration in the phase diagram. Then, for each point in the grid, a Thermochimica calculation is performed to predict the stable phases and their phase fraction. The results obtained are depicted in Figure 3-7 for the four main stable phases predicted by Thermochimica.

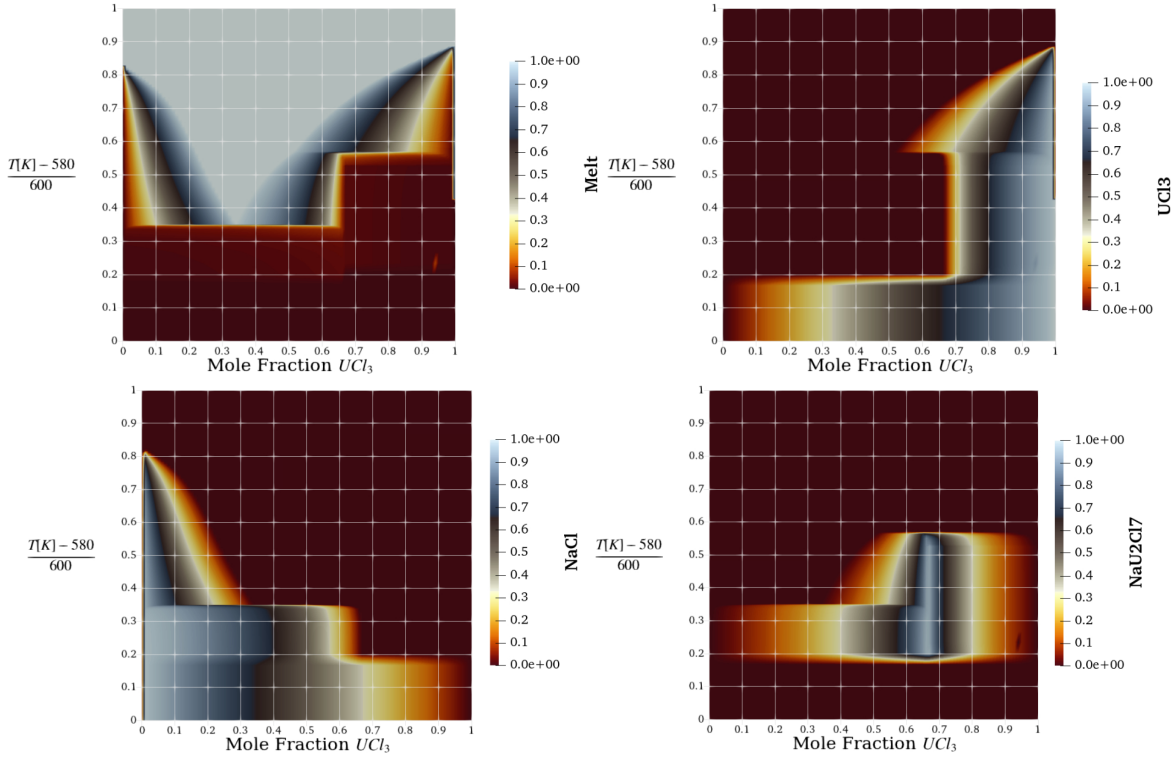


Figure 3-7. Table phase fractions predicted by the MOOSE Thermochemica for the $\text{NaCl}-\text{UCl}_3$ phase diagram.

By visual comparison, one can see a very good agreement between the reference phase diagram in Figure 3-6 and the stable phases predicted by Thermochemica in Figure 3-7. In particular, one can see that the liquid phase follows the same quantitative pattern than the reference diagram and correctly predicts the binary mixture regions with solid NaCl and UCl_3 . Additionally, the solid fraction of NaCl and UCl_3 above and below the eutectic temperature are also correctly predicted. Finally, Thermochemica also predicts correctly the appearance of the NaU_2Cl_7 phase below the eutectic point.

3.3.4. Saline

Thermophysical properties of salts are provided by Saline (Henderson et al., 2021), a MOOSE-based API that integrates quality-assured fits from the Molten Salt Thermal Properties Database—Thermophysical (MSTDB–TP) (Termini et al., 2023). The *SalineMoltenSaltFluidProperties* UserObject exposes these properties to MOOSE applications and returns density (ρ), viscosity (μ), thermal conductivity (k), isobaric heat capacity (c_p), and enthalpy (h), along with the derived thermal diffusivity ($\alpha = k/\rho c_p$) as functions of temperature (T) and composition vector (x_c) of salt components. Although pressure is included as an argument in the API, it has no effect on these nearly incompressible liquids. Saline is distributed as a submodule within the MOOSE Fluid Properties module, supporting direct ingestion of MSTDB–TP property tables and correlations.

MSTDB–TP aggregates referenced values and empirical relations for melting/boiling points, density, viscosity, heat capacity, and thermal conductivity of fluoride and chloride salts, both pure and in mixtures. Version 3.0.x documents contain data for hundreds of salt entries, including pseudo-binaries and ternaries, with reported validity ranges and uncertainties (Termini et al., 2023). Saline reads these data and exposes them through a stable C++/Fortran interface. Unless specified otherwise, all functions are isobaric ($P \approx \text{const}$) and temperature dependent.

For specific compositions, MSTDB–TP provides linear or low-order polynomial fits $\rho(T) = a_0 + a_1 T [+ a_2 T^2]$. Units follow the database entry, with the MOOSE wrapper converting to SI units. For arbitrary compositions, Saline can apply Redlich–Kister (RK) composition expansions with a linear-in-T interaction parameter $L_j(T) = A_j + B_j T$; ternary (and higher) mixtures are interpolated using the Muggianu scheme.

Temperature dependence is provided by tabulated fits per system, such as Andrade or Arrhenius-type forms. For ideal composition mixing, $\log \mu(x) = \sum_i x_i \log \mu_i$; non-ideal corrections may be supplied via RK when available.

Simple linear fits $k(T) = a + bT$ are provided where data support them. Saline includes the source and uncertainty with the fit from MSTDB–TP. Users should note that conductivity data are comparatively sparse and heterogeneous across sources.

MSTDB–TP supplies polynomial heat capacity fits of the form $c_p(T) = A + B T + C T^{-2} + D T^2$ for the liquid state. Enthalpy $h(T)$ is evaluated by integrating c_p from a reference temperature embedded in the data set. Saline exposes both c_p and h .

Saline’s *Default_Data_Store* serves property fits at specific compositions from MSTDB–TP. An optional *R_Kister_Data_Store* extends to arbitrary compositions using RK expansions built from underlying binaries. As of the referenced implementation, density is the most mature property in this path, while other properties may fall back to ideal mixing with unquantified uncertainty.

Each entry in MSTDB–TP includes the source reference, temperature validity window, and an estimated variance/uncertainty; these metadata are preserved in the Saline property files (*.prp) used by MOOSE. Current Saline releases expose the values and ranges; users should avoid out-of-range evaluations or treat them as extrapolations.

The *SalineMoltenSaltFluidProperties* object is configured with component names and mole fractions. It reads a .prp file in the Saline format and provides properties and derivatives to Materials and Kernels. The object includes a small Newton solve for variable-set conversions (e.g., $(p, h) \rightarrow (p, T)$) with user-set tolerances and can be enabled alongside other FluidProperties in coupled calculations.

In summary, Saline + MSTDB–TP supplies traceable, uncertainty-aware correlations for ρ, μ, k, c_p , and h over the temperature/composition ranges of interest, with optional RK-based composition interpolation. This integration allows thermal-hydraulic (TH) and two-phase models to use consistent, database-backed properties within the MOOSE framework.

3.3.5. Chemistry-Informed Neural-Network Predictions of Thermophysical Properties

A major challenge to MSR development is the sparsity of data for molten salt thermal properties, which can be challenging to measure experimentally (Porter et al., 2022). Nuclear applications of specific salt systems and compositions rely heavily on the system’s thermophysical and thermochemical properties; thus, there is a need for both a functional database of properties as well as a computational tool to analyze and predict thermal properties of molten salt mixtures.

In an effort to compile the available data on molten salts, the Molten Salt Thermal Properties Database (MSTDB) was created and is managed by ORNL (MSTDB, 2025), in part by the NEAMS program. This database contains two branches of property data: thermochemical (MSTDB-TC) (Besmann et al., 2024)(Besmann & Pinto, 2021) and thermophysical (MSTDB-TP) (Termini et al., 2023). The latter branch, MSTDB-TP, tabulates data on the boiling point, melting point, density, viscosity, thermal conductivity, and heat capacity of many salt compositions including pure compounds, pseudobinary systems, pseudoternary systems, and higher-order systems of molten salt mixtures in various mass ratios

(Termini et al., 2023). MSTDB-TP v3.0 contains 799 unique compositions spanning 97 systems of endmembers (Termini et al., 2023), although data does not exist for all properties and all of these compositions. Table 3-7 below shows the number of compositions for which data exists and how many of the 799 compositions are missing for each property. The large amount of data that is still missing from MSTDB-TP is an indication of the time-consuming and difficult nature of molten salt property measurements, motivating the development of predictive modeling tools.

Table 3-7. Available Properties in MSTDB-TP.

Property	Available	Missing
Boiling Point	33	766
Melting Point	654	145
Density	627	172
Viscosity	393	406
Thermal Conductivity	18	781
Heat Capacity	31	768
Total Compositions	799	
Total Salt Systems	97	

With the advent of artificial intelligence, various machine learning (ML) algorithms, such as artificial neural networks (ANNs), have been used in connection to molten salt research. ML techniques have been successfully applied to molten salt simulations of thermophysical properties, and many studies have utilized physics-informed ML (Porter et al., 2022), but another potential approach is to develop a basic neural network as a rapid predictive tool for molten salt thermal properties.

Consequently, the current study addresses data sparsity by using ML to (1) predict and (2) analyze molten salt thermal properties in MSTDB-TP v3.0. Based on these two foci, the objectives were outlined as follows: design and implement streamlined preprocessing with Python, develop a basic neural network for property predictions, and analyze relations between thermal properties.

The molten salt compositions and corresponding thermal properties were obtained from MSTDB-TP v3.0 (Termini et al., 2023). The properties included boiling point, melting point, density, viscosity, thermal conductivity, and heat capacity. The database contained 799 unique compositions spanning 97 systems of endmembers (Termini et al., 2023). Density, viscosity, thermal conductivity, and heat capacity were calculated over 5 temperatures for the single-label regression model. The temperature-dependent equations, listed below, are Eq. 3-18 for density, Eqs. 3-19 and 3-20 for viscosity, Eq. 3-21 for thermal conductivity, and Eq. 3-22 for molar heat capacity.

$$\rho = A - B T \quad 3-18$$

$$\mu = A \exp\left(\frac{B}{R T}\right) \quad 3-19$$

$$\mu = 10^{(A+B/T+C/T^2)} \quad 3-20$$

$$k = A + B T \quad 3-21$$

$$C_m = A + B T + C T^{-2} + D T^2$$

3-22

where ρ (g/cm³) is density, μ (cP) is viscosity, k (W/m-K) is thermal conductivity, C_m (J/K-mol) is molar heat capacity, and R (J/K-mol) is the universal gas constant (8.314 J/K-mol). A , B , C , and D are coefficients listed for each property per salt composition in MSTDB-TP. Viscosity was linearized before feeding into the neural network by taking the natural log of Eq. (2) or Eq. (3) to improve model performance.

To enable a basic neural network to recognize the chemistry and physics of molten salts, a novel input called a “feature matrix” was designed. The following atomic characteristics were added: atomic number, molar mass, electronegativity, polarizability, atomic radius, ionic charge, mole fraction, and temperature. The atoms in each salt system and their atomic features were formatted into a feature matrix, as illustrated in Figure 3-8. Each salt composition was described with a single feature matrix and the associated properties. Atomic features were obtained using the Python package, Mendeleev ([Mentel, 2014](#)). All features and properties were scaled to a mean of zero and unit variance using StandardScaler from Scikit-learn ([Pedregosa et al., 2011](#)).

Atomic Features

The diagram shows a table titled "Atomic Features". To the left of the table, there is a vertical double-headed arrow labeled "Atoms" pointing up and down. Above the table, there is a horizontal double-headed arrow pointing left and right, spanning the width of the table's columns. The table itself has 9 columns and 10 rows. The columns are labeled: Atomic Number, Molar Mass, Electronegativity, Polarizability, Atomic Radius, Ionic Charge, Mole Fraction, and Temperature. The first row contains numerical values for these features. Subsequent rows contain mostly zeros, except for the last row which contains non-zero values for Temperature (469), Mole Fraction (0.25), and Ionic Charge (-1).

Atomic Number	Molar Mass	Electronegativity	Polarizability	Atomic Radius	Ionic Charge	Mole Fraction	Temperature
0	133.3405	0	0	0	0	0	469
13	26.981539	1.61	57.8	125	3	0.25	0
17	35.45	3.16	14.6	100	-1	0.75	0
0	0	0	0	0	0	0	0
0	0	0	0	0	0	0	0
0	0	0	0	0	0	0	0
0	0	0	0	0	0	0	0
0	0	0	0	0	0	0	0
0	0	0	0	0	0	0	0

Figure 3-8. Example of a feature matrix that represents the input data for a single molten salt composition. Each row is a single atom in the salt system while each column is an atomic feature of the atoms.

The feature matrix method required a machine learning algorithm that accepts matrices as inputs. Convolutional neural networks (CNNs) are traditionally used for image recognition with 3D inputs, and newer 1D CNNs are often applied to sequential data such as time series ([Kiranyaz, 2023](#)) ([Ige Sibiya, 2023](#)). A 1D CNN was selected to take advantage of the relations between cation-anion pairs of the ionic compounds. Built with TensorFlow and Keras, the ML model architecture consisted of two 1D convolutional layers (kernel size = 2, filters = 128, 64) followed by 1D global max pooling and two dense layers with a 20% dropout layer in between. Leaky ReLU was the activation function.

The models were trained with the Adam optimizer (learning rate = 0.001) and a batch size of 64 for a maximum of 500 epochs. During backpropagation, mean squared error (MSE) was the loss function, and mean absolute error (MAE) was an additional metric. Single-label regression predicted one property at a time from one node.

General training behavior was monitored by learning curves with randomly split 90-10% training-validation datasets. Results from 2 iterations of 10-fold cross-validation assessed the performance of the models by training on 90% of the data. Learning rate reduction (factor = 0.2, patience = 15) dynamically adjusted the learning rate, and early stopping (patience = 25) was employed to prevent overfitting. The best-performing model from cross-validation was saved and used to predict the remaining 10% of unseen property data to evaluate the model’s generalizability. Along with MSE and MAE, performance metrics

included R², mean absolute percentage error (MAPE), *weighted absolute percentage error (WAPE) for viscosity, and root mean squared error (RMSE).

To aid in interpreting the CNN models and potential property relations, feature ablation studies were conducted. Feature importance analysis was used in conjunction with feature ablation to observe trends from single-label regression.

Entire atomic feature columns were set to zero for the single-label regression models. If the performance error increased when predicting the 10% test dataset after a feature was removed in this way, that feature was considered relatively important for predicting the property. For feature importance analysis, the same procedure was followed, though the features were shuffled randomly instead of set to zero. Ablation simulated removal of that feature while permutation preserved the distribution but broke any correlations with the permuted feature.

To analyze relations between temperature-dependent properties, multi-label regression models were trained on density, viscosity, thermal conductivity, and heat capacity. Spearman rank correlations were computed between the four properties to further evaluate any relations.

Separate ML models were trained to predict the six thermal properties from MSTDB-TP: boiling point, melting point, density, viscosity, thermal conductivity, and heat capacity. Given sufficient data, the results demonstrate that a 1D CNN with feature matrices as inputs can predict these thermal properties with accuracy and generalizability.

The model specific to each property was assessed on 90% of the data by performing 2 iterations of 10-fold cross-validation, and the results are summarized in Table 3-8. The number of samples are listed, which were expanded over 5 temperatures for density, viscosity, thermal conductivity, and heat capacity. Figure 3-9 (a)-(f) displays the parity plots of predicted vs. observed values from cross-validation. The average R² value for all properties except boiling point was >0.90, as shown in Table 2. At the same time, average MAPE (WAPE for viscosity) was <10% aside from boiling point. These results indicate that the models' general performances were relatively accurate. The boiling point model may be less accurate due to the lack of samples as compared to the other properties.

Table 3-8. Summary of 10-Fold Cross-Validation for Single-Label Regression.

Properties		10-Fold (x2) Cross-Validation	
Name	Samples	Avg. R2	Avg. MAPE (%)
Boiling Point	30	-6.064 ± 20.245	15.042 ± 9.727
Melting Point	589	0.907 ± 0.038	4.355 ± 0.650
Density	560 x 5	0.996 ± 0.001	1.604 ± 0.180
Viscosity	337 x 5	0.984 ± 0.014	9.036 ± 1.644*
Thermal Conductivity	16 x 5	0.960 ± 0.033	8.560 ± 6.074
Heat Capacity	27 x 5	0.976 ± 0.021	2.472 ± 0.967

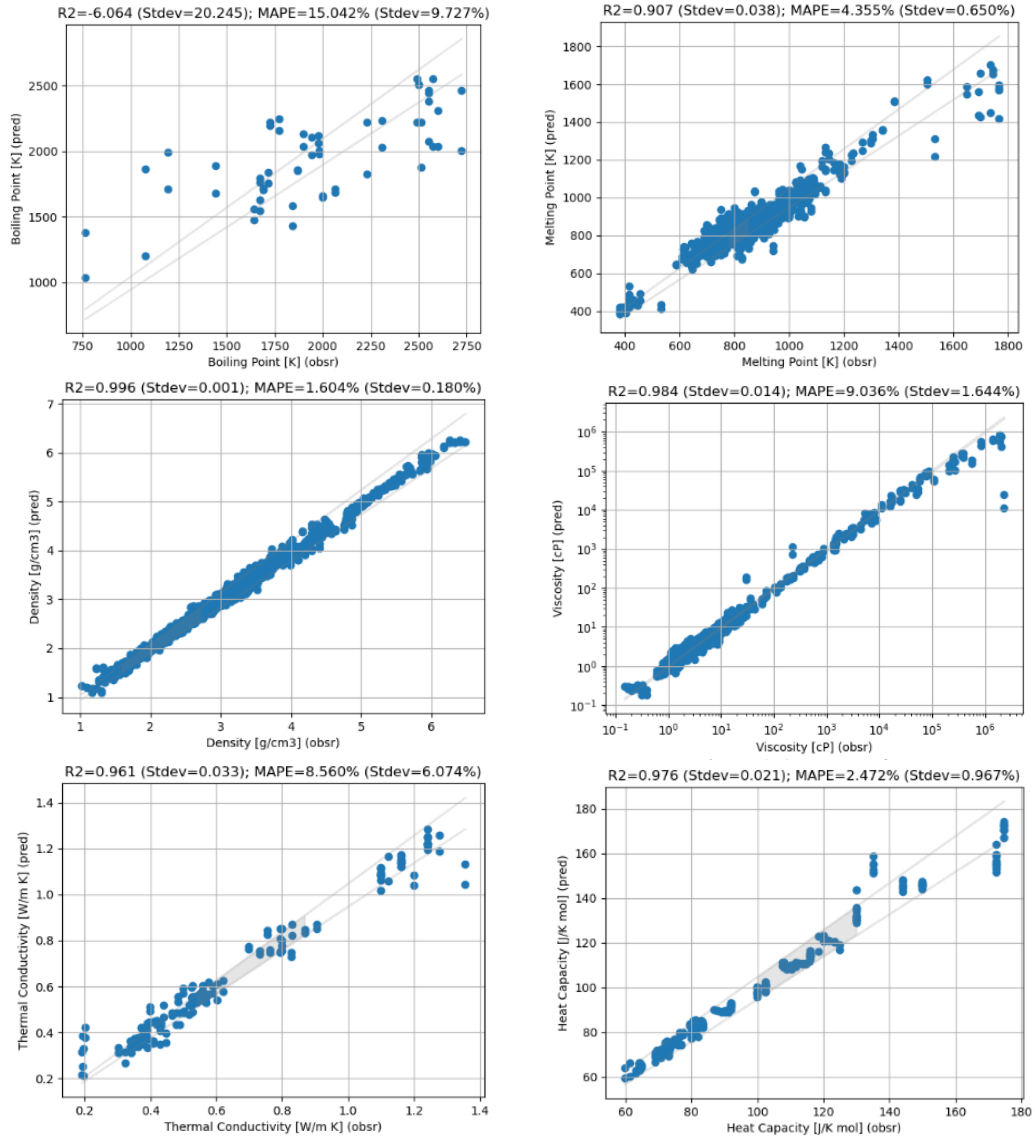


Figure 3-9. 10-fold cross-validation parity plots of predicted vs. observed values across folds for (a) boiling point, (b) melting point, (c) density, (d) viscosity, (e) thermal conductivity, and (f) heat capacity.

To assess the generalizability of the models, the remaining 10% of the data, which the models had never seen, was fed to the models for making predictions. The models with minimized loss were selected from cross-validation for the 10% property predictions, and the predicted properties were compared to the true values. Table 3-9 and Figure 3-10 contain the results from the test set predictions. R² values were >0.80 for boiling point and melting point and >0.90 for the temperature-dependent properties. Additionally, MAPE (WAPE for viscosity) was <10% for all properties. Since accuracy remained high for unseen data, the models are generalizable and not overfit.

Table 3-9. Summary of 10% Test Set Predictions for Single-Label Regression

Properties		10% Test Set Predictions	
Name	Samples	R2	MAPE (%)
Boiling Point	3	0.803	8.533
Melting Point	65	0.826	4.533
Density	62 x 5	0.996	1.572
Viscosity	37 x 5	0.983	8.916*
Thermal Conductivity	2 x 5	0.943	8.554
Heat Capacity	3 x 5	0.923	4.863

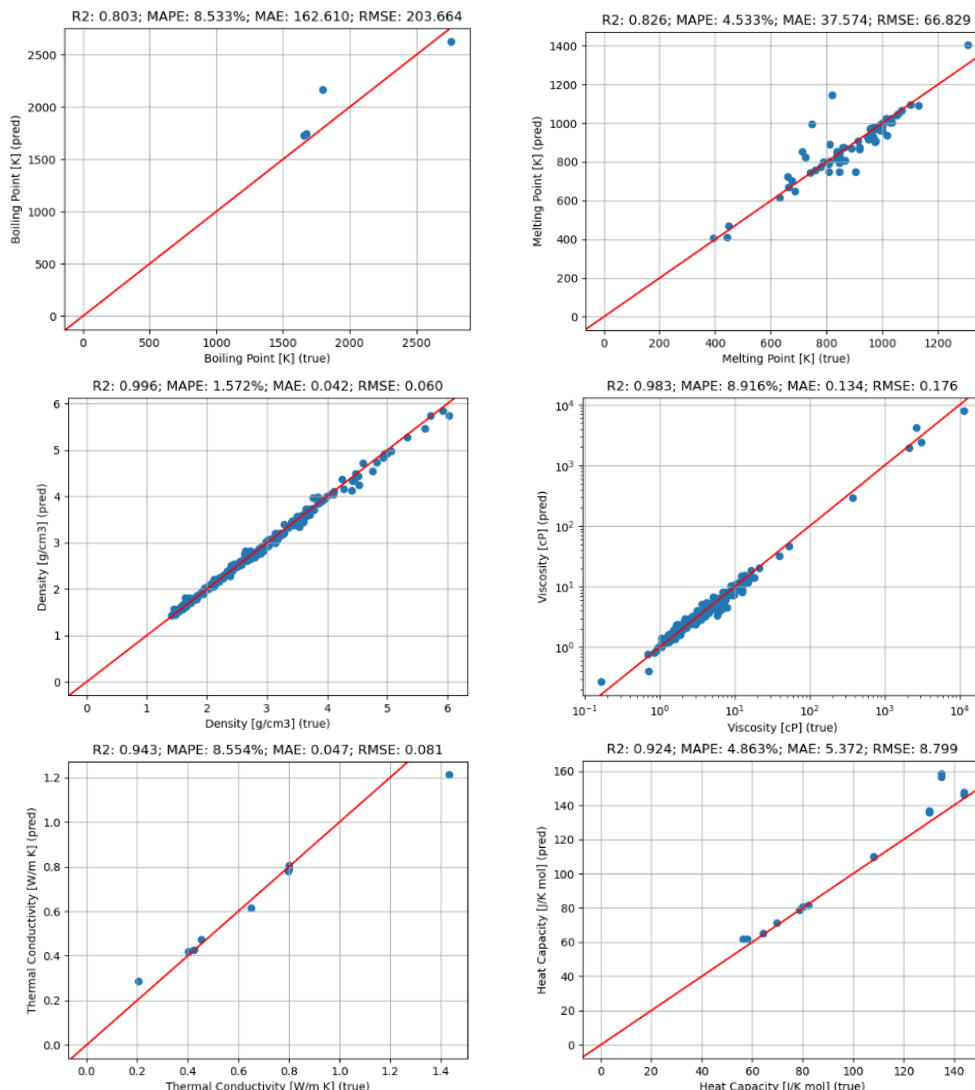


Figure 3-10. 10% test set parity plots of predicted vs. true values on unseen data for (a) boiling point, (b) melting point, (c) density, (d) viscosity, (e) thermal conductivity, and (f) heat capacity.

One caveat is that the temperature-dependent properties were computed over 5 temperatures per salt composition. Thus, it is highly likely that the randomly selected 10% test sets contain the same salt systems that the models have trained on, yet at different temperatures. As a future step, a more rigorous assessment would be to place entire salt systems across all 5 temperatures in the test sets.

The same models used for the 10% test set predictions were implemented for the ablation and permutation studies. The models' degradations in performance were calculated by comparing the MAPE on the 10% test set predictions with the ablated/permuted feature to the baseline MAPE without any ablation or permutation. A larger MAPE indicated that the ablated/permuted feature was relatively important for accurately predicting the property.

One at a time, the atomic features were set equal to zero for the ablation study but were shuffled 10 times for the permutation importance study. Figure 3-11 displays the ablation and permutation results, where a longer bar corresponds to a more important feature, and illustrates how the six thermal properties rely on different atomic features. Based on both ablation and permutation, mole fraction is the first or second most important feature for 4 properties (not including boiling point and density), and ionic charge is the first/second highest importance for 3 out of 6. Polarizability is the least important for all properties except melting point, in which the feature is second to least.

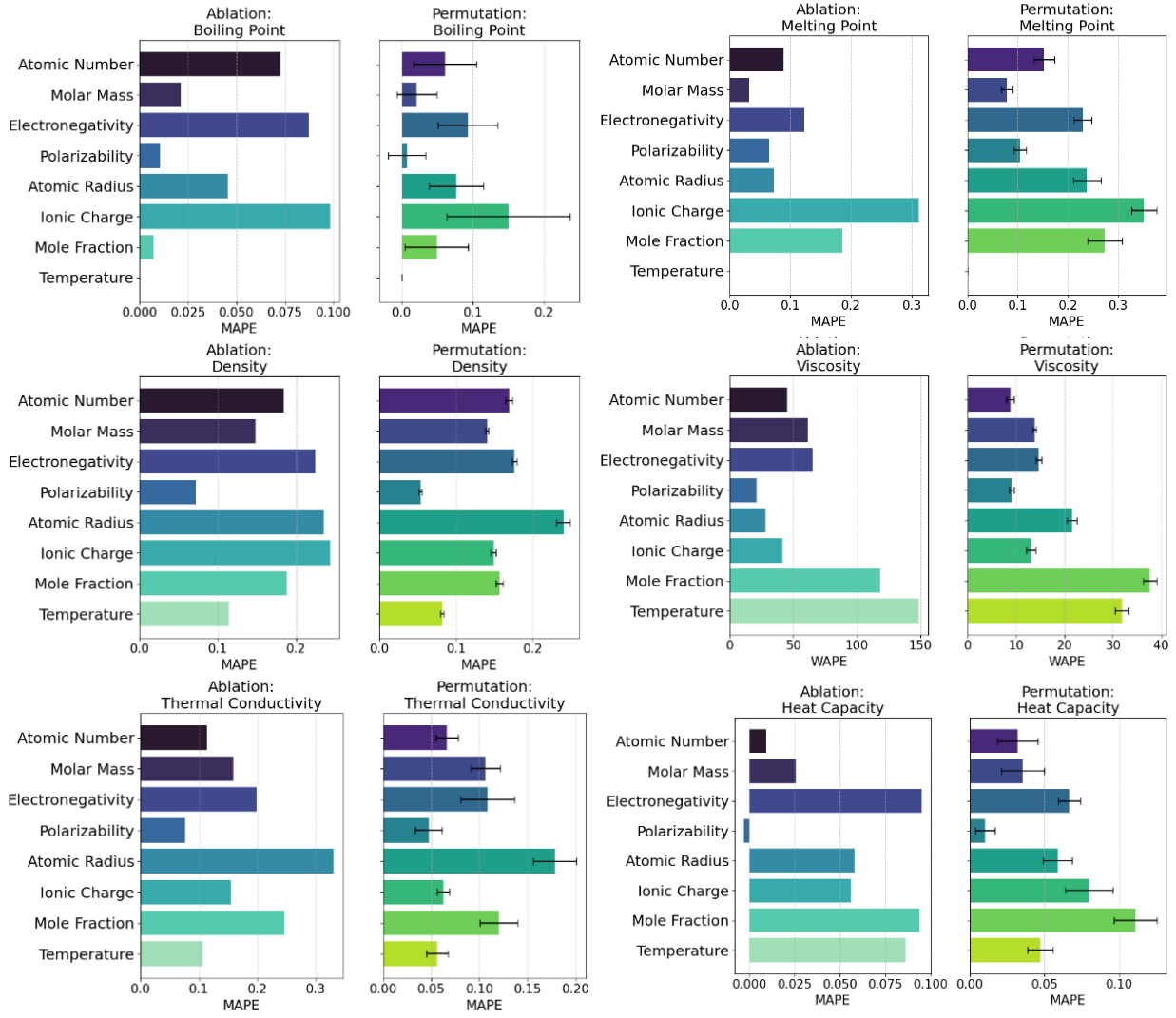


Figure 3-11. Feature ablation (left) and permutation importance (right) for (a) boiling point, (b) melting point, (c) density, (d) viscosity, (e) thermal conductivity, and (f) heat capacity. The y-axis lists the ablated/permuted features, and the x-axis shows the change in model error when the feature is removed/shuffled.

Comparing the results between ablation and permutation adds meaning. If a feature is important in both, that feature is highly depended upon for predictions. If a feature has higher importance in ablation than permutation, that feature may have a unique signal unrelated to other features; removing it causes a larger disruption than simply shuffling. On the other hand, if a feature has lower importance in ablation than permutation, that feature may be closely correlated with other features; removing it allows the model to rely on the correlated features whereas shuffling breaks the correlations. For instance, temperature always has a higher ablation MAPE than permutation, indicating the model recognizes temperature as a distinctive signal from the other features.

To aid in understanding the relationship between different thermophysical properties, Spearman rank correlations were computed between density, viscosity, thermal conductivity, and heat capacity. A positive (negative) correlation indicates the two properties are monotonically increasing (decreasing). Figure 3-12 shows a correlation heatmap on the 12 salt compositions for which data exists for all properties.

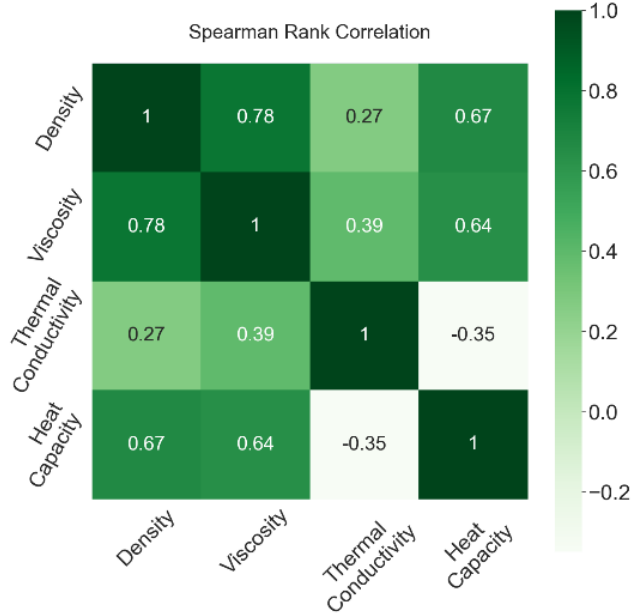


Figure 3-12. Spearman rank correlation heatmap for the temperature-dependent properties.

Density and viscosity have a strong monotonically increasing relation. Heat capacity with density and with viscosity are moderate monotonically increasing relations, though heat capacity with thermal conductivity is a weak monotonically decreasing relation. Finally, viscosity and thermal conductivity have a weak monotonically increasing relation. Overall, these correlations reveal non-linear relations across the properties. Further analysis with multi-label regression may enable a deeper understanding of how these properties are related for molten salts.

In summary, this study developed a new method for predicting molten salt thermal properties using a basic 1D CNN with feature matrices as the input. Predicted vs. true values from single-label regression consistently showed $R^2 > 0.90$ and MAPE < 10%, provided enough samples from MSTDB-TP. Lastly, usage of multi-label regression may offer insights on property correlations and relationships. Ultimately, this study aims to support the development of a tool for predicting molten salt thermal properties. To this end, data currently missing from MSTDB-TP could be populated with the models' predictions and the updated database may then be used to pinpoint potentially useful characteristics of currently unknown molten salt systems.

4. Integral Effects Modeling of the Thermal-Spectrum Molten Salt Reactor Experiment

4.1. Introduction

The Molten Salt Reactor Experiment (MSRE), conducted in the 1960s at Oak Ridge National Laboratory, provided essential data on molten-salt reactors (MSRs) that use liquid fuel. MSRs require complex modeling due to their unique fuel dynamics and significant thermal feedback. Recent interest in MSRs has led to the development of advanced modeling tools, including SAMOFAR, SAMOSAVER, EVOL, GeN-Foam, MCNP, and Serpent. INL is contributing by coupling thermal-hydraulics codes Pronghorn and SAM with the neutronics solver Griffin, validated against MSRE pump transients. Two neutronics tools are evaluated in this comparison: Griffin, which is the main reactor physics tool being evaluated, and Squirrel, which is a MOOSE-based point kinetics solver developed at the Technical University of Denmark and is evaluated as an alternative to accelerate transient simulation once the point kinetic parameters are developed. Both Griffin and Squirrel are coupled to Pronghorn for the transient MSRE modeling.

4.2. Description of the MSRE Models

The Molten Salt Reactor Experiment (MSRE) was an experimental thermal spectrum reactor operated at Oak Ridge National Laboratory in the 1960s. It was designed to study the feasibility and behavior of molten-salt reactors (MSRs) using liquid fuel. The MSRE utilized a unique design where the fuel was dissolved in a molten salt mixture that flowed through the reactor core, interacting with a graphite moderator. The key reactors specifications are outlined below:

- Design Core Power: 8 MWth
- Core Height: 1.39 meters
- Core Diameter: 1.63 meters
- Fuel Salt Composition: Lithium fluoride (LiF), beryllium fluoride (BeF₂), zirconium fluoride (ZrF₄), and uranium tetrafluoride (UF₄)
- Fuel Enrichment: ²³⁵U (initially), later replaced with ²³³U
- Core Inlet Temperature: 905 K
- Core Outlet Temperature: 928 K
- Fuel Circulation Time: 25.2 seconds

The MSRE's layout included several key components:

- Graphite Moderator: The reactor core consisted of vertical graphite stringers with cross-sections measuring 5.08 by 5.08 cm. The fuel salt flowed through rectangular channels within these graphite stringers, each channel measuring 3.05 by 1.016 cm with rounded corners.
- Core and Plenum: The core was surrounded by a lower plenum (0.12954 meters high) and an upper plenum (0.21336 meters high). These plenums facilitated the distribution and collection of fuel salt.
- Primary Circuit: The primary circuit included the core, the primary heat exchanger, and the external loop. The external loop allowed the fuel salt to circulate and transfer heat to a secondary coolant.

Figures illustrating the MSRE layout and core configuration are provided in Figure 4-1.

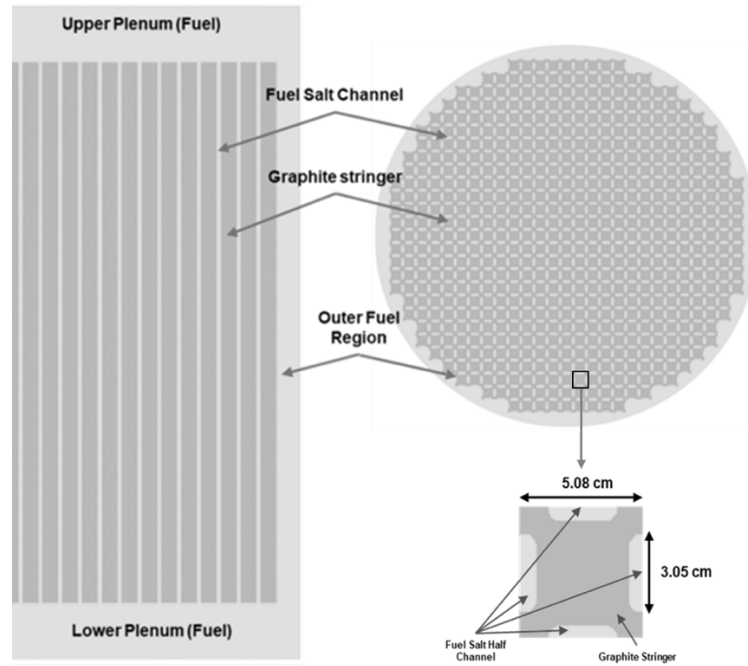


Figure 4-1. Axial (left) and radial (top right) views of the MSRE core assembly, and lattice of graphite stringers with 4-halves fuel salt channels (bottom right) [Robertson, 1965].

The MSRE used a FLiBe-based fuel salt, which was composed of lithium fluoride (LiF), beryllium fluoride (BeF₂), zirconium fluoride (ZrF₄), and uranium tetrafluoride (UF₄). The atomic fractions of the fuel salt isotopes for both ²³⁵U and ²³³U fuels are shown in the Table 4-1.

Table 4-1. Relative isotopic atomic fractions during the ²³³U and ²³⁵U loads of MSRE [Jaradat & Ortensi, 2023].

Isotope	²³⁵ U Fuel Loading	²³³ U Fuel Loading
Li-7	2.634E-01	2.618E-01
F-19	5.948E-01	5.936E-01
Be-9	1.179E-01	1.229E-01
U-233	—	4.977E-04
U-234	—	3.118E-05
U-235	1.203E-03	3.778E-06
U-238	2.443E-03	1.069E-06
Zr-90	1.042E-02	1.085E-02
Zr-91	2.273E-03	2.366E-03
Zr-92	3.474E-03	3.616E-03
Zr-94	3.521E-03	3.665E-03
Zr-96	5.673E-04	5.904E-04

The thermophysical properties of the fuel salt and graphite moderator are essential for accurate modeling. Table 4-2 summarizes these properties.

Table 4-2. Thermophysical properties of the fuel salt and the moderator.

Parameter [Units]	Fuel Salt	Graphite
Density [kg/m ³]	2,263 – 0.478 (T[K] – 923.0)	1,860.0
Thermal Conductivity [W/(m.K)]	1.4	40.1
Specific Heat [J/(kg.K)]	1868.0	1757.3
Dynamic Viscosity [Pa.s]	0.008268	-

4.2.1. SAM-based MSRE Model

FY24 work on Xenon transport calculation has provided insight on the capabilities in the NEAMS tool that needs improvement. The main capability update needed includes the Xenon transfer between the liquid and the gas phase and between the liquid and the solid phase in the core. The Xenon-carrying bubble transport is also needed to capture the different Xenon transport phenomena.

Throughout FY25, all the capabilities were added or improved to model the Xenon transport in more detail. Based on these code improvements, the Xenon transport model was significantly updated. The MSRE data was obtained for steady state Xenon poisoning effect at different void fractions. The updated Xenon transport model was then used to calculate the Xenon poisoning effect and to preliminarily validate against the experimental data.

The main model update is on the SAM MSRE model. The overall model is presented in Figure 4-2. The main update includes the incorporation of the bubble transport and the salt-to-bubble mass transfer model that are currently added to SAM (Mui et al. 2024). It also includes the updated Xenon diffusion model in the graphite(Travis Mui and et. al 2025). In general, the MSRE Xenon transport model consists of four parts that can have major impact on the Xenon poisoning estimation, including the Griffin core model for reactivity estimation based on the Xenon concentration, the SAM MSRE core model, the SAM MSRE pump model, and the other components model in the MSRE primary loop. The detailed removal and production terms in the MSRE model are described below.

The SAM core model consists of four channels in the core, the upper plenum, and the lower plenum. Significant fissions occur in these regions, which lead to the generation of I-135 and Xe-135. The power fraction calculated from Griffin is listed in Table 4-3.

The I-135 and Xe-135 production rates are proportional to the power assigned in the corresponding SAM component. The proportionality depends on the fission yields of the relevant isotopes, which differ for U-233 and U-235 fissions. Both cases are investigated, and the corresponding fission yield data are listed in Table 4-4. Both Te-135 and Xe-135m have relatively short half-life, so their fission yields are combined with I-135 and Xe-135. This reduces the number of species need to be tracked in the SAM model.

The removal terms for I-135 and Xe-135 in difference phases in the MSRE core include the decay and absorption. The absorption rate (normalized by atomic density) for Xe-135 is 2.79E-5 s⁻¹ in the fuel salt and bubble and is 2.90E-5 s⁻¹ in the graphite. I-135 decaying to Xe-135 in the salt is also a production term for Xe-135 in the salt.

Two transfer mechanisms for Xe-135 are modeled, including the transfer between the fuel salt and the bubble, as well as the transfer between the fuel salt and the core graphite. The Xe-135 transfer from the bubble to the graphite is not modeled. I-135 transfer among the different phases is not modeled as I-135 is not expected to present in the bubble significantly.

Table 4-3. Power distribution in the core and upper/lower plenum of the SAM model

Region	Power fraction
Upper plenum	0.0535
Channel 1 ^a	0.0973
Channel 2	0.2495
Channel 3	0.4239
Channel 4	0.1245
Lower plenum	0.0513

a. Channel 1 – 4 are arranged from center to periphery, with Channel 1 at the center.

Table 4-4. Fission yield data for Xe-135 production chain for U-235 and U-233 fission.

Isotope	U-235 fission	U-233 fission
Te-135	3.23%	1.69%
I-135	2.93%	3.30%
Xe-135	0.08%	0.42%
Xe-135m	0.15%	0.81%

The Xe-135 concentration in the different components of the SAM model is transferred to the Griffin model in the corresponding region with proper normalization. Only two Griffin runs are needed for the steady state calculation: one with no Xe-135 present in the core (typically time 0), and the other at the equilibrium state. The difference in the eigenvalue between the two cases is the reactivity change due to Xenon poisoning.

Xe-135 in the graphite has larger reactivity feedback than that in the fuel salt or bubble. The reactivity feedback coefficients calculated from standalone Griffin runs are listed in Table 4-5.

Table 4-5. Reactivity feedback coefficient (pcm per change of Xe-135 atomic density) for Xe-135 concentration

	U235	U233
graphite	-1.05E+13	-1.59E+13
fuel	-3.60E+12	-5.79E+12

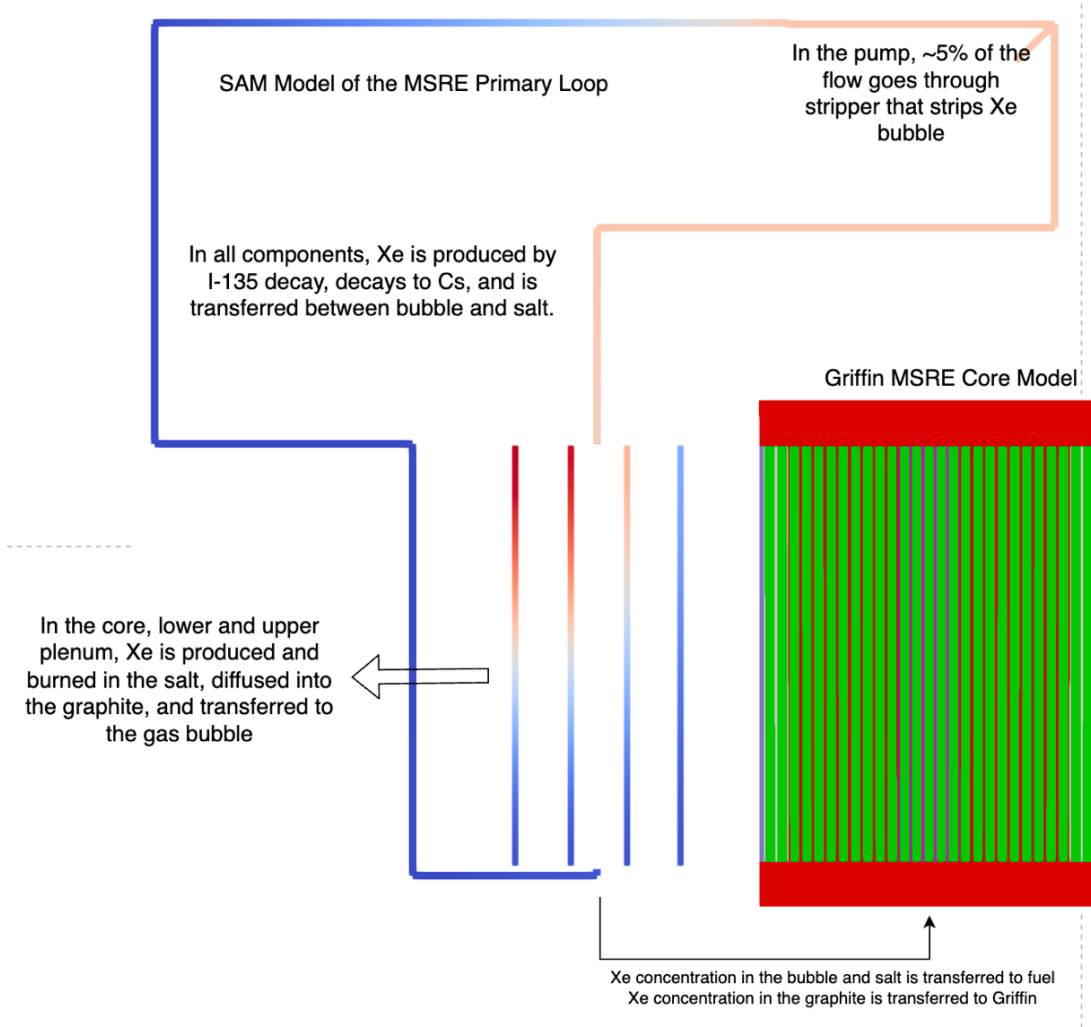


Figure 4-2 Xenon transport model for MSRE primary loop.

The pump model in SAM needs special attention as this is the main place where the Xenon-containing bubble is stripped from the fuel salt and is removed to the off-gas system. Reference (Robertson 1965), (Guymon 1973), (Engel et al. 1969) provide detailed information about the MSRE pump design. The major flow paths in the pump are indicated in Figure 4-3. The green arrows in the figure indicate the fuel salt flow paths (1200 gpm). A small fuel stream (50 gpm) (Kedl and Houtzel 1967), (Engel and Steffy 1971) is diverted to the spray ring as indicated by the blue arrows in the figure, within which the Xenon-containing bubbles are stripped from the fuel salt. The bubble-stripped fuel salt drops down to the main salt stream.

The bubble stripper is explicitly modeled in SAM. The form loss is adjusted to set the flow rate into the stripper. The Xe-135 removal term due to bubble stripping is given by

$$\text{Stripping rate} = v_g \alpha A C_{g,phase} \eta, \quad 4-1$$

where v_g is the bubble velocity. α is the void fraction. A is the flow area. $C_{g,phase}$ is the Xe-135 concentration in the bubble. η is the stripping efficiency of the bubble in the spray ring. The sink term in the SAM model of the spray ring needs to be volumetric. Thus, the stripping rate needs to be divided by the component volume. The final volumetric removal rate is

$$\text{Volumetric stripping rate} = v_g C_g \eta / l_{\text{stripper}},$$

4-2

C_g is the concentration of Xe-135 in the bubble averaged over the whole flow area, and l_{stripper} is the length of the stripper. This rate is specified as a function with v_g and C_g obtained from the postprocessors, i.e., the previous-time-step quantity.

The other removal and production terms include the isotope decay, the mass transfer between the salt and the bubble phase.

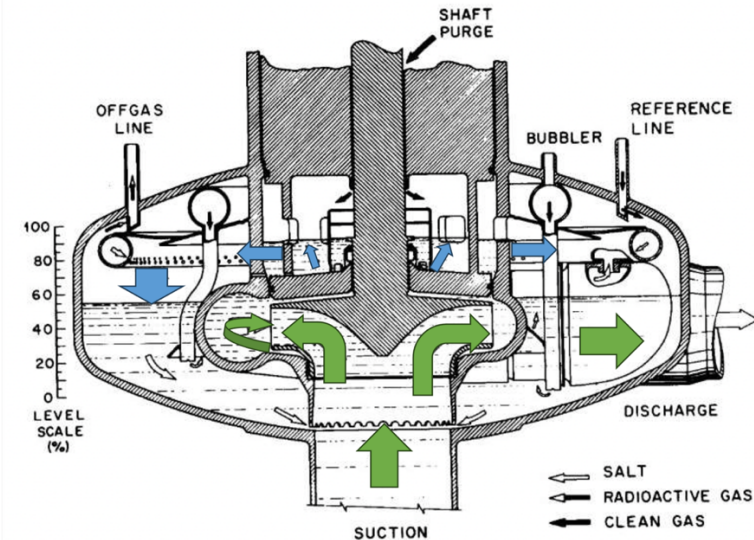


Figure 4-3 MSRE pump design (Engel et al., 1969): green arrows indicate the main salt flow pass, and the blue arrows indicate the flow pass into the gas spray ring (gas stripper).

In the other components such as pipes and heat exchangers, the removal/source terms included are decay and mass transfer between the salt and the bubble. The void fraction is controlled by the boundary condition instead of the bubble injecting speed. This should not affect the results significantly for steady state calculation.

4.2.2. Pronghorn-based MSRE Model

The MSRE model was developed using a 2-D axisymmetric domain in R-Z coordinates for both the spatial dynamics neutronics and thermal-hydraulics calculations. This model was based on a previous MSRE model developed by Idaho National Laboratory. This model has been previously published by the authors (Pfahl et al., 2025) but is documented here for completeness.

The spatial dynamics neutronics model in Griffin uses the multigroup diffusion approximation of the linearized Boltzmann transport equation. It accounts for the effect of advection and diffusion-driven drift of the DNPs and their decay in the outer loop by obtaining the DNP distributions from thermal-hydraulic calculations performed in Pronghorn using the porous media approximation.

The reactor core vessel is shown in the left panel of Figure 4-4 below, depicting the graphite stringers, fuel channels, lower and upper plenum, downcomer, and reactor core vessel. The right panel shows the developed 2-D R-Z model, including the graphite-moderated core, lower and upper plenum, riser, fuel salt pump, primary heat exchanger, outer loop pipe, and downcomer.

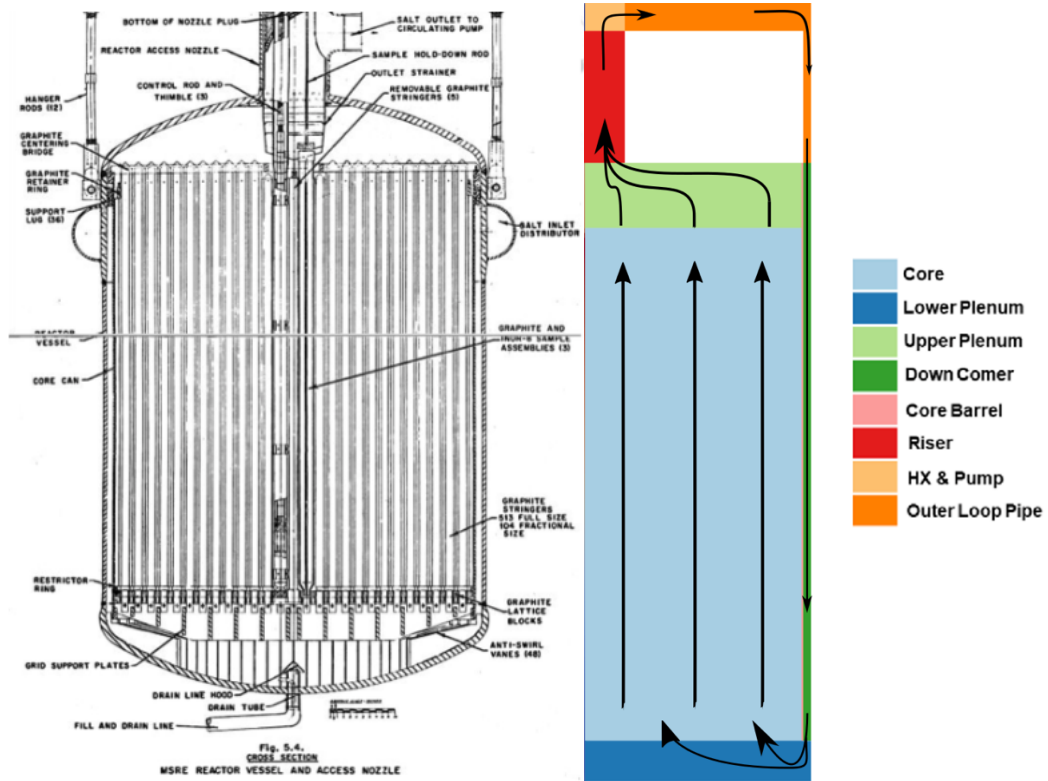


Figure 4-4. MSRE core (left) [Robertson, 1965] and 2-D R-Z model (right).

The total circulation time for the fuel in the entire system is 25.2 seconds, with the fuel taking 17 seconds to transition through the core, lower plenum, and upper plenum. The pump accelerates the fuel with a uniformly distributed momentum source, ensuring the volumes of the in-core and out-of-core regions reflect the reported volumes and circulation times.

4.3. Preliminary Verification and Validation

In this section, we present the results of our code-to-code verification between Griffin and Squirrel for transient analysis and validate these results against the experimental data from the MSRE. The analysis includes steady-state results, pump start-up and coast-down transients, and natural circulation tests. These results demonstrate the accuracy and reliability of the coupled multiphysics simulations using Griffin, Squirrel, and Pronghorn.

4.3.1. Depletion Modeling and Validation

This section analyzes the depletion results for MSRE obtained in Griffin using macroscopic and microscopic cross sections.

4.3.1.1. Macroscopic Depletion in Griffin for MSRE

The 3D MSRE model previously utilized for macroscopic depletion modeling, depicted in Figure 4-5, was also adopted for the microscopic depletion modeling approach, allowing a direct comparison between the two methodologies if required. Detailed information regarding this MSRE model can be found in Hartanto et al., 2023.

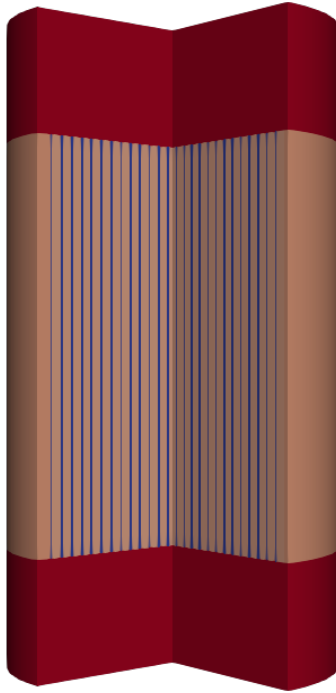


Figure 4-5. Simplified MSRE model used for depletion calculations.

Multigroup macroscopic cross sections were generated using an 8-group energy structure recommended by Kópházi et al., 2023 specifically for MSRE analyses. As an initial step in this study, multigroup macroscopic cross sections were generated only at fresh fuel salt conditions using two Monte Carlo neutron transport codes, Shift and OpenMC. Using a single, uniform cross-section set across all fuel salt regions resulted in an overestimation of the effective multiplication factor (k_{eff}) by approximately 1,276 pcm. To accurately capture varying neutron spectra within different reactor regions, separate multigroup cross section sets were produced for four distinct material regions: fuel salt within the core (located within graphite stringer), graphite moderator, fuel salt in the radial region, and fuel salt in the axial regions (top and bottom reflectors). Results from Griffin diffusion calculations employing these region-specific multigroup cross sections are summarized in Table 4-6. The comparison demonstrates excellent agreement between the Griffin diffusion results and CE Monte Carlo solutions, with relative differences in the k_{eff} below 160 pcm. Moreover, results obtained using microscopic cross sections in Griffin are consistent with those obtained from the macroscopic cross section sets.

Table 4-6. Comparison of effective multiplication factors using microscopic and macroscopic cross sections.

Code	Cross Section Type / Energy Structure	k_{eff}	Difference (pcm)
Shift	CE	1.01086 ± 0.00008	-
Shift/Griffin	Macroscopic 8-g	1.012334	147.4
	Microscopic 8-g	1.012334	147.4
OpenMC/Griffin	Macroscopic 8-g	1.012436	157.6
	Microscopic 8-g	1.012436	157.6

4.3.1.2. Microscopic Depletion in Griffin for MSRE

The next step involved preparing the microscopic cross-section sets necessary for Griffin microscopic depletion modeling. To generate these cross sections at discrete burnup points, a Monte Carlo depletion calculation was conducted to obtain isotopic compositions at each depletion interval. The depletion was conducted for one year with thermal power of 8 MW_{th}, discretized into 16 steps, without considering fractional removal of fission products and feed of makeup fuel salt. Monte Carlo calculations utilized 200,000 neutron histories per cycle for a total of 1200 cycles, with the first 200 cycles discarded as inactive. Serpent was selected for this depletion calculation due to its efficient, fully integrated depletion capability, making it computationally faster. OpenMC also supports depletion via its integrated Python-based module, however, its depletion calculations typically experience additional computational overhead associated with the data management processes, resulting in slower overall performance. Additionally, modeling a uniformly mixed, single-region depleted fuel salt is challenging in Shift, as it inherently partitions the depleted mixture into cell-wise depleted mixtures. Figure 4-6 compares k_{eff} evolution for two depletion modeling approaches in the Monte Carlo simulation: a single fuel salt depletion region representing uniformly mixed fuel salt, and a three-region approach that differentiates fuel salt in the core, in the radial region, and in the axial region. The three-region case exhibits a notably steeper reduction in k_{eff} due to a higher fissile consumption rate in the core region that has the highest neutron flux.

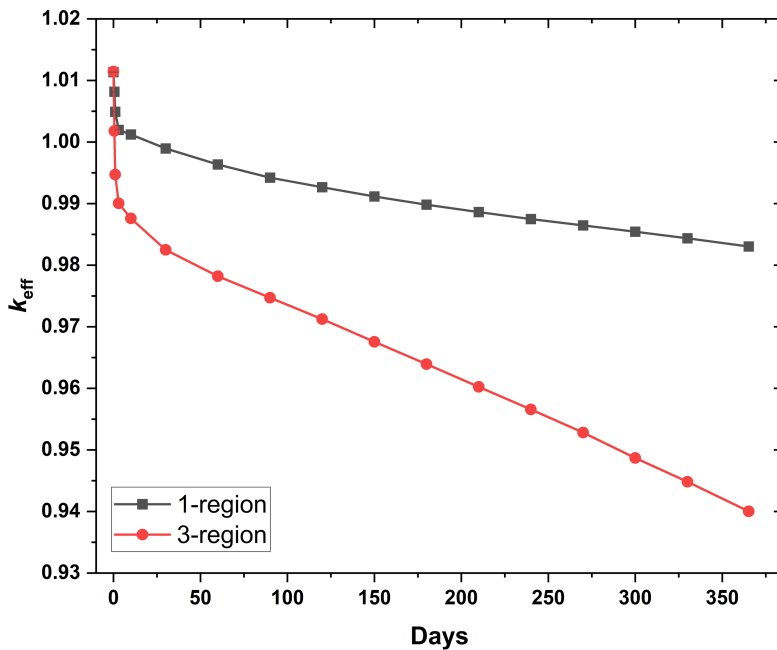


Figure 4-6. k_{eff} as a function of irradiation history for uniform single depletion and 3 depletion regions.

As illustrated in Figure 4-7, microscopic cross-section sets were produced at each depletion point using OpenMC using the irradiated fuel compositions generated from Serpent depletion calculations, maintaining consistent number of isotopes across all depletion steps. Each burnup point includes cross sections for 423 nuclides, consistent with the isotopes available in the ENDF/B-VII.1 nuclear data library, covering 21 reaction types as recommended in Griffin's User Manual. To consistently represent all nuclides at each depletion step, isotopes absent during early depletion stages were artificially introduced as trace isotopes with an extremely low atomic density of 1.0×10^{-20} atoms/barn-cm. However, introducing these trace isotopes minorly modifies the atomic density normalization of the fuel composition in the Monte Carlo simulations. Additionally, at the time of this study, Shift did not generate complete microscopic cross section sets for isotopes with nuclide densities below 1.0×10^{-15} atoms/barn-cm; specifically, microscopic scattering cross sections for these isotopes are zero. Due to this limitation,

the microscopic depletion modeling in Griffin was carried out using microscopic cross sections generated by OpenMC. However, after this work was performed, the Shift team has made the modifications necessary to allow for microscopic cross sections generation with trace isotopic content below 1.0×10^{-15} atoms/barn-cm. This modification is yet to be pushed into the production branch and will be tested in the future.

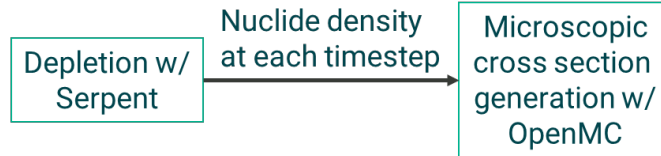


Figure 4-7. Flowchart illustrating the procedure for generating microscopic cross sections.

In the microscopic depletion approach with Griffin, the microscopic cross-section sets were generated separately for three distinct fuel salt regions (core, radial reflector region, and axial reflector region), consistent with the regions defined in the steady-state analysis. However, Griffin inherently performs depletion calculations independently for each region with a unique material number. To ensure Griffin treats the entire fuel salt as a single depletion region, the same material number was assigned to all three regions, and the cross-section sets were differentiated using unique `region_ID` grid. This workaround maintains correct use of spatial cross sections while performing depletion as a single region.

Sensitivity studies were performed to find the minimum number of burnup grids needed for accurate results. Four cases were set up to reflect the use of different cross-section libraries that were prepared, as listed in Table 4-7. Figure 4-8 compares the k_{eff} evolution obtained for each case. The lowest error bands are obtained with the single mid-cycle library (Case 2) and the full 16-point library (Case 4). Using only a simple BOC/EOC pair (Case 3) introduces noticeably larger deviations.

Table 4-7. Number of burnup points in the cross section grid used in Griffin.

Case	Burnup points used to generate microscopic XS
1	1 point at 0 day (fresh fuel)
2	1 point at 180 days (mid cycle)
3	2 points at 0 day and 365.25 days (fresh and end cycle)
4	16 points matching the 16 CE Monte Carlo depletion steps

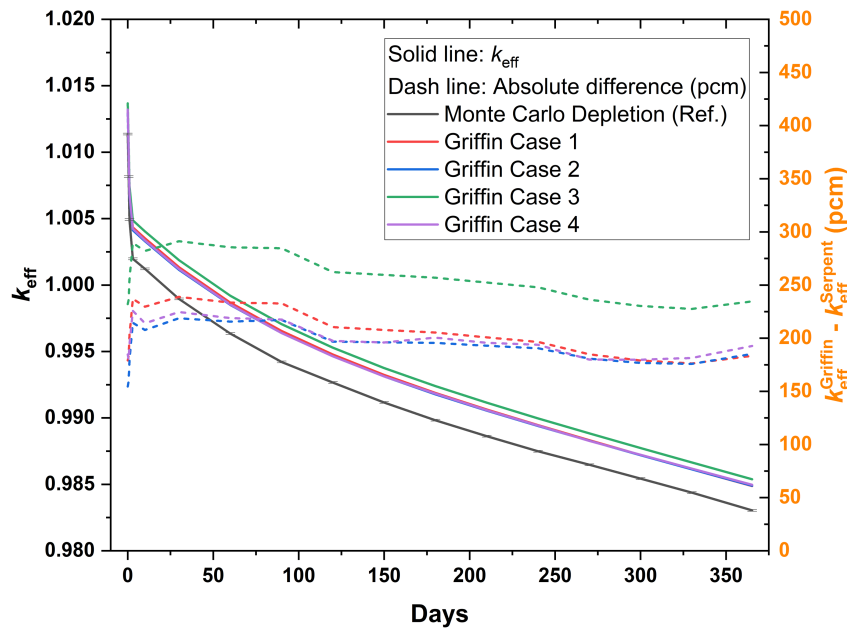


Figure 4-8. Comparison of k_{eff} as a function of irradiation history using different set of microscopic cross sections.

Figure 4-9 compares the isotopic number densities calculated by Griffin against those obtained from the reference Monte Carlo depletion performed by Serpent. In general, the Griffin results exhibit good consistency across cases. However, for isotopes with atom densities greater than 1.0×10^{-8} atoms/barn-cm at 365.25 days, Griffin predicts slightly lower values than Serpent, with relative differences ranging from approximately -4% to -5%. Notably, larger discrepancies were observed for Pu-239 and Pu-240, with relative differences of approximately -15% and -14%, respectively, compared to the Monte Carlo reference. These significant deviations suggest that the current 8-group energy structure might be inadequate to capture the resonance energy regions that affect the buildup of these plutonium isotopes. Future studies using a finer energy-group structure are recommended to better represent resonance absorption phenomena and potentially reduce these differences.

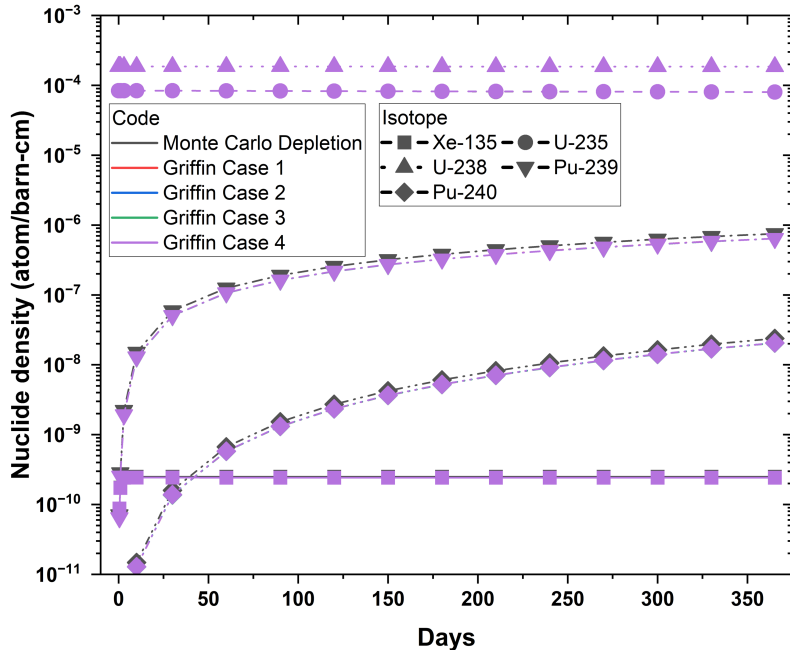


Figure 4-9. Comparison of selected isotopes as a function of irradiation history.

4.3.2. Radiochemical Transport Analysis Using Multi-Region Depletion

In FY25, work was performed to develop a benchmark problem for the Griffin fuel depletion solver, building on similar FY24 work that demonstrated a method to estimating radionuclide inventories in the Molten Salt Reactor Experiment (MSRE) off-gas system (OGS) from radiochemically measured gas samples (Shahbazi et al., 2024). The present work introduces a novel application of radiochronometry to estimate nuclide inventories in the MSRE OGS based on a limited set of on-line gamma spectroscopic data taken during ^{233}U power operation of the reactor. By analyzing isotopic, isobaric, and isomeric activity ratios measured in MSRE off-gas streams, key depletion model parameters related to species transport within the reactor system could be inferred. The findings demonstrate the potential of leveraging a small set of gamma spectroscopy measurements to accurately estimate nuclide inventories throughout the OGS. The approach can be useful in reactor design activities and support analyses relevant to operations, safety, security, and safeguards.

In order to perform the radiochemical transport analysis of the OGS experimental data, it was necessary to utilize a model that tracks nuclides across multiple successive OGS regions transferred from a fuel region representing depletion in the primary loop. This is due to the fact that the experimental data consists of the activity of short-lived fission products after a hold-up time representing multiple regions of the reactor system. This includes the transport from the core to the pump bowl, evolution to the cover gas of the pump bowl, and the flow through the various stages of the OGS system itself. The multi-region OGS fuel depletion compartment model simulated in this study can be seen in Figure # below.

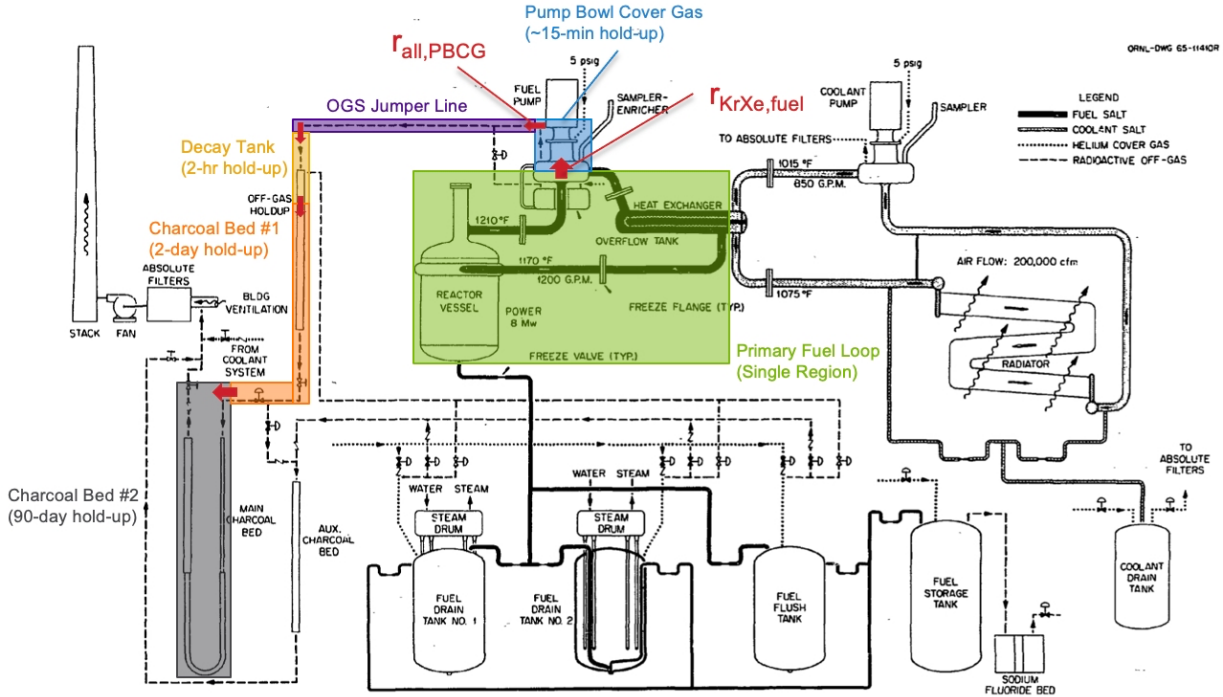


Figure 4-10. Discretization of the MSRE fuel and OGS compartments modeled in the present study, overlaid on a representative design flowsheet of the reactor system (reproduced from Houtzeel et al., 1972)

During FY25, key functionalities needed to perform this study were not yet available in the Griffin fuel depletion solver, therefore the initial benchmark problem was demonstrated with the OpenMC fuel depletion solver and was recently published elsewhere (Shahbazi et al., 2024). As a result of the study, the Griffin fuel depletion solver was assessed, and the missing capabilities were proposed to the Griffin development team. Code development is planned for FY26 to implement the capabilities necessary to perform such a multi-region OGS inventory tracking study. Once ready, these new capabilities will be demonstrated with this benchmark problem. Specifically, these capabilities are related to the tracking of nuclides at each depletion timestep not only in the main “fuel region” but also within multiple user-defined “ex-fuel regions” that are connected, e.g., a region of an OGS. The currently missing functionalities that will be developed in Griffin involve:

- The one-way transfer of nuclides/elements from one ex-fuel region to a different one
- The ability to track nuclides in more than three different ex-fuel regions

4.3.3. Analysis of Steady-State Pronghorn-Griffin Multiphysics Results

In this subsection, we provide the steady-state solutions of the MSRE model obtained from coupled Griffin and Pronghorn calculations. Also, results from a coupling within Squirrel, which is an open-source point kinetics application developed by the Technical University of Denmark (Pfahl et al., 2025), are introduced. These results are simply added as a measure of the accuracy that point kinetics solvers can have on MSRE transients. The results include isothermal temperature coefficients, effective delayed neutron fractions for stationary and circulating fuels, and steady-state distributions of power density, fuel salt temperature, and DNP concentrations.

The isothermal temperature coefficients for ^{235}U and ^{233}U fuel salts were calculated by globally varying the temperature in the reactor between 850 K and 1000 K. The temperature coefficients involve both density and Doppler feedback due to the temperature dependency of the fuel salt density. The

calculated values showed good agreement with the measured values obtained during MSRE operations. For ^{235}U fuel, the calculated temperature coefficient was approximately -12.7 pcm/K , closely matching the measured value of $-13.140 \pm 0.372 \text{ pcm/K}$. For ^{233}U fuel, the calculated value was -17.7 pcm/K , compared to the measured value of $-15.300 \pm 0.433 \text{ pcm/K}$. This agreement indicates that the model accurately captures the thermal feedback mechanisms in the reactor.

The steady-state distributions of power density, fuel salt temperature, and salt velocity, shown in Figure 4-11, Figure 4-12, and Figure 4-13, respectively, obtained from coupled Griffin-Pronghorn calculations revealed key insights into the reactor's behavior. The power density was highest at the center of the active core region, with lower values near the outer core. The fuel salt temperature distribution was skewed toward the top of the core, with a maximum temperature of approximately 950 K near the core's center. The fuel salt flowed upward through the core, with the highest flow rates in the riser region.

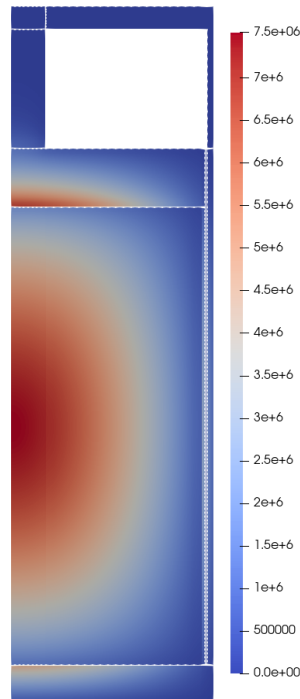


Figure 4-11. Steady-state power density distribution in W/m^3 .

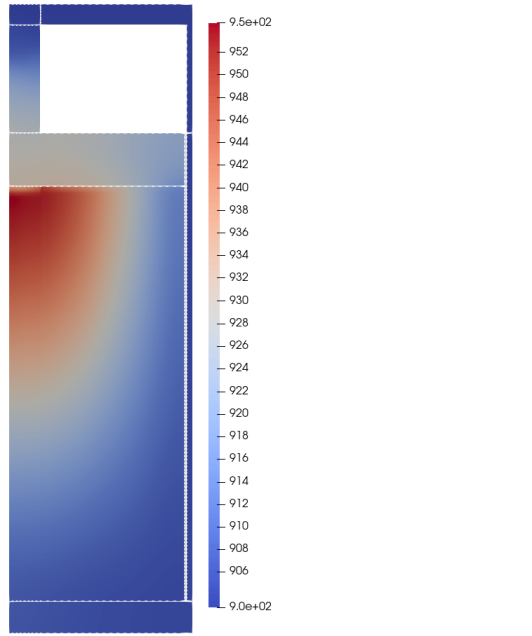


Figure 4-12. Steady-state fuel salt temperature distribution in Kelvin.

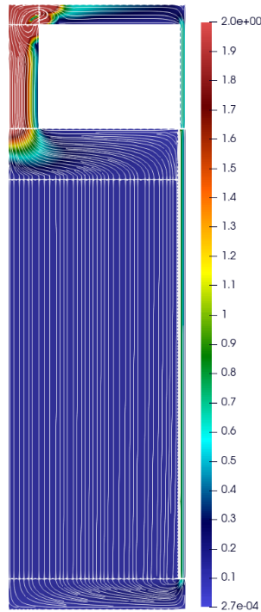


Figure 4-13. Steady-state salt velocity distribution with streamlines in m/s.

For the flowing-fuel case, the redistribution and decay of DNPs resulted in reactivity losses. The effective delayed neutron fraction for ^{235}U fuel salt was more than twice that of ^{233}U . Both Griffin and Squirrel showed good agreement with the measured reactivity losses, validating the accuracy of the models. The effective delayed neutron fraction for ^{235}U fuel was approximately 654 pcm, with a reactivity loss of 223 pcm. For ^{233}U fuel, the effective delayed neutron fraction was 298 pcm, with a reactivity loss of 110 pcm. The relative loss in reactivity was similar for both fuels, around 35%.

4.3.4. Pump Start-Up and Coast-Down

We validate the simulation results against experimental data for pump start-up and coast-down transients, which were performed with ^{235}U fuel salt at a low power level. These tests evaluated the reactivity changes due to changes in fuel salt flow rate, with control rods adjusting to maintain a constant low power level. The mass flow rate and pump force during start-up and coast-down are compared against experimental measurements for MSRE in Figure 4-14, showing a good agreement between the model and the experimental results.

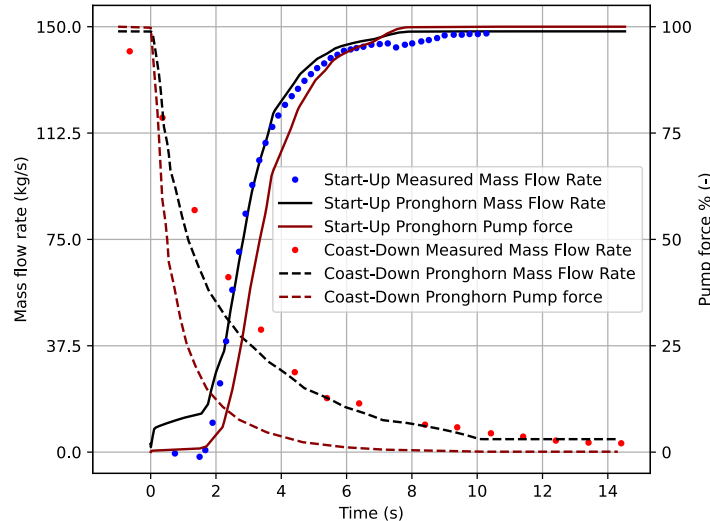


Figure 4-14. Steady-state salt velocity distribution with streamlines[Prince et al., 1968].

During the pump start-up test, the fuel salt mass flow rate increased, leading to increased reactivity losses due to the redistribution and decay of DNPs. The reactivity loss during the pump start-up transient, depicted in Figure 4-15, showed that both Griffin and Squirrel accurately captured the initial increase in reactivity loss and the final steady-state oscillations. The maximum difference between the codes was 3.5 pcm, indicating that the advection effects of DNPs were accurately modeled. The measured reactivity loss peaked at 284 pcm, while the simulations captured a peak loss of approximately 250 pcm. Despite this slight discrepancy, the overall trends and behavior were well-represented. This showcases the ability of the Griffin-Pronghorn model to predict pump start-up transients and that these transients could be modeled with point kinetics if one seeks computational efficiency.

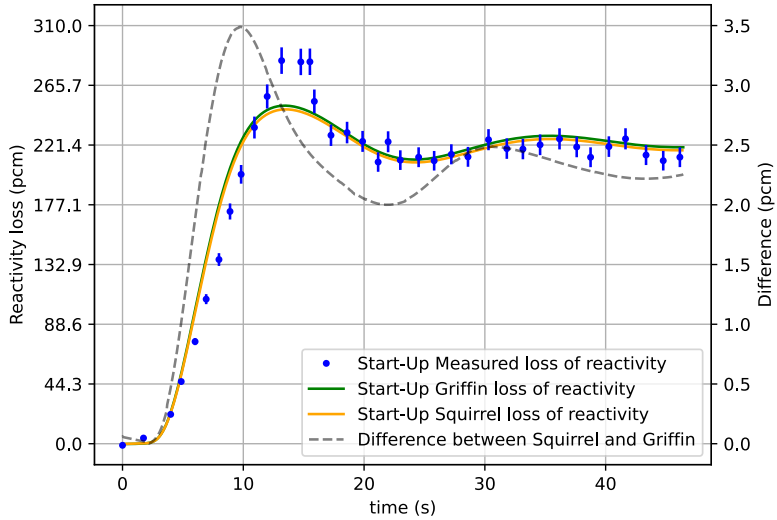


Figure 4-15. Reactivity loss during the pump start-up transient [Prince et al., 1968]. Note: Squirrel results are added as a metric of the performance that a point kinetic solver can have for this transient.

During the pump coast-down test, the reactivity loss decreased as the fuel salt flow rate reduced, leading to more DNPs decaying within the active core region. The results are depicted in Figure 4-16. The reactivity loss during the pump coast-down transient showed that both Griffin and Squirrel were in good agreement with the experimental values, with a maximum difference of 2.5 pcm. The results demonstrated that the codes accurately captured the reactivity changes due to fuel flow variations. The reactivity loss started at around 220 pcm and gradually decreased to zero as the flow rate decreased to zero. These results also show that point kinetics modeling would be enough for pump coast-down transients if computational efficiency is sought.

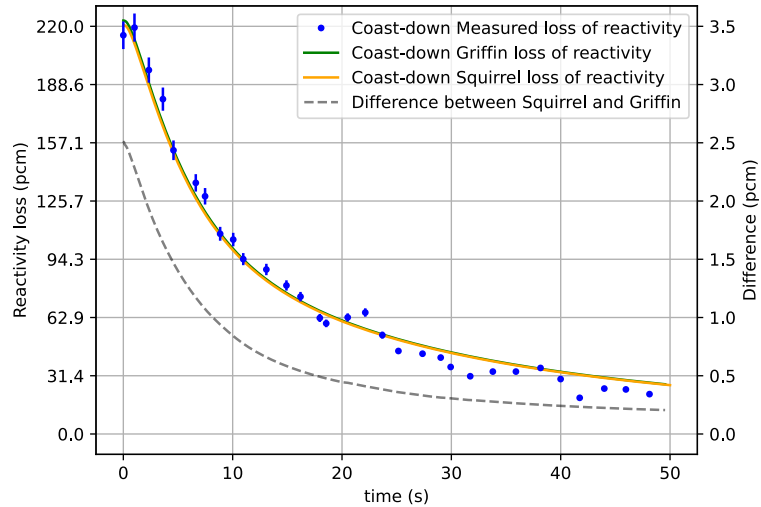


Figure 4-16. Reactivity loss during the pump coast-down transient [Prince et al., 1968]. Note: Squirrel results are added as a metric of the performance that a point kinetic solver can have for this transient.

4.3.5. Pump Start-Up with Added Void Transport

One notable issue from the previous models, as seen in Figure 4-15, is the inability of the model to predict the initial peak in the loss of reactivity during pump start-up. Predicting this peak is fundamental since this is the condition in which the stability of the MSRE is the furthest strained. Hence, in addition to modeling the coupled neutronics and single-phase thermal hydraulics mode, void formation during the pump startup process is incorporated into the model. This requires an additional void conservation equation and a drift-flux model for the slip velocity of the gases within the liquid salt.

The rationale behind this addition is that, unlike other nuclear reactor pumps, the MSRE pump suction line is permanently in contact with a gas interface due to its additional function of eliminating fission gases from the molten salt during normal operation. A sketch of the MSRE pump bowl showing the flow patterns is depicted in Figure 4-17. Consequently, gases from the cover gas region are incorporated into the liquid-fueled salt that circulates through the primary loop, playing an important role in reactivity prediction, especially for this validation exercise.

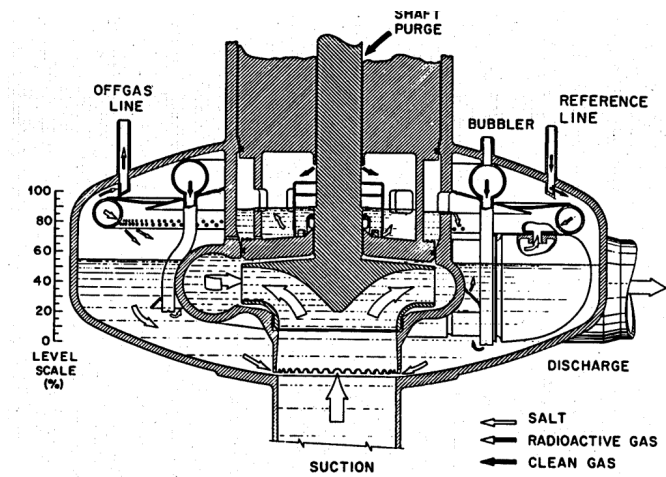


Figure 4-17. MSRE pump sketch with arrows indicating flow patterns

The results of different scenarios with void entrainment at the pump are shown in Figure 4-18. The green line represents the single-phase molten salt model with precursor advection. The model starts from the zero-power distribution of delayed neutron precursors in the core. As the pump is started, the DNPs (Delayed Neutron Precursors) are advected out of the core, resulting in a loss of reactivity from neutrons that previously decayed in the core region. After 25 seconds of recirculation time, the DNPs return to the core and stabilize at a new reactivity level, i.e., a new control bar configuration. Overall, the predictions correspond to the reactivity evolution in the transient. However, the reactivity peak at approximately 15 seconds is not captured with this model.

Considering the startup of the pump and the insertion of void due to the pump startup, void modeling is added to the multiphysics model. Void is assumed to be created during the startup until the pump reaches its maximum torque. Different quantities of void insertion from the pump into the loop have been explored in this parametric study, which falls within the expected void level ranges reported in the MSRE document, from 0.04% to 0.7% in the pipelines. The red line in Figure 4-18 shows the reactivity prediction for increasing levels of void. Compared to the green line predictions without void formation during the startup, the results indicate extra negative reactivity, resulting in a reactivity peak at 15 seconds of the transient, coinciding with the recirculation time from the pump to the core region entry. The predictions of the model, assuming void formation during the pump startup, enhance the prediction of the

negative reactivity inserted in the transient, while the continued DNP advection outside and inside of the core maintains the same level as the experimental calculations.

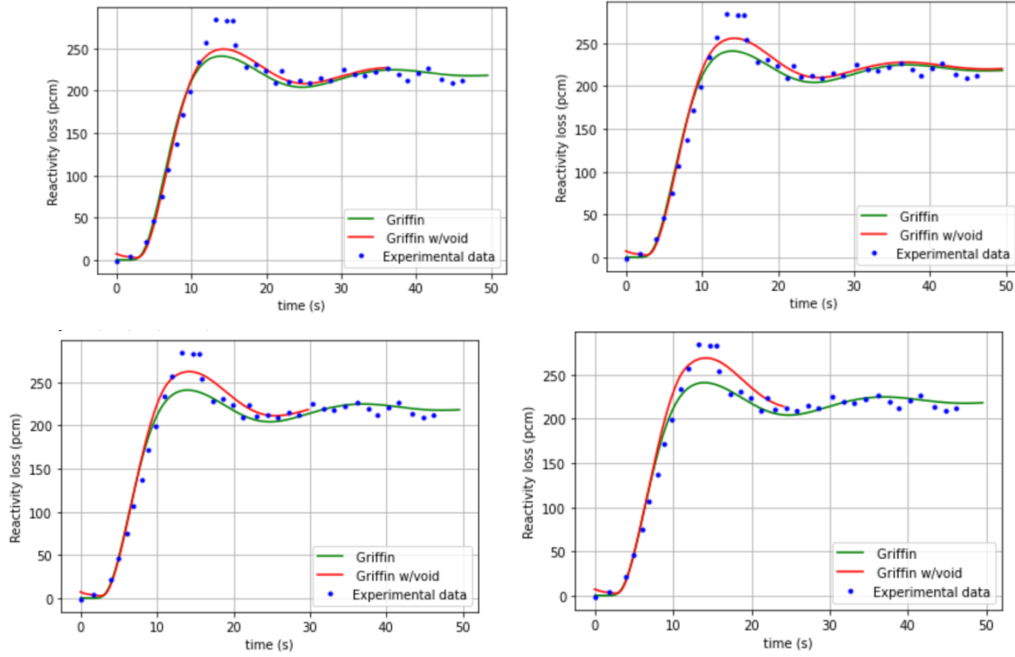


Figure 4-18. Reactivity loss as a function of time during the MSRE pump startup. Experimental measurements [Prince et al., 1968] are plotted in black, Griffin and Pronghorn predictions without void are plotted in green and Griffin and Pronghorn predictions with void formation are plotted in red. Panels compare void injections to 0.04% (top-left), 0.1% (top-right), 0.25% (bottom-left), and 0.7% (bottom-right), as the red curved, against the no-void-injection cases, as the green curve, and the experimental data, as blue dots.

4.3.6. Natural Circulation Test

The natural circulation test examined the reactor's behavior with ^{233}U fuel salt and the primary pump turned off. The fuel salt circulated due to buoyancy forces, with the reactor's power and temperature evolving over several hours.

The inlet and outlet fuel temperatures, along with the mass flow rate, were tracked throughout the natural circulation test and are shown in Figure 4-19. The temperature evolution showed that as the inlet temperature was gradually reduced, the reactor power increased due to the positive temperature feedback. Multiple power plateaus were reached, with the maximum power reaching 351 kW and the final power stabilizing at 324 kW. The mass flow and measured temperatures agree well between the models and the experiments.

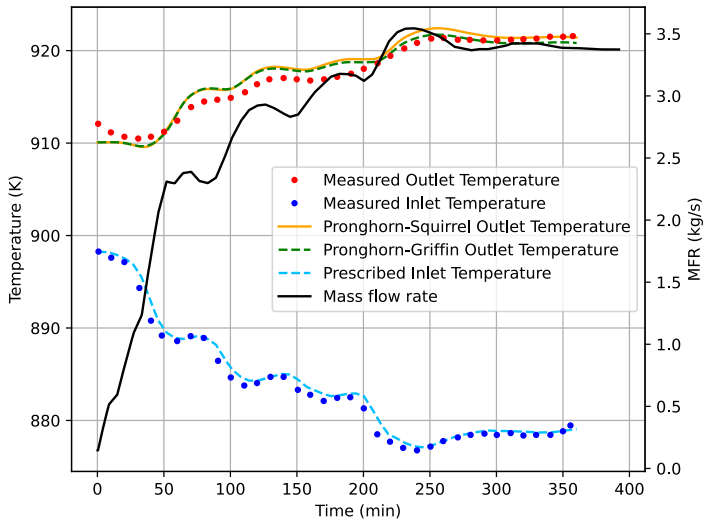


Figure 4-19. Mass flow rate and temperature evolution during the natural circulation test [Prince et al., 1968].

The reactor power evolution during the natural circulation test showed that both Griffin and Squirrel accurately predicted the power changes as shown in Figure 4-20. The maximum difference between the codes was 7.5 kW. The models captured the thermal feedback of the system, with the power increasing in response to the reduced inlet temperature and then stabilizing as the temperature reached a new steady state. This also shows that the power evolution during the natural circulation transient can be accurately predicted with point kinetics if computational efficiency is sought.

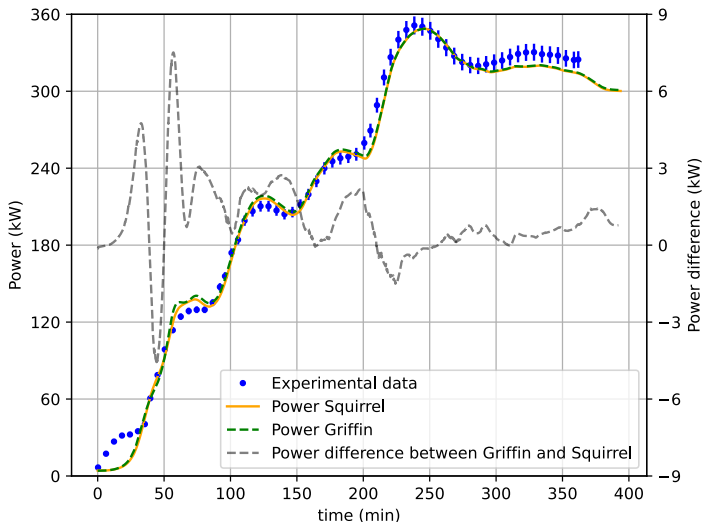


Figure 4-20. Reactor power evolution during the natural circulation test [Prince et al., 1968]. Note: Squirrel results are added as a metric of the performance that a point kinetic solver can have for this transient.

4.3.7. Testing Coupled Thermal-Hydraulics and Chemistry

The steady-state MSRE model previously developed in SAM and obtained from the Virtual Test Bed (VTB) by Hu et al. (2021) was modified to incorporate thermophysical property data from the Molten Salt Thermophysical Database - Thermophysical Properties (MSTDB-TP) (Termini et al., 2023). Thermophysical properties provided in MSTDB-TP, include melting temperature, boiling temperature, density, viscosity, thermal conductivity, and heat capacity, are formatted in a CSV file. To integrate these

properties into SAM simulations, the [SalineMoltenSaltFluidProperties] input type was utilized. For consistency and direct comparison, the original equations and thermophysical property data for the MSRE salt from the initial SAM model were transferred into the MSTDB-TP CSV format. Figure 4-21 compares the temperature profiles across the reactor core obtained from both the original SAM simulation and the updated MSTDB-TP implementation, showing excellent consistency between the two results.

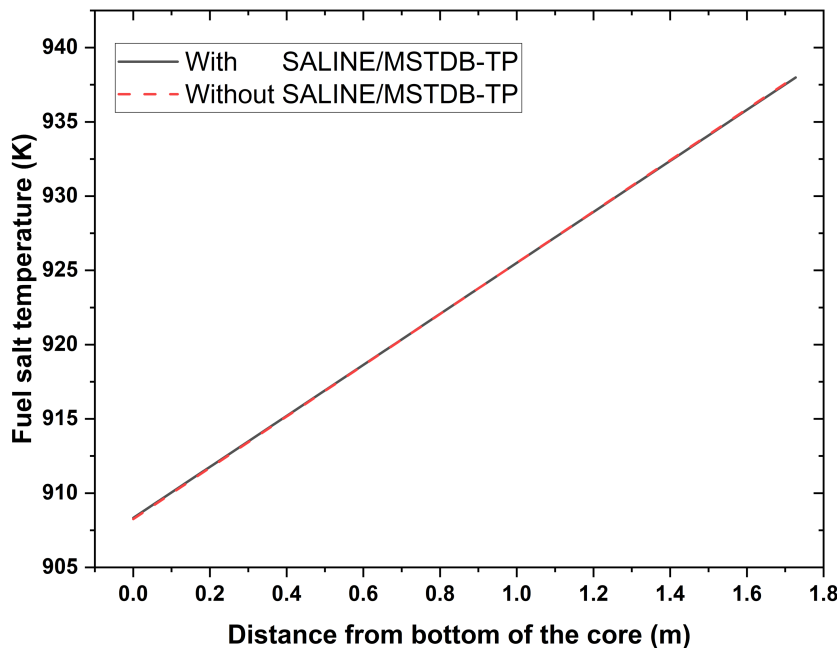


Figure 4-21. Comparison of fuel salt temperature in the core with and without using SALINE/MSTDB-TP with SAM

4.3.8. Evolution of the Redox Potential

The relative redox potential of the fuel salt in the MSRE was determined by measuring the percentage of UF_3 relative to the total $\text{UF}(x)$ in the fuel salt during approximately 9000 full power hours of the ^{235}U runs. The initial fuel salt had a UF_3 percentage of ~0.41%, which increased to a maximum of ~1.74% due to the addition of reducing metals like beryllium and uranium. These reducing metal additions, identified by sharp increases in measured UF_3 , are part of active chemistry control.

Without active chemistry control, the natural progression of the fuel salt thermochemistry leads to depletion-driven oxidation, where UF_3 is converted to UF_4 . This cumulative decrease in measured UF_3 is due to the consumption of $\text{UF}(x)$ and the production of noble fission products, which do not adequately replace the cationic charge of species in the fuel. The Griffin-depletion calculation, with active chemistry control, adequately captures the changing thermochemistry of the MSRE. Both the depletion-driven oxidation and the active chemistry control effects are replicated in the redox potential measurements of the MSRE ^{235}U runs with minimal normalization of the fluorine concentration within measurable uncertainty.

However, there is some bias in the Griffin-Thermochimica model during the second half of reactor operation, from ~4000 full power hours onward. This bias is likely due to errors in the zero-dimensional Griffin-depletion model, which appears to over-reduce the system by adding an incorrect amount of beryllium metal. The UF_4 to UF_3 ratio, shown in Figure 4-22, provides additional clarity on the relative agreement. The depletion-driven oxidation effect is seen more clearly with parabolic increases in the UF_4 to UF_3 ratio, while active chemistry control through beryllium metal additions results in sharp decreases of the ratio.

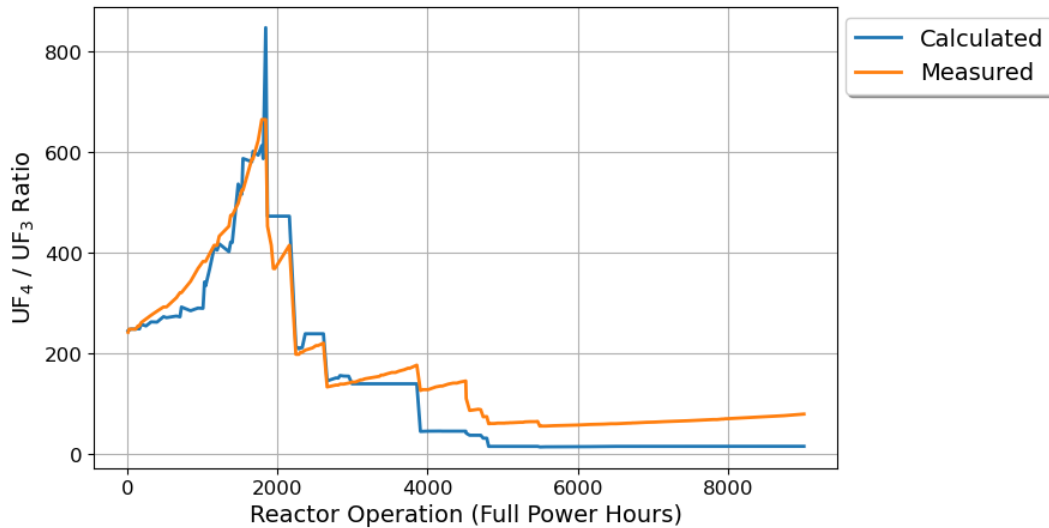


Figure 4-22. UF_4 to UF_3 ratio in the MSRE during ^{235}U runs for fuel-salt depletion and reducing material additions, measurements from Thoma (1971) report.

Including measured corrosion products, results in a calculated UF_4 to UF_3 ratio that is too reduced and performs worse than without considering corrosion products. This is likely because the current Thermochimica model treats chromium, nickel, and iron corrosion products as pure substances rather than part of an alloy mixture. Future work will incorporate a simple alloy model to better capture the thermochemical equilibrium between the fuel salt and the structural material alloy, accurately determining the amounts of corrosion products in the fuel salt.

4.3.9. Xe Transport

The SAM-Griffin model developed is applied to evaluate the Xenon poisoning effect of MSRE at the steady state. The reason to choose MSRE is due to existing experimental measurement of the Xenon poisoning effect at the steady state for different void fractions in the fuel salt. The main experiment measurements to be compared with are obtained from Reference (Engel and Steffy 1971) and are illustrated in Figure 4-23. This figure plots the reactivity change due to Xe-135 presence in MSRE for different void fractions in the core.

It should be pointed out that the Argon cover gas was used in this case. Another set of data is available for Helium cover gas. The main difference between the two cases is the solubility of the two gases in the fuel salt (Argon is much less soluble than Helium in the fuel salt). The SAM-Griffin model discussed in the previous section does not include the cover gas solubility effect, so it was decided to compare to the measurements with Argon cover gas.

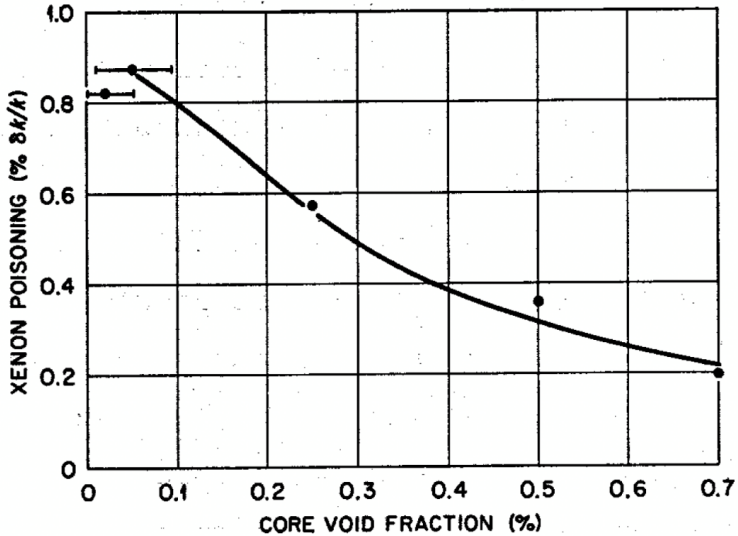


Figure 4-23 Experiment measurement of reactivity change due to Xenon for different void fractions (Engel and Steffy 1971).

4.3.9.1. Parametric Study

Two parametric studies were conducted to examine the effect of the mass transfer coefficients between the bubble and the fuel salt and the Henry's constant. The values of these parameters investigated are listed in Table 4-8. The current SAM model relies on a constant mass transfer coefficient and Henry's constant. Ongoing SAM development plans to add build-in correlations and to couple with the correlations developed in the Mole code (Lee et al. 2024), which allows the use of temperature-dependent coefficients.

Table 4-8. Mass transfer coefficient (MTC) and Henry's constant parametric study

MTC [m/s]	Henry's constant [mol/m ³ -Pa]	Notes
4.62E-3	1.85E-4	Both values are obtained from the example in Ref. (Mui et al. 2024)
7.00E-5	1.85E-4	The MTC is obtained from Ref. (Wu et al. 2024).
1.69E-4	1.85E-4	The MTC is obtained from Ref. (Kedl and Houtzeel 1967)
1.69E-4	2.90E-8	The Henry's constant is obtained from (Engel and Steffy 1971).

The results of the parametric studies are presented in Figure 4-24 and Figure 4-25 for the mass transfer coefficients and the Henry's constant, respectively. In all the cases, the Xe-135 concentration in the bubble is about $1.2 - 1.3 \times 10^5$ mol/m³ averaged over the entire core flow volumes. The Xe-135 concentration in the fuel salt is at least one order of magnitude smaller than that in the bubble, and it varies significantly with the mass transfer coefficients and the Henry's constant. All the cases have a core-averaged void fraction of 0.25%. Most of Xenon is transferred to the bubble for different mass transfer coefficients and Henry's constant, and this is consistent with the low solubility of Xenon in the fuel salt.

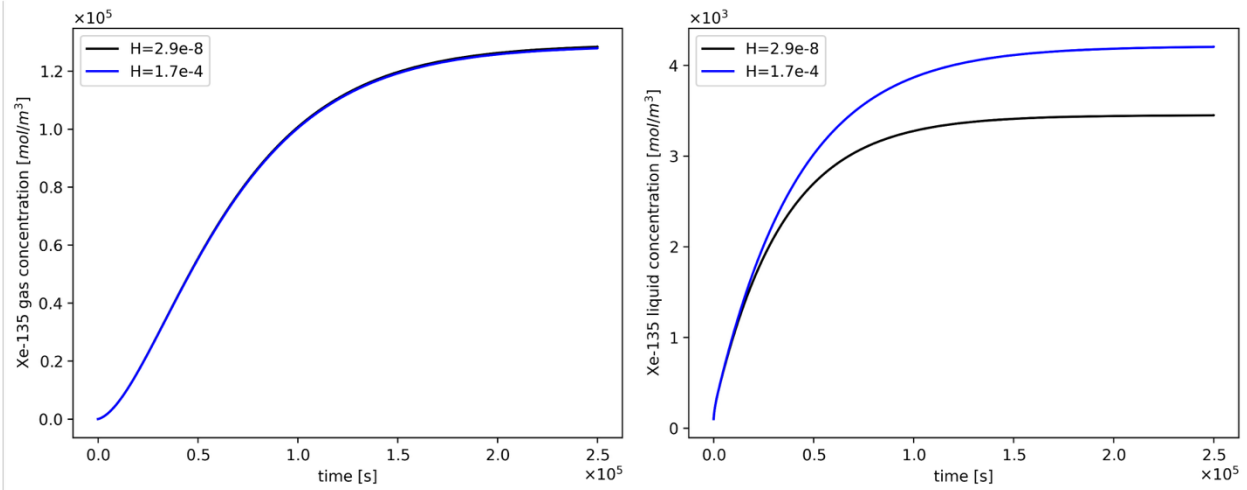


Figure 4-24 The Xe-135 concentration in the bubble (left) and in the salt (right) for different Henry's constant.

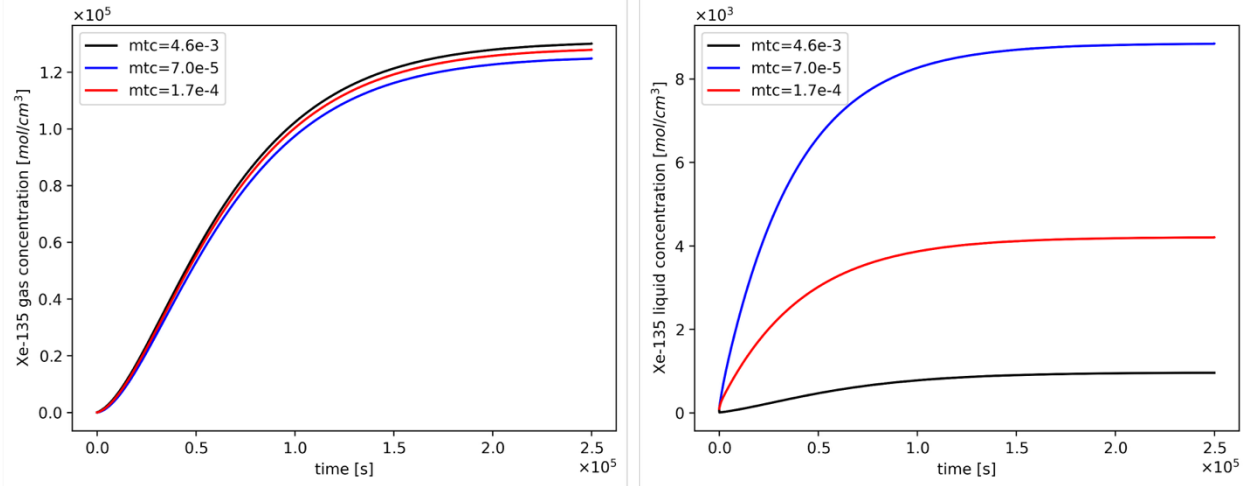


Figure 4-25 The Xe-135 concentration in the bubble (left) and in the salt (right) for different mass transfer coefficients.

A parametric study on the void fraction was conducted to investigate the effect of void fraction on the Xe-135 concentration. Four cases were examined for core-average void fractions of 0.05%, 0.25%, 0.50%, and 0.75% that covers the range of the experimental measurements. The results are presented in Figure 4-26. Noticeable difference is observed for the two cases with 0.05% and 0.25% void fraction. Above 0.25% void fraction, almost no change is observed in the Xe-135 concentration in the bubble. This means that bubbles with 0.25% void fraction have already picked up most of the Xenon gas generated in the core. This is also consistent with the Xe-135 concentration in the fuel salt, which shows the major drop in concentration when the bubble void fraction changes from 0.05% to 0.25%.

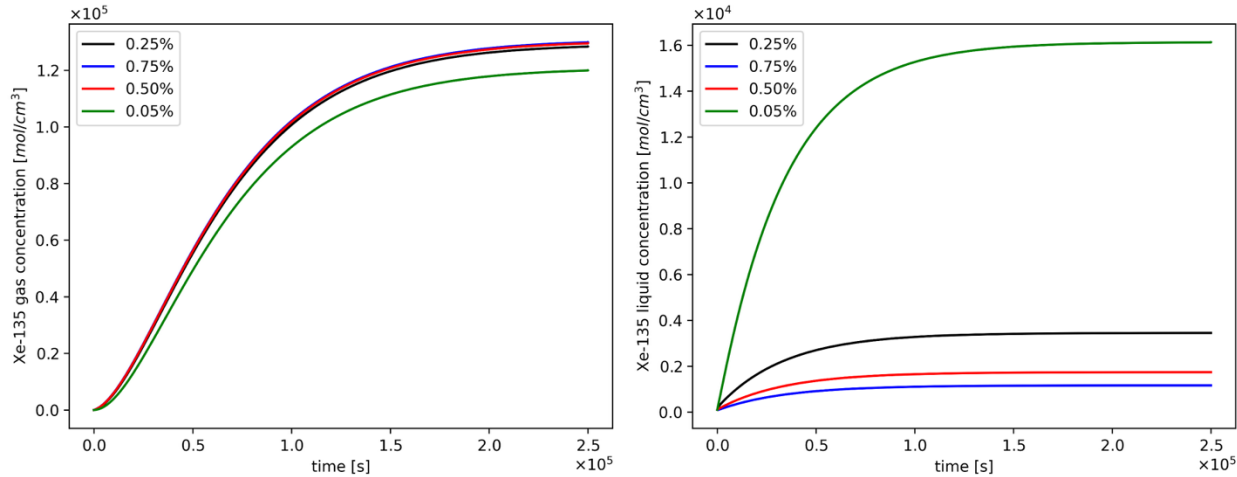


Figure 4-26 The Xe-135 concentration in the bubble (left) and in the salt (right) for different void fractions.

Given the large Xenon concentration in the bubble, the gas flow model is important in predicting the Xenon concentration in the MSRE primary loop. The gas model currently implemented in SAM is based on the drift flux model (Salko et al. 2021). It was acknowledged in Ref. (Salko et al. 2021) that some of the parameters used in the drift flux model were qualified for steam-water or air-water mixtures, so it would be important to validate the applicability of the model for molten salt. This validation effort on the gas model was also pursued and discussed further in the two-phase flow validation section.

4.3.9.2. Xenon Transfer Model to Graphite

In the MSRE core, Xenon can also transfer from the fuel salt to the graphite. Previous year's work relied on the Tritium diffusion model in the graphite. A simplified Xenon transfer model was implemented in Moose (Gaston et al. 2009) based on the method used in (Engel and Steffy 1971). For the simplified Moose model, the diffusion in the graphite is assumed to reach equilibrium instantaneously at each time step. This may be a problem for transient simulation but should have limited impact on the steady state calculation for the current validation effort. The distribution of the Xe-135 concentration can be solved analytically (by solving a 1D diffusion equation) based on the assumption as listed below.

$$c = \frac{c_0}{1 + e^{-2aL}} (e^{a(x-2L)} + e^{-ax}) \quad 4-3$$

Here, c_0 is the Xe-135 concentration at the interface between the salt and the graphite. a is the square root of the ratio of the removal rate (decay + absorption) and the diffusion coefficient. L is the width of the graphite. Based on this equation, the interfacial concentration can be related to the average concentration in the graphite by integrating over the width of the graphite.

The mass transfer of Xe-135 between the fuel salt and the graphite is modeled by adding additional Kernels in Moose, which relies on a mass transfer coefficient that relates the fluid bulk Xe-135 concentration to the interfacial concentration.

This simplified salt-to-graphite Xe-135 transport model was tested for the four-channel SAM model. The axial Xe-135 concentration distributions in different core channels are presented in Figure 4-27. The Xe-135 concentration in the fuel salt and in the graphite increases with the core axial position as Xe-135 is produced in the fuel salt directly from fission. However, the Xe-135 concentration in the bubble decreases with the core axial position because of the large absorption rate and the lack of direct fission production in the bubble. The magnitude of the change is dependent on the flux level in the core channel. The difference among different channels is relatively small. This means that a single-channel analysis may be sufficient for the Xe-135 transport calculation.

The Xe-135 concentration in the graphite is always smaller than that in the fuel salt due to the simplified salt-to-graphite transport model. The mass flux is always driven by the concentration difference between the salt bulk concentration and the interfacial concentration.

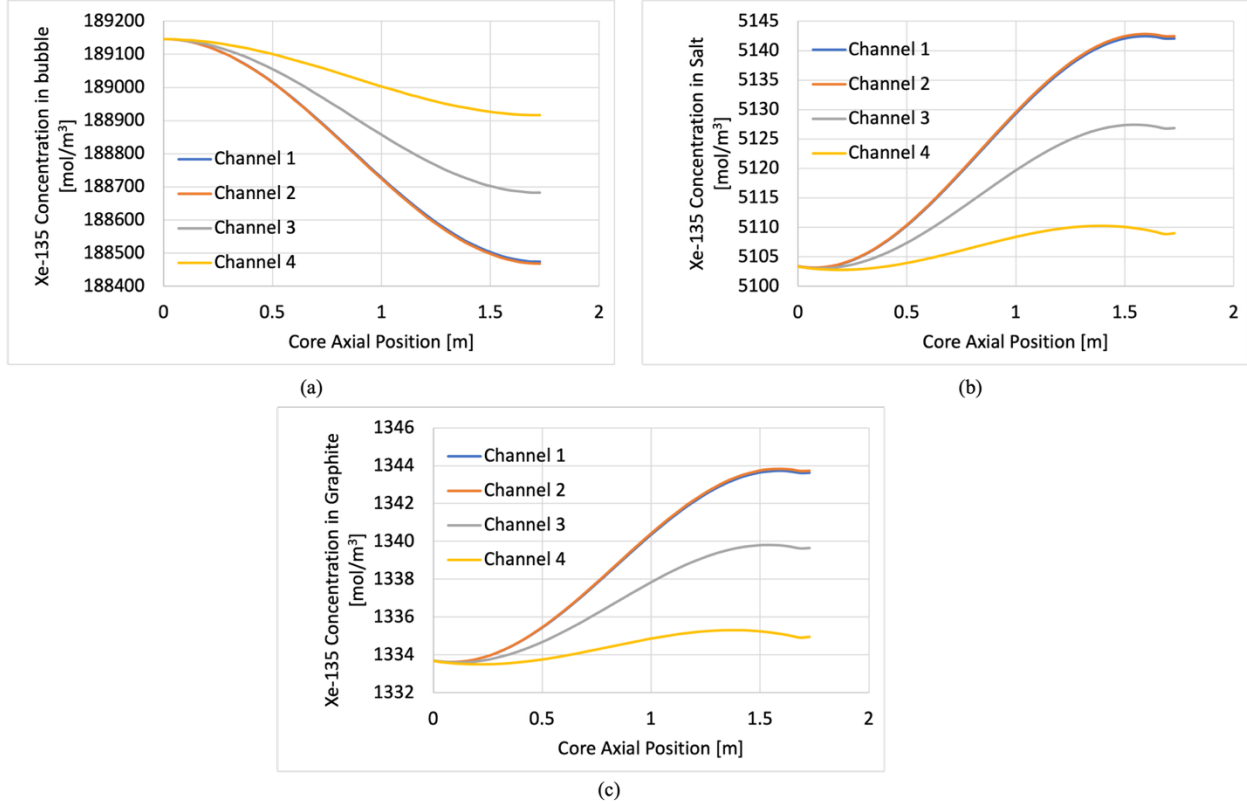


Figure 4-27 Axial Xe-135 concentration distribution in each core channel for the case with 0.25% void fraction.

The reactivity change due to Xenon poisoning is predicted for different void fraction using this simplified salt-to-graphite Xenon transport model. The results are shown in Figure 4-28 along with the experimental measurements. Good agreement between the predicted and the measured values can be achieved when using a bubble stripping efficiency around 5-7% for the case with 0.75% void fraction in the core. However, this efficiency is low compared to what was used in Ref. (Engel and Steffy 1971) (10%).

A higher stripping efficiency means more Xe-135 would be removed in the pump, which ultimately corresponds to a smaller reactivity change due to the smaller Xe-135 concentration in the bubble. The Xe-135 concentration in the graphite is too small to have any major impact on the final reactivity change. To resolve this issue, an improved SAM model on the Xenon transfer and diffusion in the graphite is employed. This SAM build-in model has been recently implemented in the recent SAM version. The detail of the methodology is described more in Ref. (Travis Mui and et. al 2025). This model relies on solving the diffusion equation in the graphite for each time step, which requires more computational time.

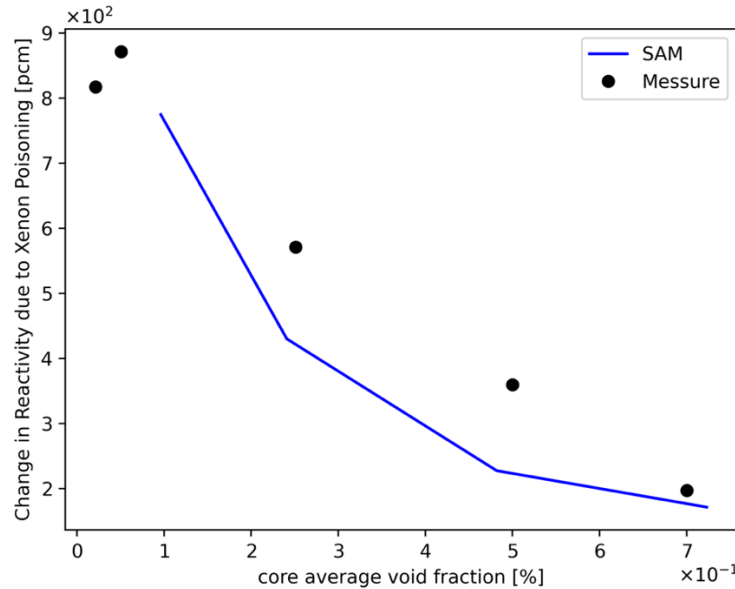


Figure 4-28 Xenon poisoning effect for different void fraction predicted using the simplified graphite diffusion model.

4.3.9.3. Comparison to experimental measurement

Two cases were investigated using the state-of-the-art SAM Xenon salt-to-graphite transport model. The first case uses a low bubble stripping efficiency (10% when void fraction is 0.75%) and a high salt-to-bubble Xe-135 MTC ($1.69\text{E-}4 \text{ m/s}$). The other case relies on a high bubble stripping efficiency (50% when void fraction is 0.75%) and a low salt-to-bubble Xe-135 MTC ($4.23\text{E-}5 \text{ m/s}$).

Comparing to the simplified diffusion model in graphite, the new model shows a higher level Xe-135 concentration in the graphite than that in the fuel salt. In the new SAM model, a thin gas layer is assumed to exist at the interface between the graphite and the salt. Thus, the interfacial Xe-135 concentration would depend on the solubility of Xe-135. This means it is possible to have a higher Xe-135 concentration in the graphite than that in the fuel salt. This is also observed in (Wu et al. 2024) for high void fraction in the core.

The average Xe-135 concentration in the core is listed in Table 4-9 for the case with low stripping efficiency and different void fractions. The Xe-135 concentration in the bubble is much greater than that in the fuel salt and in the graphite. As the void fraction increases, more Xe-135 would be removed from the primary loop of MSRE in the pump bowl, and the Xe-135 in all parts of the core would decrease accordingly. The predicted reactivity change due to Xenon poisoning is presented in Figure 4-29 along with the experimental results. Good agreement is achieved for this case with low stripping efficiency and high MTC. It should be noted that the stripping efficiency and MTC used in this case is consistent with that used in (Engel and Steffy 1971).

Table 4-9. Xe-135 concentration in the core for the case with low stripping efficiency and high salt-to-bubble MTC.

Void fraction [%]	Xe-135 Concentration [mol/m^3]		
	Bubble	Salt	Graphite
0.1	1.29E+05	1.80E+04	2.43E+04
0.25	7.41E+04	7.39E+03	9.95E+03
0.5	4.31E+04	3.72E+03	5.01E+03
0.75	3.04E+04	2.49E+03	3.35E+03

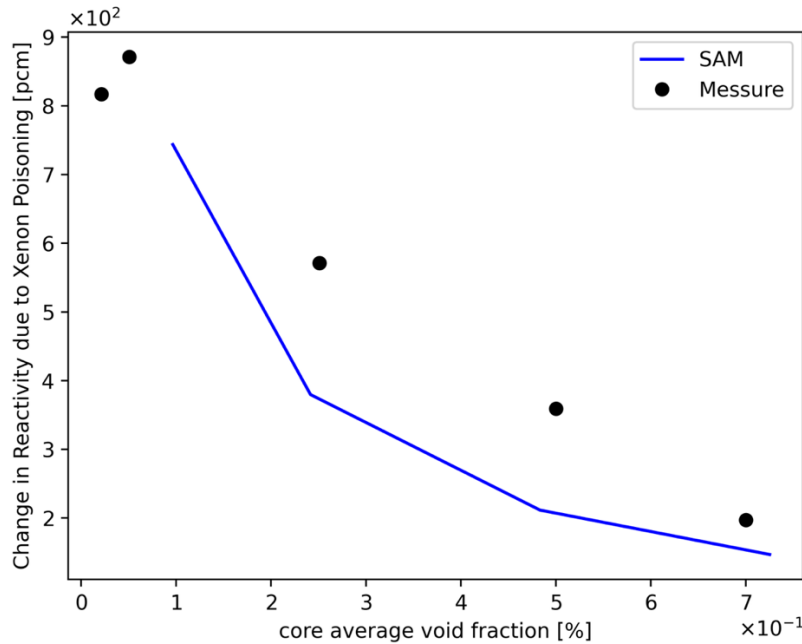


Figure 4-29 Xenon poisoning effect for different void fraction predicted using low stripping efficiency and high MTC to bubble.

The Xe-135 concentration in various parts of the core for the case with high stripping efficiency is listed in Table 4-10. Comparing to the low-stripping-efficiency case, the Xe-135 concentration in the graphite and in the fuel salt is about three times larger, while the Xe-135 concentration in the bubble is much lower. This is due to the lower salt-to-bubble MTC used, which means more Xe-135 stays in the fuel salt. The high stripping efficiency of 50% (void fraction at 0.75%) is likely closer to the reality as discussed in Ref. (Engel and Steffy 1971).

Figure 4-30 shows the Xenon-induced reactivity change as a function of the void fraction in the core and compares it with the experimental measurement. Again, good agreement is also reached for this case. For this case, the Xe-135 removal in the pump stripper can be directly observed in Figure 4-31. About 50% of the Xe-135 is removed in the stripper, which consists of about 5% of the total flow. The Xe-135 concentration in the bubble remains constant in the main flow path of the pump.

Table 4-10. Xe-135 concentration in the core for the case with high stripping efficiency and low salt-to-bubble MTC.

Void fraction [%]	Xe-135 Concentration [mol/m ³]		
	Bubble	Salt	Graphite
0.1	3.33E+04	5.80E+04	7.95E+04
0.25	1.62E+04	2.55E+04	3.50E+04
0.5	8.64E+03	1.32E+04	1.80E+04
0.75	5.87E+03	8.84E+03	1.21E+04

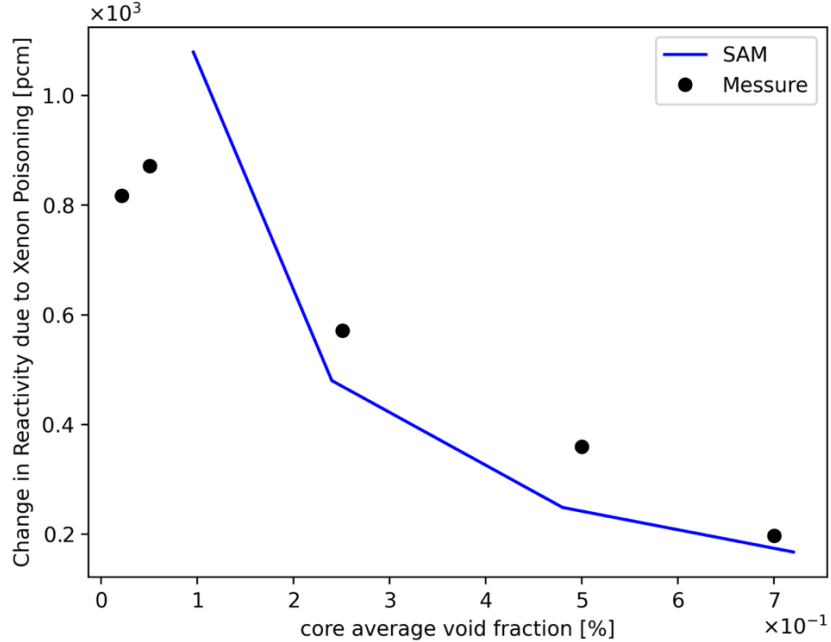


Figure 4-30 Xenon poisoning effect for different void fraction predicted using high stripping efficiency and low MTC to bubble.

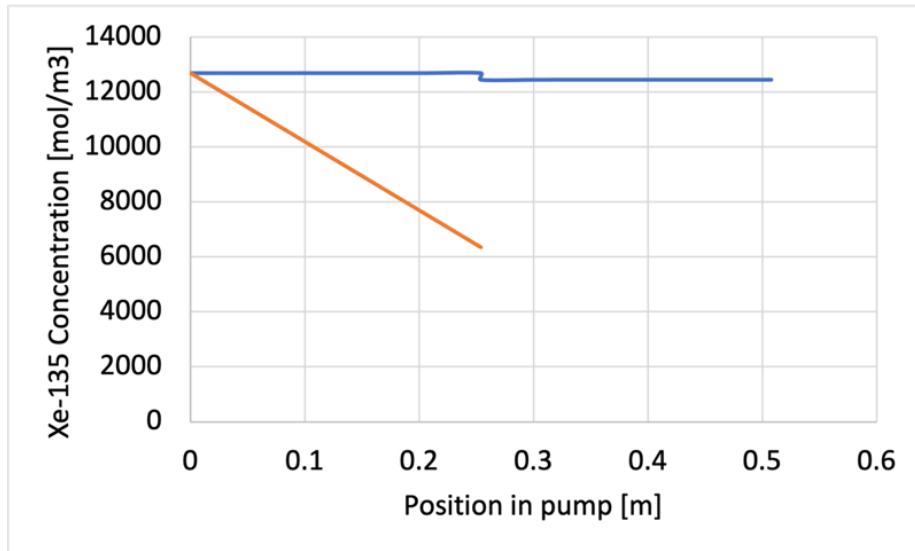


Figure 4-31 Xe-135 concentration variation in the pump main flow path and in the stripper.

At this point, it is difficult to further determine the applicability of the stripping efficiency and the proper MTC to be used. High-fidelity simulation and experiments are likely needed to better understand the Xenon transport phenomena in an MSR primary loop.

4.3.10. Noble Metal Transport

The Molten Salt Reactor Experiment (MSRE), conducted at Oak Ridge National Laboratory from 1965 to 1969, highlighted the critical role of noble metal fission products—such as molybdenum (Mo), ruthenium (Ru), niobium (Nb), antimony (Sb), and tellurium (Te)—in the operational challenges of liquid-fuel reactors. These elements, exhibiting low solubility in fluoride salts, coalesce into insoluble

particles that migrate via diffusion, sedimentation, or drift, leading to widespread plating on structural surfaces. This phenomenon not only causes physical fouling and reduced flow efficiency but also generates localized decay heat and gamma radiation hotspots, potentially compromising material integrity and safety during transients or shutdowns (Tanaka, 2017). As detailed in historical analyses, the behavior of these "noble metals" is of paramount importance to molten salt reactor design, influencing neutronics, fuel cycle optimization, and reprocessing strategies by affecting fission product residence times and inventory. Recent modeling efforts underscore the need for continued research, as uncontrolled deposition can exacerbate neutron poison loads and hinder passive safety features, informing modern designs for advanced MSRs (Frederix and Komen, 2023).

A particularly vulnerable component in this context is the MSRE's primary heat exchanger (PHE)—a shell-and-tube assembly critical for transferring heat from the fuel salt to the secondary coolant—where noble metal deposition emerges as a primary concern due to temperature gradients, turbulent flow, and high surface-to-volume ratios. Post-operation autopsies revealed significant plating, with Sb and Te exhibiting stronger adhesion than Mo or Nb on Hastelloy-N surfaces, leading to thermal inefficiencies and potential tube failures from decay heat concentrations exceeding 700°C limits (Tanaka, 2017). Multiphysics simulations and atomic force microscopy studies have quantified these adhesion forces and transport mechanisms, enabling predictive models for deposition rates and removal strategies via helium bubbling, which could reduce fouling by 5–15% in analogous designs (Frederix and Komen, 2023). Such investigations guide material selection (e.g., favoring low-adhesion alloys like SiC) and operational strategies, ensuring reliable heat rejection and mitigating risks in next-generation MSRs.

Building on these insights, the present study develops a detailed computational fluid dynamics (CFD) model of the MSRE PHE using the spectral element solver nekRS, establishing a foundational framework for subsequent multiphysics simulations with MOSCATO (Molten Salt Chemistry and Transport). Turbulent CFD has proven instrumental in retrospectively validating MSRE behaviors, providing deeper insights into conjugate heat transfer and structural dynamics; for example, recent OpenFOAM-based simulations of modified MSRE geometries have reconciled empirical data with predictive models, illuminating pathways to mitigate vibration and enhance efficiency in contemporary systems (Akner, 2021). As a precursor to integrated multiphysics analyses, these nekRS efforts lay the groundwork for MOSCATO, which fuses high-fidelity spectral element solving with modules for corrosion, electrochemistry, and multiphase transport to capture the holistic interplay of phenomena in MSRs (Yuan et al., 2024). Validated against MSRE-correlated benchmarks—such as alloy dissolution rates and tritium dynamics with errors under 15%—MOSCATO's GPU-accelerated architecture supports scalable analyses of complex interfaces, from bubble-induced mixing to particle advection. Extending this capability to noble metal fouling in the PHE, future integrations will model deposition hotspots and remediation tactics, such as inert gas sparging, to optimize material resilience and operational longevity in next-generation reactors.

NekRS (Fischer et al., 2022), developed at Argonne National Laboratory as part of the Nuclear Energy Advanced Modeling and Simulation (NEAMS) program, represents a cutting-edge, GPU-accelerated spectral element computational fluid dynamics (CFD) solver designed for high-fidelity simulations of incompressible and low-Mach-number flows on exascale computing platforms. Building on the legacy of the open-source Nek5000 code, nekRS integrates high-order spectral element discretization for exceptional accuracy and geometric flexibility, enabling efficient resolution of complex turbulent phenomena with minimal numerical diffusion. Its architecture leverages libParanumal's performance-optimized kernels for GPU execution, achieving unprecedented scalability—up to millions of elements on thousands of GPUs—while supporting applications in nuclear engineering, such as molten salt reactor thermal-hydraulics and heat exchanger flows. This makes nekRS an indispensable tool for predictive multiphysics modeling, bridging experimental data with advanced reactor designs through robust, massively parallel computations.

In partnership with Copenhagen Atomics, we have been provided with a comprehensive CAD model of the MSRE primary heat exchanger (PHE), which has been leveraged to develop an initial computational grid using the third-party meshing tool ANSYS Mesh. This complex geometry, featuring a U-tube shell-and-tube configuration, was discretized into an unstructured mesh comprising tetrahedral and wedge elements to accommodate its intricate design. Given that the spectral element CFD solver nekRS demands a pure hexahedral mesh for accurate simulations, an in-house conversion utility was employed to transform the ANSYS-generated mesh into a pure hex mesh suitable for nekRS computations (Yuan et al., 2020). The meshing process involved an iterative approach, carefully balancing computational efficiency and precision while preserving mesh quality, resulting in a finalized pure hex mesh with 56 million cells and a polynomial order of 3, yielding approximately 1.5 billion grid points. The resulting mesh is illustrated in Figure 4-32, providing a robust foundation for subsequent CFD analyses.

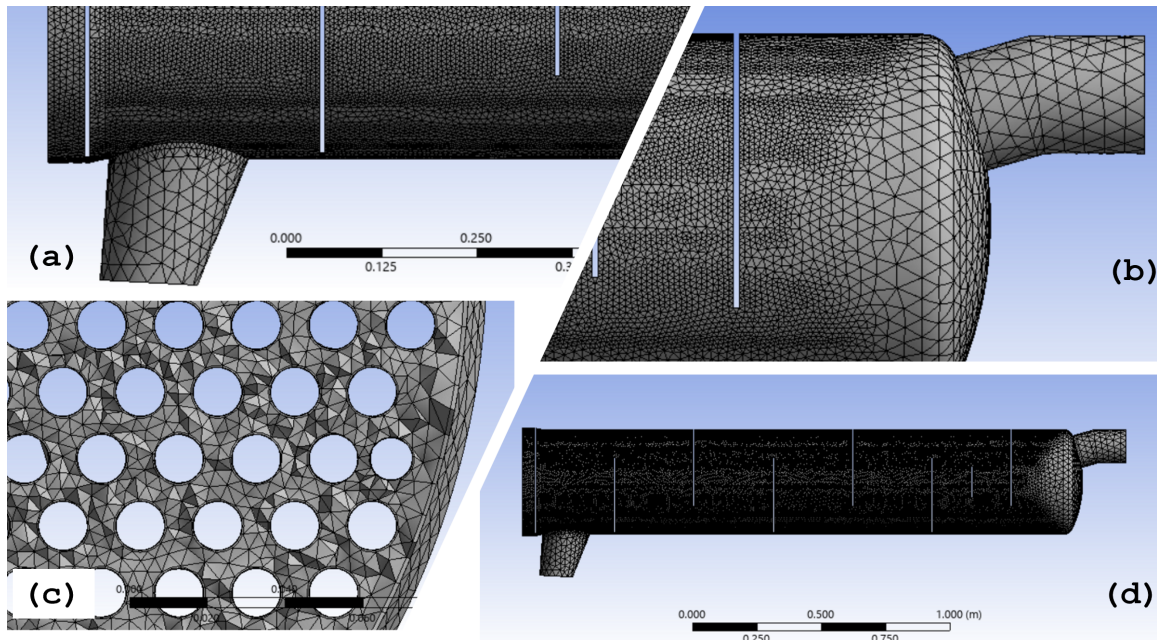


Figure 4-32. Computational mesh generated for the MSRE primary heat exchanger (PHE), showcasing local mesh perspectives: (a) outlet region of the PHE, (b) inlet region of the PHE, (c) cross-sectional view, and (d) an overall view of the PHE mesh.

Regarding the boundary conditions, a fixed inlet velocity is prescribed at the PHE inlet, while a natural pressure boundary condition is applied to the outlet face to facilitate realistic flow exit dynamics. All wall surfaces are treated as no-slip boundaries to reflect the viscous interaction with the solid structure, including the surfaces of the PHE shell, coolant tubes as well as the baffle plates installed. Initially, the flow is modeled under isothermal conditions to establish a baseline, but a more sophisticated CFD case is under development, incorporating temperature dynamics with representative thermal boundary conditions on the coolant tube surfaces within the PHE. With an anticipated flow rate of 1200 gallons per minute (gpm), the inlet velocity is calculated at approximately 5.93 m/s, resulting in a high Reynolds number of around 250,000 at the inlet, indicative of turbulent flow. However, within the tube bundle, the local Reynolds number drops significantly to approximately 7,000, based on a local hydraulic diameter of 0.026 cm and an expected fuel salt velocity of 0.84 m/s, reflecting a more subdued flow regime. Detailed flow properties and conditions essential for configuring these CFD simulations are compiled in Table 4-11. Given that the PHE is predominantly characterized by the tube bundle and features a relatively moderate Reynolds number across most of its domain, a large eddy simulation (LES) model has been selected to effectively capture the turbulent flow behavior within this complex geometry.

Table 4-11. Properties and flow conditions expected in the MSRE PHE.

Parameter	Value	Unit
Fuel Salt Composition	LiF-BeF ₂ -ThF ₄ -ZrF ₄ -UF ₄	
Density	2466	[kg/m ³]
Dynamic viscosity	0.0075	[Pa*s]
Kinematic viscosity	3.04136e-06	[m ² /s]
PHE inlet diameter	0.1275	[m]
PHE inlet fuel velocity	5.93	[m/s]
Hydraulic diameter of tube bundle	2.56e-2	[m]
Expected fuel velocity through tube bundle	0.845	[m/s]
Local Reynolds number at the PHE inlet	248,486.21	[\cdot]
Local Reynolds number within the tube bundle	7,119.04	[\cdot]

Leveraging access to leadership-class high-performance computing resources, such as Argonne National Laboratory's Aurora supercomputer, enabled the efficient execution of these large-scale nekRS simulations. The runs of interest utilized 500 Aurora nodes, each equipped with dual Intel Xeon CPU Max Series processors and six Intel Data Center GPU Max Series accelerators, facilitating rapid convergence and high temporal resolution. Simulations were conducted in a non-dimensional framework, with velocities normalized by the inlet velocity and lengths by the inlet hydraulic diameter; the molecular viscosity was gradually ramped down to align with the system's physical properties and target Reynolds numbers. A time step of approximately 2×10^{-5} non-dimensional units (equivalent to 4×10^{-7} seconds) was employed, and computations have advanced to 4.4 non-dimensional time units—placing the flow in a transitional developing regime, with ongoing extensions to fully developed conditions. Despite this, the dominant flow features have emerged distinctly, as illustrated in Figure 4-33 and Figure 4-34.

The instantaneous velocity magnitude field on the midplane ($x = 0$), depicted in Figure 4-33, reveals pronounced turbulence immediately upon fuel salt entry into the PHE, with peak normalized velocities exceeding 1.2 near the inlet and interacting intensely with the curved U-tube bends, generating shear layers and vortical structures that could promote enhanced mixing and potential erosion hotspots. Local velocity fluctuations are particularly evident around the U-tube headers and outlet regions, where gradients sharpen due to geometric constraints, suggesting regions of elevated shear stress relevant to fouling precursor transport. Deeper into the tube bundle, the flow is markedly influenced by the segmental baffle plates, enforcing a characteristic cross-flow zig-zag trajectory that periodically accelerates the salt through unobstructed baffle windows—manifesting as narrow high-velocity streaks (up to ~ 1.0 normalized)—while inducing recirculation zones upstream of baffle impingements, as hinted by the low-velocity blue hues in the figure. These recirculations, with magnitudes dipping below 0.2, may foster localized stagnation and particle settling, aligning with historical MSRE observations of uneven plating. Figure 4-34 complements this by illustrating the horizontal velocity (u_y), where adaptive arrow directions highlight lateral flow shifts around obstacles, with backflow eddies near baffle edges and

acceleration bands in gaps, potentially influencing the inertial transport of noble metal particles. These preliminary results align with MSRE observations of uneven plating, offering a foundation for future MOSCATO integrations to model multiphase interactions and fouling dynamics, with ongoing simulations expected to refine these insights as the flow approaches a fully developed state.

The figures provide valuable insights into the flow's spatial heterogeneity, which is critical for understanding noble metal behavior. In Figure 4-33, the high-velocity gradients at the U-tube bends and outlet suggest regions where shear-induced particle agglomeration or detachment might occur, a phenomenon worth exploring with particle tracking models. The recirculation zones near baffles, evident from the low-velocity blue regions, could act as deposition traps for smaller particles driven by Brownian motion, while the acceleration bands in window gaps may enhance inertial capture of larger particles, as hinted in the flow description. Figure 4-34's arrow patterns further suggest that the lateral flow shifts could create secondary flows or vortices not fully captured in magnitude alone, potentially affecting heat transfer uniformity and noble metal distribution. These observations underscore the need for extended simulation time and multiphysics coupling to validate deposition mechanisms, particularly in the PHE's high-gradient zones, aligning with the research goals outlined in the existing literature ([Frederix and Komen, 2023](#); [Tanaka, 2017](#)).

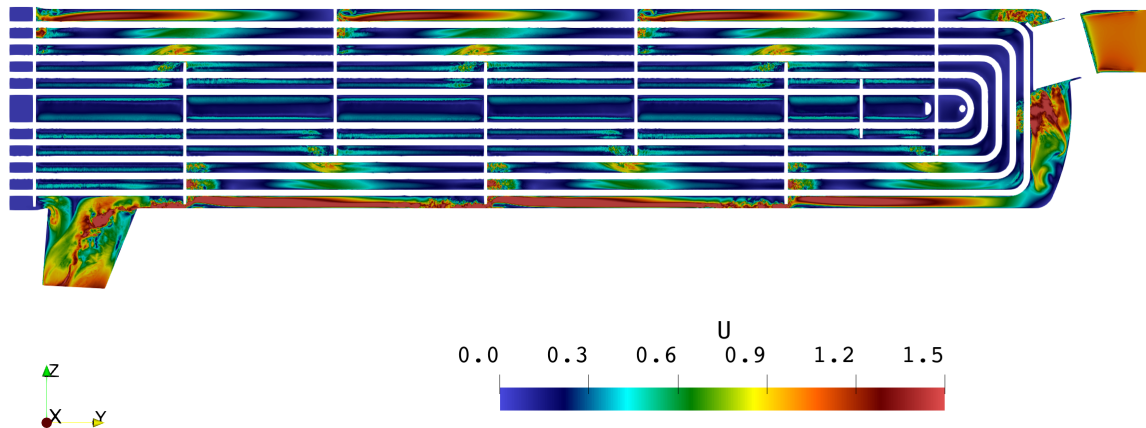


Figure 4-33. Instantaneous velocity field predicted by NekRS on the middle plane ($x = 0$) of the MSRE PHE.

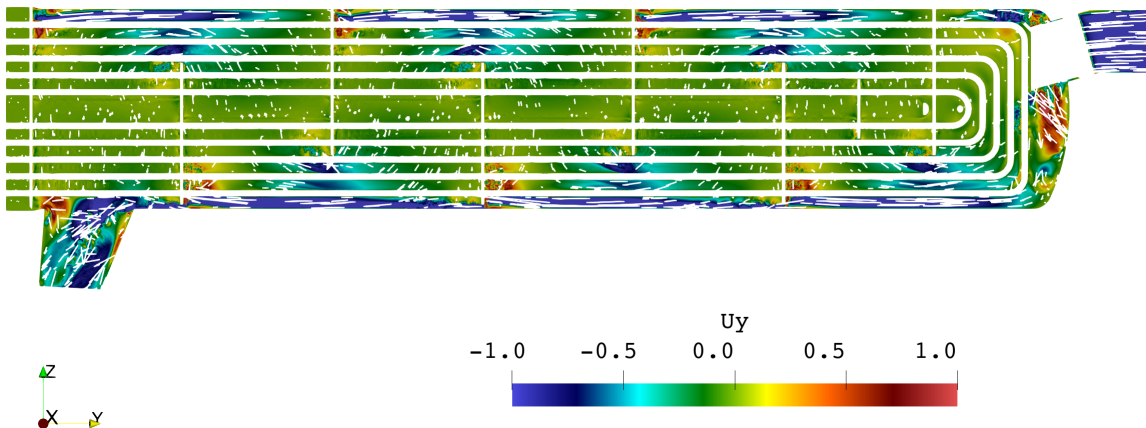


Figure 4-34. The horizontal middle plane velocity ($x = 0$) with arrows showing the local velocity directions inside the PHE.

5. Integral Effects Modeling of the Fast-Spectrum Lotus Molten Salt Reactor

5.1. Introduction

As an example of a fast-spectrum MSR, the Lotus Molten Salt Reactor (L-MSR) is modeled based on the open-source specifications of the Molten Chloride Reactor Experiment (MCRE). Work conducted in the first half of FY25 demonstrated the steady-state model of this reactor and the implementation of NEAMS tools to model several programmatic transients. These transients included full and partial losses of flow circulation, over-circulation of the fuel salt, overheating of the reactor piping due to electric tracing malfunction, overcooling of the reactor core, and various density changes in the fuel salt and the nuclear reflector. This fiscal year's work involved modeling more complex transients in the reactor core, further extending the testing and applicability of NEAMS tools.

5.2. Description of the L-MSR Model

For completeness, a brief overview of the L-MSR configuration is provided in this section. The proposed concept of the L-MSR is depicted in Figure 5-1. The reactor dimensions in this figure are provided in meters. The main components of the fuel loop include a core pool without internal elements, a pump, and the piping that connects the reactor to the pump. This model is based on the open-source specifications provided for TerraPower's MCRE. Surrounding the core cavity is a neutron reflector.

In this configuration, the liquid nuclear fuel enters the reactor cavity from the bottom piping, circulates through the cavity, and is then pumped back into the return piping. The reflector is modeled as a solid monolithic block, although in practice, it would likely be constructed from multiple blocks to minimize thermal stresses and facilitate fabrication. Only heat conduction is modeled in the reactor reflector, as work in FY24 demonstrated that the uncertainties associated with the mechanical deformation of the reflector are small compared to uncertainties in the cross sections, fuel salt thermophysical properties, etc. A mixing plate is included at the entrance of the reactor cavity to ensure uniform flow within the reactor.

The key design parameters of the reactor are summarized in Table 5-1. The fuel salt composition corresponds to the eutectic point of the $\text{UCl}_3\text{-NaCl}$ system. The thermophysical properties of the nuclear salt and the reflector are based on best-estimate values from open literature. Although most models in this study assume a reactor power of 25 kWth, TerraPower's MCRE is envisioned to operate within a range of 0.1 kWth to 150 kWth. This power range may be adjusted in future iterations of the concept, but for demonstrating the multiphysics model, a single characteristic power is sufficient. Similarly, a mass flow rate of 100 kg/s is assumed for the steady-state operation of the L-MSR, although the actual range for MCRE is postulated to be between 25 kg/s and 100 kg/s. Selecting one mass flow rate is adequate for studying the multiphysics response in low-power MSRs.

At this mass flow rate, the nominal pressure drop across the reactor loop is approximately 139 kPa. The fuel salt completes a full circulation through the loop, including the return piping and reactor core, in roughly 10 seconds. Due to the small core size, higher fuel enrichment is required to maintain a sufficiently large reactivity margin above criticality for sustained operation. In its current configuration, without the insertion of control rods, the reactor exhibits an excess reactivity of approximately 12,000 pcm.

Table 5-1. Key modeling parameter of the L-MSR [Walter, 2023].

Parameter	Value
Core Power [KWth]	25
Operation Temperature [K]	900
Mass Flow Rate [kg/s]	100
Fuel Salt Composition [mol %]	NaCl [33.3%] – UCl3 [66.7%]
Fuel Enrichment (235U) [wt %]	93.2
Fuel Salt Density [kg/m3]	$\rho = 4.213 \times 10^3 - 1.0686 T[K]$
Specific Heat Capacity [J/(kg.K)]	$C_p = 8.900439 \times 10^3 - 1.377936 \times 10^1 T[K]$ $+ 6.400369 \times 10^{-3} T[K]^2$ $- \frac{8.443758 \times 10^8}{T[K]^2}$
Thermal Conductivity [W/(m.K)]	$k = 5.6820 - 8.7832 \times 10^{-3} T[K]$ $+ 4.0967 \times 10^{-6} T[K]^2$ $- \frac{5.7642 \times 10^{-5}}{T[K]^2}$
Dynamic Viscosity [Pa.s]	$\mu = 1.505 \times 10^{-4} \exp\left(\frac{2.666 \times 10^4}{8.314 \times T[K]}\right)$

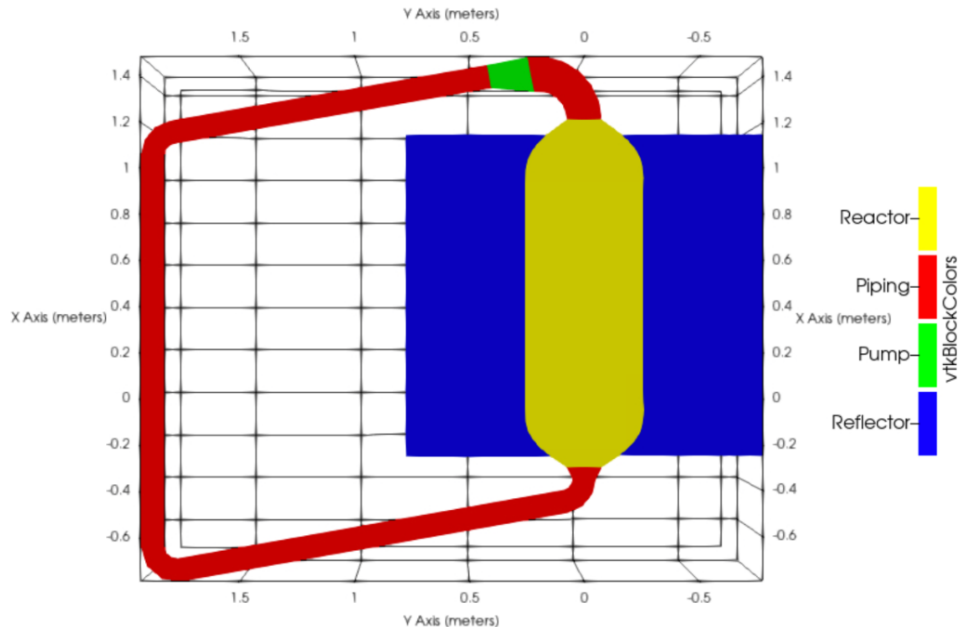


Figure 5-1. Simulation domain for the Lotus Molten Salt Reactor.

5.3. Multiphysics Demonstrations and Benchmarking

5.3.1. Benchmarking of the Hydraulics Flow Modeling for L-MSR

The simulations using MOOSE involve several steps, each addressing different aspects of the simulation to ultimately develop the final model. As the simulation progresses, the geometric complexity increases, expanding from a simple fluid domain to include a reflector and external domain considerations. This section will therefore be structured to reflect each step of the process, building up to the complete model.

The geometry modeled in MOOSE has been simplified to facilitate meshing within Cubit for analysis purposes. Figure 5-2 illustrates the fluid dynamics domain, where certain components have been modified or removed to streamline the simulation process. For instance, the mixing plate is represented but not resolved in detail, and the Venturi on the pipe, along with all instrumentation tubes, has been excluded. Additionally, surfaces have been strategically inserted at various locations to measure pressure drops and calibrate modeled features, such as the friction associated with the mixing plate.

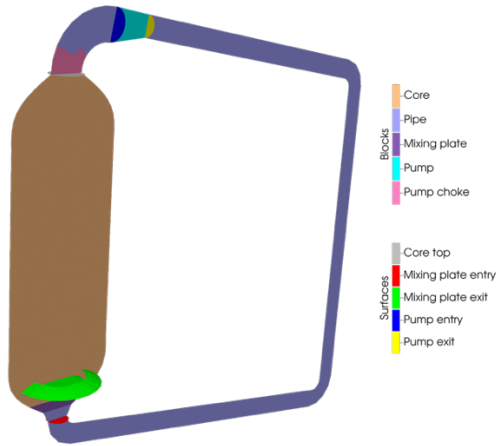


Figure 5-2. Fluid dynamics domain, with mesh blocks and measuring surfaces.

Table 5-2 lists the thermophysical properties of the fluid used in the simulation. To aid in convergence during the initial stages when fields are unknown and the simulation may be unstable, the fluid viscosity is artificially increased through a ramp-down function, as defined as follows:

$$\mu_{eff} = \mu(4e^{-t} + 1), \quad 5-1$$

For completeness, the effective viscosity is illustrated in Figure 5-3. This approach, known as numerical viscosity, gradually reduces the viscosity to its real value as the simulation progresses, ensuring that the final solution is unaffected by this initial adjustment.

Table 5-2. Thermophysical properties of the fuel salt

Property [Unit]	Value
Density [kg/m ³]	3279
Dynamic Viscosity [Pa.s]	0.005926
Thermal Conductivity [W/(m.K)]	0.38
Specific Heat Capacity [J/(kg.K)]	640

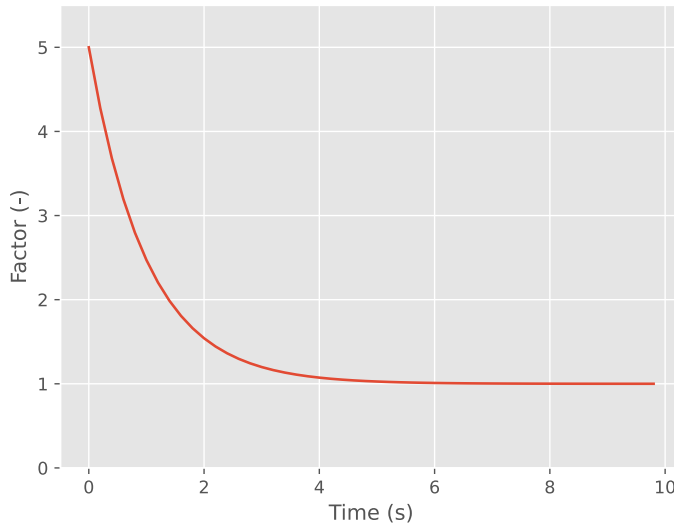


Figure 5-3. Viscosity Ramp-down Function

The domain is assumed to be entirely composed of fluid (i.e., no porosity is considered). A mixing length turbulence model is used, with the mixing length defined individually for each block. A friction coefficient is assigned to the mixing plate and pump choke blocks to represent their flow resistance. The mixing plate and pump choke blocks are assigned a zero mixing length, meaning all pressure drop is modeled through friction coefficients. A volumetric momentum source is added at the pump block. The pump choke block, where the fluid passage is restricted due to the impeller, and the pump block, where momentum is added to the fluid, are modeled as separate blocks. No-slip boundary conditions are applied to all outer surfaces. Pressure is pinned to zero at a cell located at the elbow between the reactor and pump blocks.

Separating the pump choke from the pump may initially appear counterintuitive. Originally, it was a modeling artifact introduced to account for the pump choke, which had previously been ignored. However, further analysis revealed that separating the location of the pressure drop from the location where momentum is added was the optimal arrangement. Combining these blocks would prevent proper calibration of the friction parameters for pump-related pressure drops, making it impossible to model natural circulation scenarios that require calibrated pressure drops without a momentum source.

To facilitate the calibration of mass flow and pressure drops, a proportional-integral (PI) control system is implemented. For example, mass flow is controlled by adjusting the momentum source (FF) at the pump block:

$$F_{controlled} = F_{baseline}(1 - f_{prop} - f_{integral}), \quad 5-2$$

Where f_{prop} and $f_{integral}$ are proportional and integral factors used to adjust the baseline pump force. The proportional factor is calculated as follows:

$$f_{prop} = C_{prop} I_{relative}, \quad 5-3$$

Here, C_{prop} is a constant that determines the impact of the relative imbalance ($I_{relative}$), which is calculated using a simple relative error formulation:

$$I_{relative} = \frac{\dot{m} - \dot{m}_{target}}{\dot{m}_{target}}, \quad 5-4$$

The integral factor is calculated as:

$$f_{integral} = C_{integral} \int_0^t I_{relative} dt, \quad 5-5$$

The adjustment of pressure drops starts with the block after the pump and proceeds sequentially to the block right before the pump. The sequence includes the pipe, mixing plate, core, and finally the pump choke. The parameters may influence each other in complex ways, necessitating multiple iterations to achieve satisfactory pressure drops in all calibration zones.

After completing the calibration process, we observe the pressure fields in Figure 5-4. As expected, there is a pressure drop from the pump outlet to the reactor outlet, with the majority of the pressure drop occurring at the pump choke. This observation underscores the importance of including the pump choke in the model.

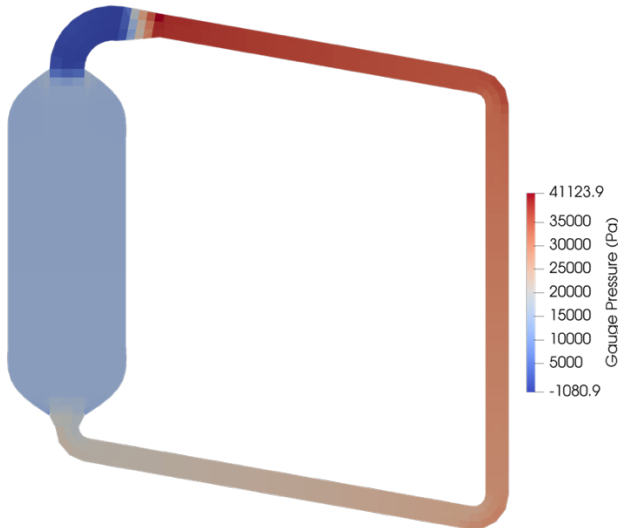


Figure 5-4. Gauge pressure field, with a reference point at the elbow before the pump inlet.

The velocity field, shown in Figure 5-5, exhibits the expected flow characteristics imposed by the pump. Velocity increases and decreases appropriately near elbows, and in regions with convergent and divergent nozzles. An artifact is present at the pump inlet, which may be attributed to the level of abstraction used for the pump, as it is the least well-known component with the most assumptions in the model. The velocity field also highlights the absence of boundary layers, suggesting potential benefits from their implementation.

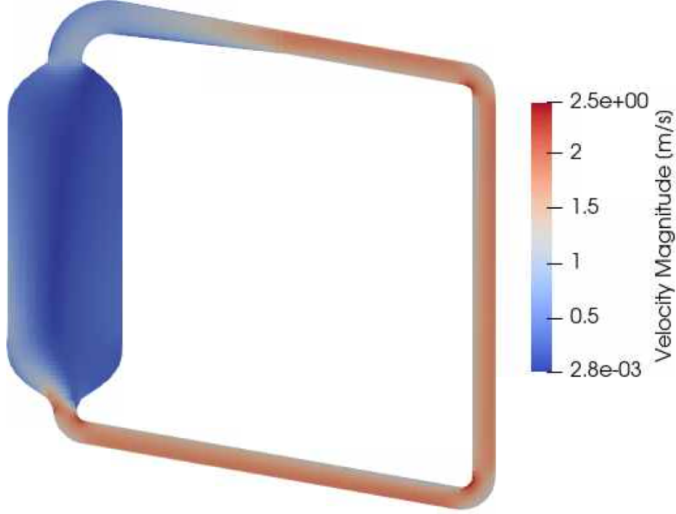


Figure 5-5. Velocity field during steady-state operation of L-MSR.

Table 5-3 summarizes the pressure drop results and their discrepancies compared to the Large Eddy Simulation (LES) reference model at a matched mass flow of 25 kg/s. The minimal discrepancies demonstrate that the MOOSE model has been calibrated effectively.

Table 5-3. Pressure drops per block and comparison with reference LES model.

	Mass Flow Rate	Δp_{pipe} [Pa]	Δp_{mixing_plate} [Pa]	Δp_{core} [Pa]	Δp_{pump_choke} [Pa]
LES Model	25.0	1.07e4	2.60e3	1.27e3	7.38e4
Pronghorn Model	25.0	1.067e4	2.576e3	1.273e3	7.97e4
Absolute Error [Pa]	-	-32	-24.4	3.1	5910
Relative Error	-	-0.3%	-0.94%	-0.24%	8.1%

Finally, after completing the case, it was restarted to verify that the conditions remained stable and consistent. The results confirmed that the converged conditions were successfully maintained during the restart, with no significant changes observed in the results.

5.3.2. Improvements in Microscopic Depletion in Griffin for L-MSR

The results obtained in FY24 for benchmarking Griffin against OpenMC v.0.15.2 and Serpent 2 have been updated to incorporate a new depletion model that yields higher accuracy. The issue with the model in FY24 was that the differences obtained in some of the fission products could have significantly biased the thermochemical results. The main differences are the following:

- Microscopic cross sections for depletion are tabulated every 0.01 kWd/kgHM, instead of the previous tabulation that was using 1.0 kWd/kgHM

- Depletion cross sections are tabulated considering the temperature of the fuel salt and reflector, which allows us to account for spectral shifts due to temperature variations; although the salt temperature does not have a considerable impact on depletion, the reflector temperature affect the results obtained

In all cases, predictor-only calculations were performed, i.e., without predictor-corrector steps, to keep the numerics in all solvers similar. The power history considered for the operation of the L-MSR is based in the planned operation for MCRE, which was reported in the open-source specifications of the MCRE by TerraPower. The operational history considered for the L-MSR depletion benchmark is detailed in Table 5-4. In brief, the reactor starts at low power operation and the power is gradually increased until 100 kWth for the primary experiments. Then, the reactor operates at its highest power of 150 kWth during 60 hours. As expected, due to the low power involved, the burnup of the reactor is small.

Table 5-4. Operation history modeled for the Lotus Molten Salt Reactor

Operating Condition	Power [kWth]	Time at Power [h]	Produced Thermal Energy [kWh]
Primary Experiments	0.1	697	70
	1	305	305
	10	60	600
	100	10	1000
Unallocated time at power	150	60	9000
		Total Hours	10,975

The evolution of the main elements of MCRE during operation, as predicted by the Griffin calculations, is depicted in Figure 5-6. As expected, due to the low power of the reactor and the large inventory of fuel salt in the core, the concentration of the constituent elements of the fuel salt remains approximately constant. This indicates that the thermophysical property of the salt and its chemical stability are unlikely affected by the depletion of the liquid nuclear fuel.

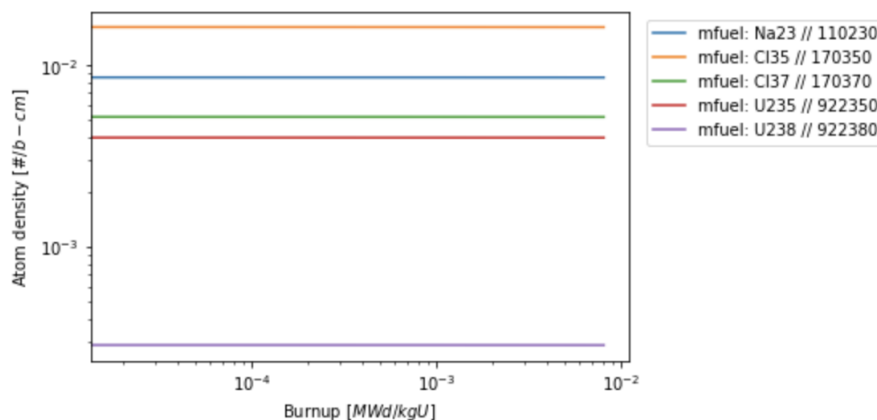


Figure 5-6. Evolution of the fuel salt main constituent nuclides of L-MSR during operation.

Along with the evolution of the constituent elements of the liquid nuclear fuel, the evolution of the FPs with the largest concentrations are shown in Figure 5-7. Due to the small burnup reached by the reactor core during operation, it is observed that FPs do not significantly buildup in the fuel salt. In every case, the concentration of the FPs with maximum concentration is at least 5 orders of magnitude smaller than the nuclide with the smallest concentration in the original nuclear fuel.

The small concentration of FPs during the operation of the reactor suggests that they could be neglected when performing best-estimate or safety analyses of this reactor. However, a different situation may be found when dealing with computing the reactor's mechanistic source term after accounting for all possible radionuclide transport pathways. Hence, it is important to verify Griffin's capabilities to accurately predict the inventory in the L-MSR when compared with the predictions of other codes.

As previously mentioned, the code benchmarking is performed between Serpent 2, OpenMC v. 13.1.0, and Griffin. All codes use the ENDF/B-VII.1 decay library for the depletion calculations. The single-group cross sections per isotope for performing the Griffin calculations were computed using Serpent 2. Both OpenMC and Serpent perform transport-coupled depletion, in which cross sections for depletion are re-computed at the end of each of the operation cycles detailed in Table 5-5. Due to the small burnup, spectral shifts were observed to have negligible impact on depletion. Hence, the cross sections used in the Griffin calculations were computed as the beginning-of-cycle cross sections and not updated during the depletion of the L-MSR.

Using Serpent 2 as the reference, the percent difference in the predicted isotopic concentrations by OpenMC and Griffin by the end of operation are presented in Table 5-5. It is observed that the difference in cementations obtained when comparing OpenMC vs Serpent 2 are generally smaller than the ones observed in the Griffin vs Serpent 2 comparison. However, in both cases, the differences obtained are reasonably small. This benchmark provides confidence on the usage of Griffin depletion capabilities for the L-MSR. However, in the future, this work needs to be extended to account for the impact of the circulating nuclear fuel on the depletion patterns obtained.

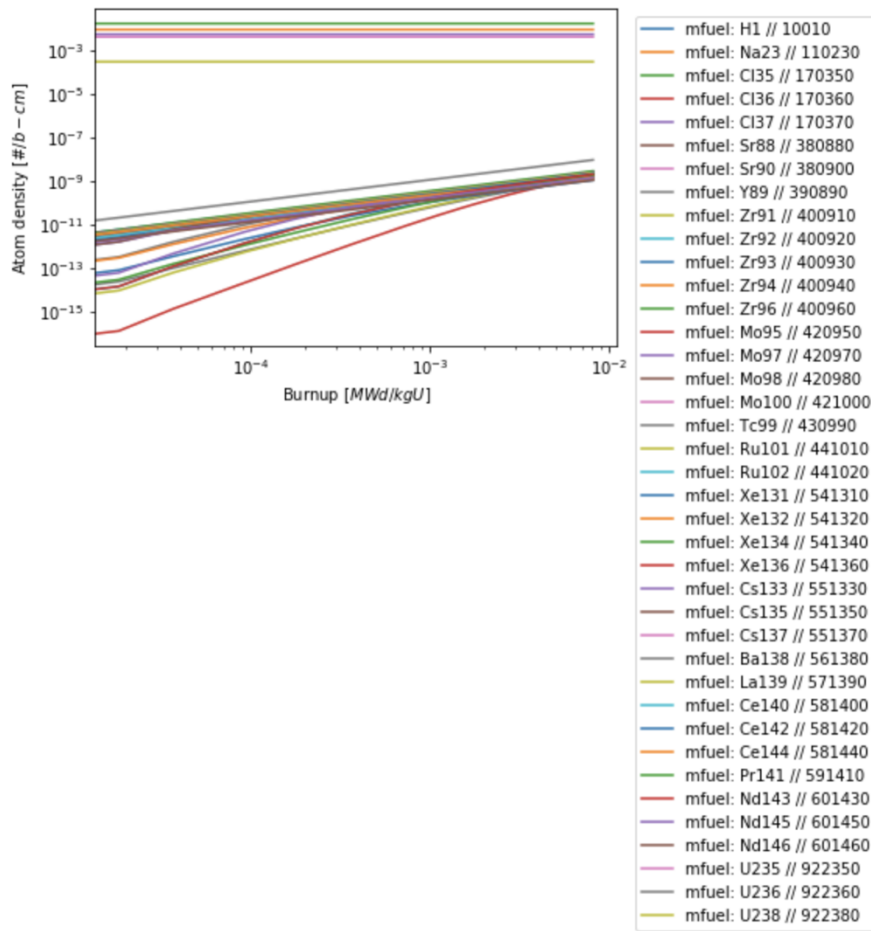


Figure 5-7. Evolution of the fuel salt main constituent nuclides and FPs with largest concentration of L-MSR during operation.

Table 5-5. Difference in predicted concentration by end of operation between OpenMC, Serpent 2, and Griffin. The Serpent 2 values are used as the reference ones.

Isotope	Category	OpenMC v. 13.1.0 vs Serpent 2	FY24 Griffin vs Serpent 2	FY25 Griffin vs Serpent 2
²³ Na	Salt Constituent	0.24%	0.45%	0.22%
³⁵ Cl	Salt Constituent	0.46%	1.49%	0.58%
³⁷ Cl	Salt Constituent	0.31%	0.19%	0.07%
²³⁵ U	Salt Constituent	0.37%	0.72%	0.34%
²³⁸ U	Salt Constituent	0.24%	1.14%	0.52%
⁸⁸ Sr	Fission Product	-0.16%	0.55%	0.23%
⁹⁰ Sr	Fission Product	-0.31%	0.14%	0.05%
⁸⁹ Y	Fission Product	-0.34%	1.14%	0.44%
⁹¹ Zr	Fission Product	-0.47%	1.04%	0.45%
⁹² Zr	Fission Product	-0.49%	-0.41%	-0.14%
⁹³ Zr	Fission Product	0.10%	-0.30%	-0.11%
⁹⁴ Zr	Fission Product	0.18%	0.37%	0.13%
⁹⁶ Zr	Fission Product	0.41%	1.18%	0.54%
⁹⁵ Mo	Fission Product	0.39%	1.22%	0.50%
⁹⁷ Mo	Fission Product	-0.38%	1.35%	0.60%
⁹⁸ Mo	Fission Product	0.33%	0.73%	0.26%
¹⁰⁰ Mo	Fission Product	-0.30%	0.96%	0.37%
⁹⁹ Tc	Fission Product	0.13%	-0.31%	-0.12%
¹⁰¹ Ru	Fission Product	-0.23%	1.37%	0.60%
¹⁰² Ru	Fission Product	0.24%	0.22%	0.10%
¹³¹ Xe	Fission Product	-0.43%	0.95%	0.42%
¹³² Xe	Fission Product	-0.49%	1.08%	0.42%
¹³⁴ Xe	Fission Product	0.36%	0.62%	0.27%
¹³⁶ Xe	Fission Product	0.30%	0.29%	0.11%
¹³³ Cs	Fission Product	-0.33%	0.34%	0.16%
¹³⁵ Cs	Fission Product	0.13%	0.03%	0.01%
¹³⁷ Cs	Fission Product	0.41%	1.50%	0.60%
¹³⁸ Ba	Fission Product	0.19%	-0.16%	-0.06%
¹³⁹ La	Fission Product	-0.49%	1.37%	0.56%
¹⁴⁰ Ce	Fission Product	-0.37%	-0.38%	-0.17%
¹⁴² Ce	Fission Product	-0.10%	0.19%	0.08%
¹⁴⁴ Ce	Fission Product	0.16%	0.77%	0.29%
¹⁴³ Nd	Fission Product	-0.17%	-1.29%	-0.50%
¹⁴⁵ Nd	Fission Product	0.33%	0.78%	0.27%
¹⁴⁶ Nd	Fission Product	0.40%	0.51%	0.19%
²³⁶ U	Activation Product	0.32%	0.51%	0.25%

5.3.3. Steady-State Results Analyses

This section examines the fully coupled steady-state operating point of the Lotus Molten Salt Reactor (L-MSR), using the calibrated hydraulics (Sec. 5.3.1) and the updated depletion configuration (Sec. 5.3.2) as the basis. The goals are to: (i) verify neutronics–thermal-hydraulics consistency at nominal conditions; (ii) quantify key fields that define the reactor’s baseline operating envelope; and (iii) provide high-fidelity initial conditions for the transient studies that follow.

The analyses focus on the spatial structure and self-consistency of the neutron source and heat release, the temperature–density state of the fuel salt, and the flow topology that governs mixing, transport, and wall loading. We also report closure-related diagnostics—surrogate turbulence quantities, derived transport coefficients, and near-wall resolution indicators—to assess modeling adequacy for engineering-scale predictions. Where relevant, we include steady proxies for thermochemical response to illustrate how the thermal-hydraulic state can couple to interfacial chemistry in later sections.

The results below are organized to address:

- **Power and source consistency:** power-density and fission-source distributions under the converged eigenvalue solution, used to confirm conservative mapping and energy balance.
- **Thermal state:** three-dimensional temperature and density fields of the salt, identification of hot spots, and buoyancy patterns with implications for reflector heat load.
- **Flow topology:** streamline structure near inlets, elbows, and recirculation regions, with discussion of their impact on scalar transport and mixing length scales.
- **Conjugate heat transfer:** heat fluxes into neighboring solids and the resulting gradients that set structural and corrosion-relevant boundary conditions.
- **Turbulence and transport closures:** representative turbulence variables and the implied turbulent viscosity, thermal conductivity, and mass diffusivity used by the RANS-grade model.
- **Near-wall adequacy:** wall-distance indicators (e.g., y^+) to gauge boundary-layer resolution and appropriateness of wall treatments across core and reflector surfaces.
- **Kinetics consistency:** a brief check on delayed-neutron-precursor advection/decay under the steady flow to clarify its contribution to the effective source term.

Together, these steady-state results close the verification loop for the nominal operating condition and establish a quantitatively consistent baseline from which pump-driven, buoyancy-driven, and thermochemistry-coupled transients will be initialized in subsequent subsections.

Figure 5-8 presents the steady-state neutronic fields for the L-MSR in two complementary forms: the volumetric power density, $q'''(r)$, and the volume-normalized fission source, $\hat{S}_f(r)$. The power density is the recoverable thermal energy deposited per unit volume, while the normalized fission source represents the spatial distribution of fission events per unit volume, scaled so that its core-volume integral is unity. Displaying the two maps side-by-side enables a direct assessment of spatial coherence in the k-eigenvalue solution and a quick visual check that the heat-generation field used by the thermal-hydraulic solver is consistent with the underlying fission source.

In steady state, the mapping between these fields is given by $q'''(r) = E_f S_f(r)$, where E_f is the recoverable energy per fission and $S_f(r) = \nu \Sigma_f(r) \varphi(r)$ is the local fission rate density. The figure uses the normalized source $\hat{S}_f(r) = S_f(r) \int_{\Omega} S_f dV$ to emphasize shape over magnitude. Because $q'''(r)$ and $\hat{S}_f(r)$ differ only by a constant scale factor and the normalization, their spatial structures should be congruent: peaks, troughs, and isosurfaces ought to co-locate across the two panels. This congruence is a

necessary condition for energy conservation, since the domain integral of $q'''(r)$ must match the target thermal power within solver tolerances.

The spatial structure observed in Figure 5-8 follows the expected physics. Radially, the fields peak in moderated, high-flux interior regions and roll off toward the reflector as neutron leakage increases and the spectrum hardens. Axially, the profile is approximately cosine-like, with mild skewness introduced by temperature-dependent feedback (Doppler broadening and salt-density changes) and by inlet/outlet boundary conditions. In upward flow, hotter upper regions slightly depress reactivity, whereas cooler lower regions slightly enhance it, producing a modest down-shift in the axial peak location. The smoothness of the contours—absence of spurious oscillations or block-wise artifacts—also indicates proper cross-section interpolation and conservative mapping between the neutronics and thermal-hydraulics meshes.

Several internal consistency checks are naturally enabled by these plots. First, alignment of salient features in $q'''(r)$ and $\hat{S}_f(r)$ confirms that the recoverable energy per fission, cross-section treatment, and field transfers are coherent. Second, the visual agreement complements the quantitative power balance check $\int_{\Omega} q''' dV \approx P_{set}$. Third, the sharpness of radial gradients at the core–reflector interface reflects net leakage and moderation efficacy; steeper edges imply stronger leakage, whereas flatter edges suggest more effective moderation near boundaries. Fourth, localized depressions of $\hat{S}_f(r)$ in high-temperature regions are consistent with negative temperature coefficients and provide a qualitative fingerprint of feedback operating as intended. Finally, because delayed-neutron precursors are sourced by $S_f(r)$, the right-hand panel directly informs the precursor advection–decay problem that accompanies the steady flow.

The implications for the coupled model are direct. A close correspondence between the two fields yields a stable and physically grounded heat-generation map for the thermal-hydraulic solver, helping to avoid artificial hot spots or mismatched cooling demands. The radial roll-off sets the reflector heat-flux footprint used in conjugate heat-transfer evaluations and informs structural loading. From a verification standpoint, we recommend reporting alongside Figure 5-8: the core-integrated power error $|\int q''' dV - P_{set}|/P_{set}$; the spatial correlation between q'' and \hat{S}_f and a normalized L2 discrepancy; peak-to-average factors and the coordinates of maxima; and an edge-gradient metric at the core–reflector interface as a leakage indicator. Together, these summaries quantify the qualitative impressions conveyed by the figure and establish that the neutronic source and deposited power form a coherent basis for subsequent thermal-hydraulic and delayed-neutron-transport analyses.

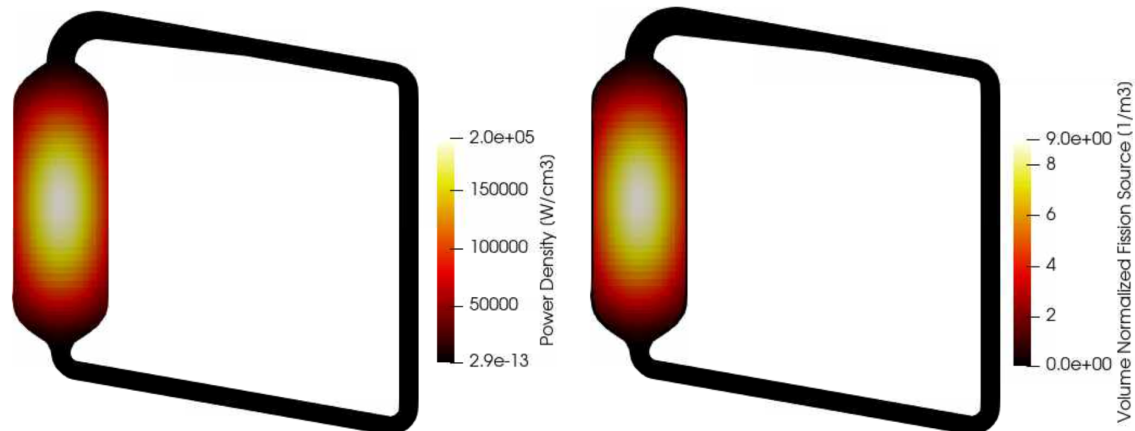


Figure 5-8. Left: power density during the steady-state operation of the L-MSR. Right: volume-normalized fission source during the steady-state operation of the L-MSR.

Figure 5-9 illustrates the distributions and relative behavior of the first six delayed neutron precursor groups under the established steady-state operating condition. These groups, commonly labeled 1 through 6 in ascending decay rate, represent the dominant fraction of the total delayed neutron yield and therefore strongly influence reactor kinetics and stability during nominal operation and in the initial phases of transients. Displaying the group-wise precursor fields side-by-side enables direct comparison of how production by the fission source and losses by radioactive decay and transport shape the spatial structure of each group.

Two physical time scales govern the appearance of these maps: the group decay constants and the hydrodynamic residence times. For the L-MSR configuration used here, a representative fuel circulation time is roughly 10 seconds. By contrast, the first six groups have decay constants $\lambda \approx \{0.0125, 0.0283, 0.0425, 0.133, 0.292, 0.666, 1.635, 3.555\} \text{ s}^{-1}$, which correspond to mean lifetimes $\tau = 1/\lambda$ of about $\{80.2, 35.3, 23.5, 7.52, 3.42, 1.50, 0.61, 0.28\} \text{ s}$ and half-lives $t^{1/2} = \ln(2)/\lambda$ of about $\{55.6, 24.5, 16.3, 5.21, 2.37, 1.04, 0.42, 0.20\} \text{ s}$. The long-lived groups (1–3) therefore persist over multiple passes around the loop and appear more spatially smeared, tracking the broader circulation. The shorter-lived groups (4–8) decay on time scales comparable to or shorter than the loop transit time and are consequently more localized near high-source regions and along primary flow paths immediately downstream of the core.

The magnitude ordering visible across the groups reflects both decay and yield. In the adopted dataset, the fractional yields (as a share of the total delayed fraction) for groups 1 through 6 are approximately $\{3.5\%, 14.6\%, 10.1\%, 20.0\%, 31.3\%, 9.5\%\}$. Groups 4 and 5 dominate the total delayed fraction, but their shorter half-lives limit the spatial extent of their concentrations; groups 1–3 contribute less per fission but remain present throughout a larger portion of the loop. This interplay—yield versus lifetime—explains why the long-lived groups provide a relatively uniform background of precursors while the short-lived groups highlight the immediate vicinity of the neutron source and near-core recirculation structures.

These patterns have direct implications for coupled kinetics. Because the effective delayed source encountered by the neutron field depends on the location of precursor decay, long-lived groups tend to preserve delayed reactivity feedback even when material is transported out of the core, whereas short-lived groups make the delayed component more sensitive to local flow and mixing near the active region. In practical terms, the figure confirms that the model captures the expected gradient from broad, advectively smeared distributions (groups 1–3) to localized, source-peaked distributions (groups 4–6), consistent with the relative magnitudes of decay constants and the loop residence time.

Table 5-6 reports the eight delayed neutron precursor groups used in the kinetics and transport model, listing each group's fission yield (in pcm) and decay rate (s^{-1}). The sum of the yields is 719.92 pcm, corresponding to a total delayed neutron fraction $\beta_{\text{eff}} \approx 0.0071992$. The distribution is strongly weighted toward the middle groups: group 5 contributes $\approx 31\%$, group 4 $\approx 20\%$, group 2 $\approx 15\%$, and group 3 $\approx 10\%$ of β_{eff} , with the remaining share split among groups 6–8 and 1. This allocation underscores that the bulk of the delayed source is provided by groups with intermediate lifetimes.

In the steady, circulating-fuel setting, each group obeys a precursor balance of the form $\text{production} \approx \text{decay} + \text{advection} + \text{diffusion}$, with production proportional to the local fission source and weighted by the group yield. Consequently, for groups with long lifetimes (small λ), the advective term is comparatively important and the spatial distribution is extended; for groups with short lifetimes (large λ), decay outpaces transport and the distribution is confined near regions of high fission rate. The values in Table 8 quantify these tendencies and, when combined with the hydrodynamic residence times, explain the qualitative differences observed across the group-wise patterns in Figure 5-9.

Beyond qualitative insight, the table enables several quantitative consistency checks that are reported alongside the steady-state results: (i) reconstruction of β_{eff} from the listed yields; (ii) verification that the spatially integrated decay of all groups equals the spatially integrated production at steady state; and (iii) sensitivity studies that vary loop residence time or local temperature to assess how changes in transport or

cross-section temperature dependence shift the relative importance of short- versus long-lived groups. Together, Figure 5-9 and Table 5-6 demonstrate that the delayed neutron model is internally consistent and appropriately coupled to the flow field at nominal conditions, providing a reliable baseline for subsequent transient analyses.

Table 5-6. Delayed neutron precursor groups including fission yields and decay rates.

Delayed Neutron Precursor Group	Fission Yield [pcm]	Decay Rate [1/s]
Group 1	25.05	0.0124667
Group 2	104.89	0.0282917
Group 3	72.68	0.0425244
Group 4	143.74	0.133042
Group 5	225.03	0.292467
Group 6	68.07	0.666488
Group 7	63.18	1.63478
Group 8	17.28	3.5546
Total	719.92	NA

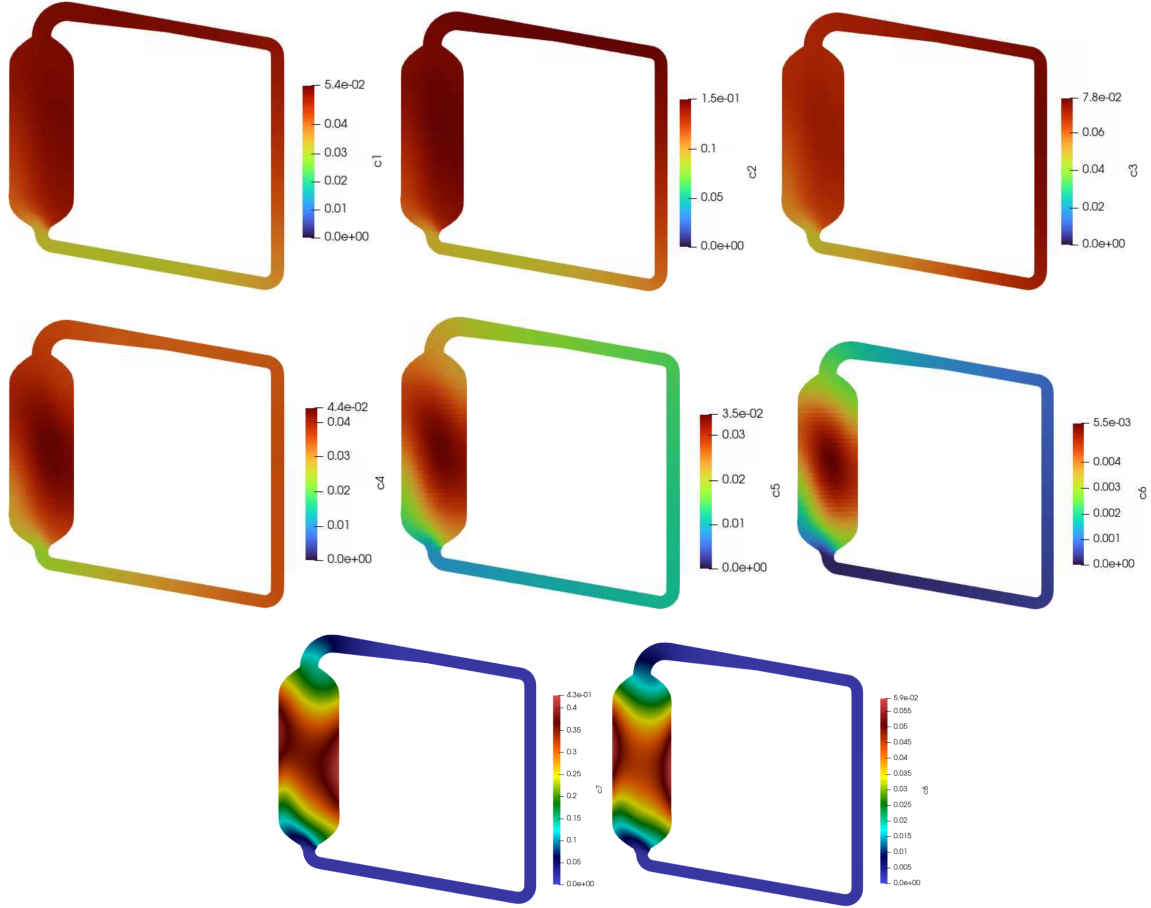


Figure 5-9. Normalized concentration of delayed neutron precursors. The fission yield and decay rate of each of the species presented are outlined in Table 5-6.

Figure 5-10 presents, on the left, the three-dimensional temperature field $T(r)$ of the circulating fuel salt at the converged steady state and, on the right, the corresponding density distribution $\rho(r)$ within the reactor core. The temperature map reflects volumetric heating by fission in the active region, convective transport along the main flow paths, and heat removal through the solid boundaries via conjugate heat transfer. Peak temperatures are centered in high-power-density zones and decrease toward outlet plenum regions and cooled boundaries. The contours remain smooth without unphysical oscillations, indicating stable coupling and conservative field transfers across the multiphysics meshes.

The density profile is the thermally expanded counterpart of the temperature field. For the salt equation of state used in this model, density is represented as $\rho(T) \approx \rho_{ref} \cdot [1 - \beta_T \cdot (T - T_{ref})]$, where β_T is the volumetric thermal expansion coefficient at the reference state (T_{ref}, ρ_{ref}) . The right-hand panel therefore exhibits an inverse correlation with $T(r)$: hotter core regions appear less dense, whereas cooler regions near inlets and conductive boundaries remain denser. The resulting density contrast $\Delta\rho/\rho_{ref} \approx \beta_T \cdot \Delta T$ provides a quantitative measure of buoyancy potential that can augment or oppose the forced flow, depending on local alignment with gravity.

Physically, the pair $\{T(r), \rho(r)\}$ encodes the baseline thermal load and the associated stratification tendencies. A modest radial roll-off of T near the core–reflector interface is consistent with conductive heat leakage into the reflector, while axial skewness reflects inlet/outlet placement and

temperature-feedback effects in the neutronic source. In upward core flow, slightly lower ρ in the upper portion of the active region is expected and contributes to weak buoyancy-assisted motion there, while denser inflow at the bottom helps stabilize the entrance region. The observed inverse alignment of temperature and density maxima/minima is a primary validation point for the material model and field mapping.

Recommended quantitative summaries to accompany Figure 24 include: core-volume extrema and peak-to-average values for T ; the core-averaged ΔT across the active region; a histogram or cumulative distribution of T to characterize hot-spot extent; and an estimate of $\Delta\rho/\rho_{ref}$ via the model's β_T . For buoyancy relevance, reporting Grashof-to-Reynolds ratios, e.g., $Ri \approx Gr/Re^2$ with $Gr = g \cdot \beta_T \cdot \Delta T \cdot L^3/v^2$, helps indicate where natural-convection effects may alter local mixing relative to purely forced convection.

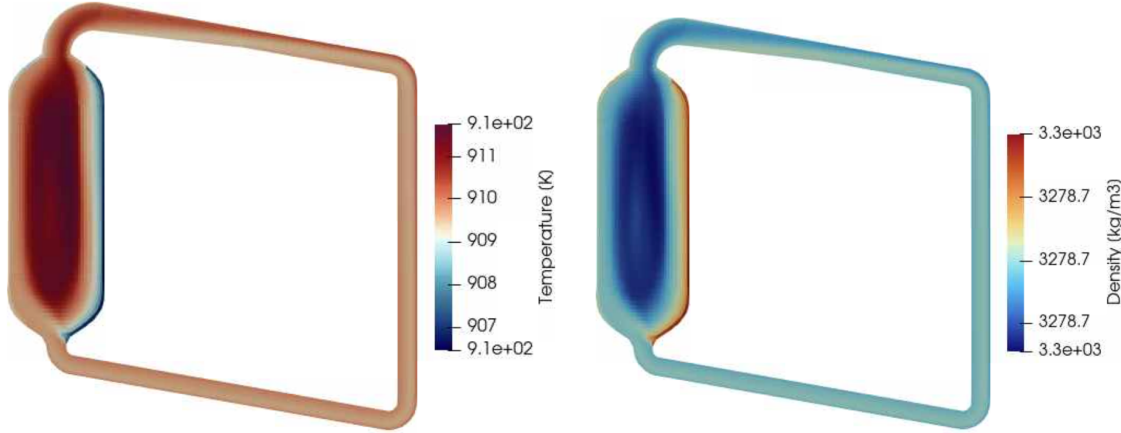


Figure 5-10. Left: detailed temperature field in the fuel salt during operation. Right: density profile within the reactor core.

Figure 5-11 overlays steady streamlines through the core with temperature coloring and, alongside, displays the temperature field within the graphite (or equivalent) reflector. The streamline picture reveals the primary flow channels, entrance development, and any localized recirculation near geometric features such as the mixing plate, elbows, or contractions/expansions. Temperature tinting along the streamlines highlights convective transport of thermal energy, delineating hot plumes leaving high-source regions and cooler jets entering from the inlet. Regions of streamline crowding coincide with higher convective heat transport; sparse regions indicate lower throughflow and potential thermal residence.

The reflector panel evidences conjugate heat transfer (CHT) from the salt to the solid. At the interface, the normal heat flux is continuous, $q_n = -k_f \cdot (\nabla T_f \cdot n) = -k_s \cdot (\nabla T_s \cdot n)$, and the temperatures match, $T_f = T_s$. The reflector temperature gradients closest to the interface map the wall-heat-flux footprint imposed by the core; deeper into the solid, diffusion spreads the thermal field according to $\nabla \cdot (k_s \nabla T_s) = 0$ (steady conduction). The shape and thickness of interfacial isotherms provide a qualitative indicator of local heat-transfer coefficients on the fluid side: sharper drops imply higher convective coefficients, while broader transitions suggest milder convection.

Coupled implications follow. First, the correspondence between hot streamline bundles and elevated reflector temperatures identifies locations of larger structural thermal gradients and potential thermal-stress concentration. Second, the wall-adjacent temperature field in the salt sets boundary conditions for near-wall modeling (e.g., wall functions and property evaluation) used in turbulence closures reported later in this section. Third, the CHT picture helps prioritize mesh refinement and material-property sensitivity in zones where the thermal footprint is steepest. For documentation, we

recommend reporting interfacial heat-flux statistics (area-averaged and peak values), wall temperature extrema, and an effective Nusselt number based on local bulk temperature and hydraulic diameter to anchor the CHT interpretation.

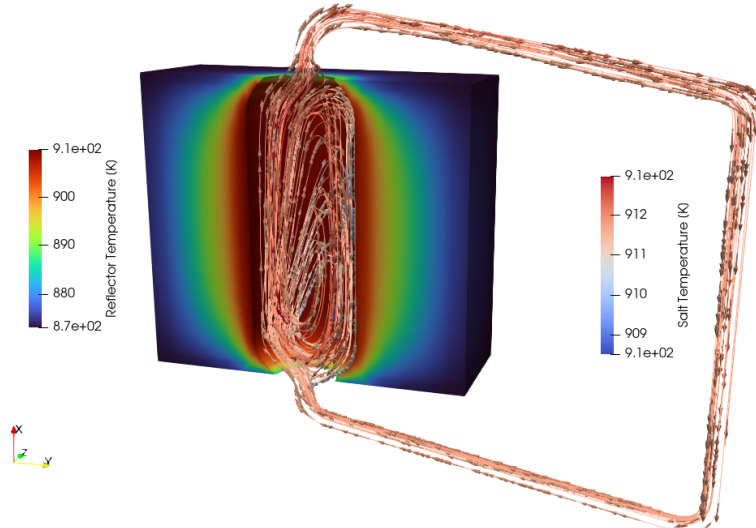


Figure 5-11. Streamlines in the reactor core during operation colored with the temperature field and temperature in the reactor reflector. Heat is transmitted from the reactor core into the reflector via conjugate heat transfer.

Figure 5-12 zooms into the recirculation region adjacent to the reactor inlet and colors the fluid domain by the angular-velocity magnitude, a proxy for local rotational motion rate. This view isolates vortical structures triggered by the inlet geometry and by rapid curvature or area change. The recirculation bubble size, the peak rotational rates, and the trajectories of re-entrant flow characterize how incoming, relatively cooler salt mixes with the hotter core fluid. These features govern scalar homogenization, local shear, and wall heat-transfer augmentation near the entrance.

From a mixing perspective, the ratio of the eddy-turnover time $\tau_e \approx 1/\omega$ (with ω a representative angular-velocity magnitude) to the throughflow residence time in the entrance control volume indicates whether vortices can effectively homogenize temperature before the stream re-enters the core bulk. If $\tau_e \ll \tau_{\text{res}}$, strong local mixing reduces thermal streaking; if $\tau_e \gtrsim \tau_{\text{res}}$, thermal inhomogeneities may persist, potentially promoting striping or localized hot/cold impingement at nearby walls. The observed angular-velocity field thus provides a direct diagnostic for entrance-mixing adequacy under the modeled operating point.

The accompanying reflector temperature map again documents the CHT response to the entrance-region dynamics. Elevated angular-velocity zones often correlate with enhanced convective coefficients and, therefore, with steeper interfacial thermal gradients in the adjacent solid. Conversely, stagnant pockets within or downstream of the recirculation bubble may show muted reflector heating. For verification and design iteration, we recommend summarizing: the maximum and integral of angular-velocity over the entrance control volume; an estimated reattachment length (or recirculation extent) normalized by local hydraulic diameter; entrance-region heat-flux statistics; and sensitivity to inlet boundary conditions (velocity profile, turbulence intensity) to bracket uncertainty in the recirculation topology.

Taken together, Figure 5-10–Figure 5-12 establish a coherent thermal–hydraulic baseline at steady state: the temperature and density fields quantify the thermodynamic state and buoyancy potential; the streamline and reflector fields delineate the conjugate heat-transfer footprint; and the inlet-adjacent recirculation analysis clarifies entrance mixing and wall-loading mechanisms. These results provide the

necessary context and metrics for the turbulence, transport, and near-wall assessments that follow, and they define a stable set of initial conditions for the subsequent transient studies.

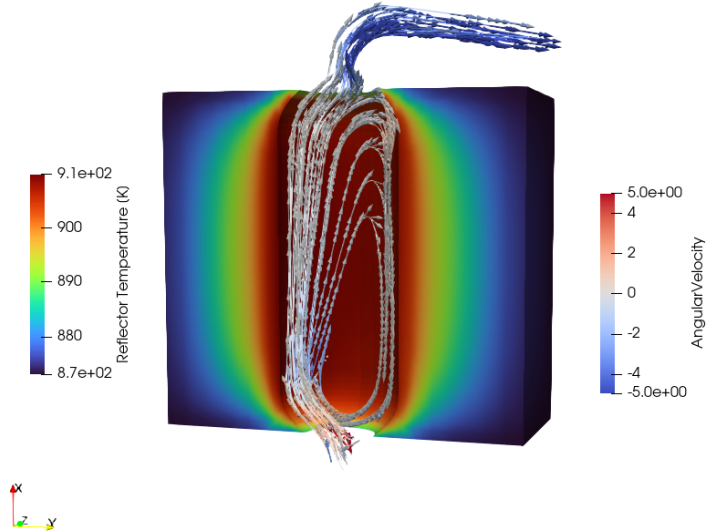


Figure 5-12. Detailed model showcasing the fuel salt recirculation region next to the reactor inlet, colored with the angular velocity, and the temperature field in the reactor reflector.

Figure 5-13 displays, side by side, the steady-state maps of the turbulent kinetic energy $k(r)$ and the turbulence dissipation rate $\epsilon(r)$ (or an equivalent rate variable for the chosen two-equation closure). Together these fields summarize how shear production, transport, and near-wall destruction of turbulence are distributed throughout the L-MSR flow domain. The k field (units m^2/s^2) highlights regions of intense velocity fluctuations generated by mean shear; peak values commonly align with mixing layers, entrance and exit contractions, elbows, and recirculation structures at geometric discontinuities. In contrast, the dissipation rate ϵ (units m^2/s^3) concentrates where the smallest turbulent scales are active—typically adjacent to walls, within thin shear layers, and in the cores of strong vortical structures where strain rates are largest.

The spatial relationship between k and ϵ provides a qualitative health check on the closure and the mesh. Where k is elevated in broad regions but ϵ remains focused near walls and sharp gradients, the model is capturing production in bulk shear while correctly confining dissipation to boundary layers and thin mixing zones. Conversely, co-located spikes of k and ϵ at isolated cells can indicate excessive numerical diffusion, under-resolution, or overly stiff damping from the near-wall model. In the L-MSR geometry, we expect strong k in the core outlet/upflow region, at the entrance to the chimney/riser and around the inlet-adjacent recirculation bubble, with ϵ peaking along the walls of the fuel channels, near the mixing plate features, and at turns where shear is most intense.

Physically consistent $k-\epsilon$ patterns support stable heat-transfer predictions and credible scalar mixing. Elevated k in the core bulk enhances momentum and scalar transport, improving thermal homogenization and damping temperature streaks, while high ϵ at the walls helps maintain realistic boundary-layer thicknesses. For documentation alongside Figure 5-13, it is useful to report volume-averaged k and ϵ , the locations and magnitudes of their peaks, and integral production–dissipation balance checks within selected control volumes; these metrics quantify the qualitative impressions conveyed by the plots and help target mesh refinement to zones with large gradients or closure sensitivity.

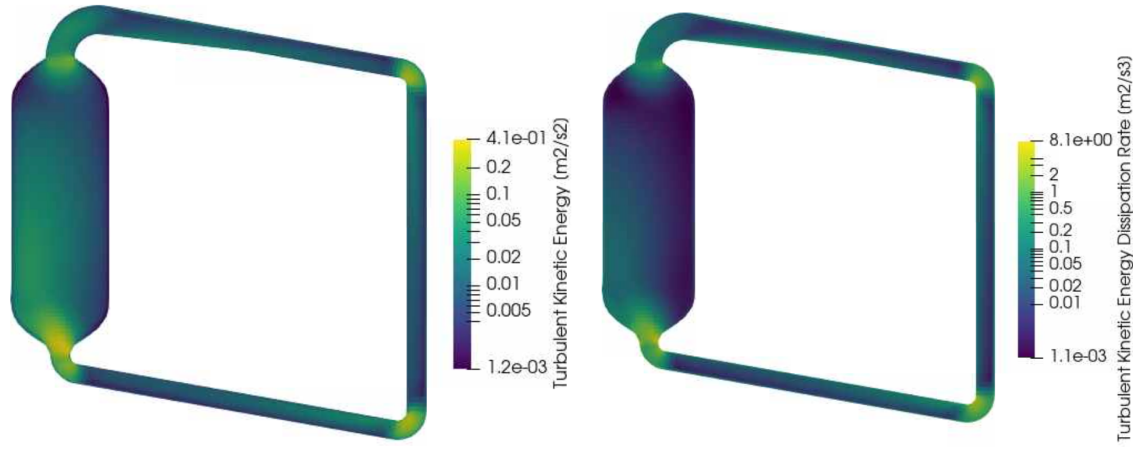


Figure 5-13. Surrogate turbulence fields during the operation of the L-MSR. Left: turbulent kinetic energy. Right: turbulent kinetic energy dissipation rate.

Figure 5-14 presents the transport-coefficient fields derived from the turbulence closure: the dynamic turbulent viscosity μ_t , the turbulent mass (species) diffusivity D_t , and the turbulent thermal conductivity k_t . These fields connect the surrogate turbulence variables from Figure 27 to the effective transport of momentum, species, and heat used in the RANS-grade model. In a $k-\varepsilon$ formulation one typically has $\mu_t \approx \rho C_\mu k^2 / \varepsilon$, whereas in a $k-\omega$ formulation $\mu_t \approx \rho k / \omega$; in either case μ_t maps directly to the local enhancement of momentum transport over the molecular viscosity. The corresponding scalar diffusivities follow standard gradient-diffusion assumptions: the turbulent mass diffusivity can be expressed using a turbulent Schmidt number Sc_t as $D_t \approx (\mu_t / \rho) / Sc_t$, and the turbulent thermal conductivity is linked via a turbulent Prandtl number Pr_t as $k_t \approx \mu_t c_p / Pr_t$. With commonly used values $Sc_t \approx O(1)$ and $Pr_t \approx 0.9$, regions of high μ_t translate into proportionally enhanced species and heat transport.

The μ_t field concentrates where k is large and ε (or ω) is moderate, corresponding to persistent shear layers and recirculating zones that promote mixing. The D_t map mirrors μ_t once normalized by density, highlighting where dissolved species (e.g., fission products or corrosion surrogates) are advected and diffused most efficiently. The k_t distribution indicates where convective heat-transfer coefficients are effectively augmented by turbulence, often aligning with wall regions subject to high heat flux and with flow passages of elevated shear. Consistency among μ_t , D_t , and k_t —similar hot spots and smooth variations without spurious checkerboarding—indicates that the closure is behaving smoothly and that the mesh quality and coupling are adequate.

From a design and verification standpoint, these transport maps guide where additional resolution or property sensitivity is most impactful. High μ_t corridors mark paths of rapid momentum and scalar exchange that help homogenize temperature and species fields but can also focus heat flux onto specific wall sections. Reporting domain-averaged and wall-adjacent statistics of μ_t , inferred Nusselt numbers based on k_t , and effective turbulent Schmidt and Prandtl numbers recovered from the fields provides a quantitative anchor to the qualitative interpretation of Figure 5-14 and supports comparisons across operating conditions.

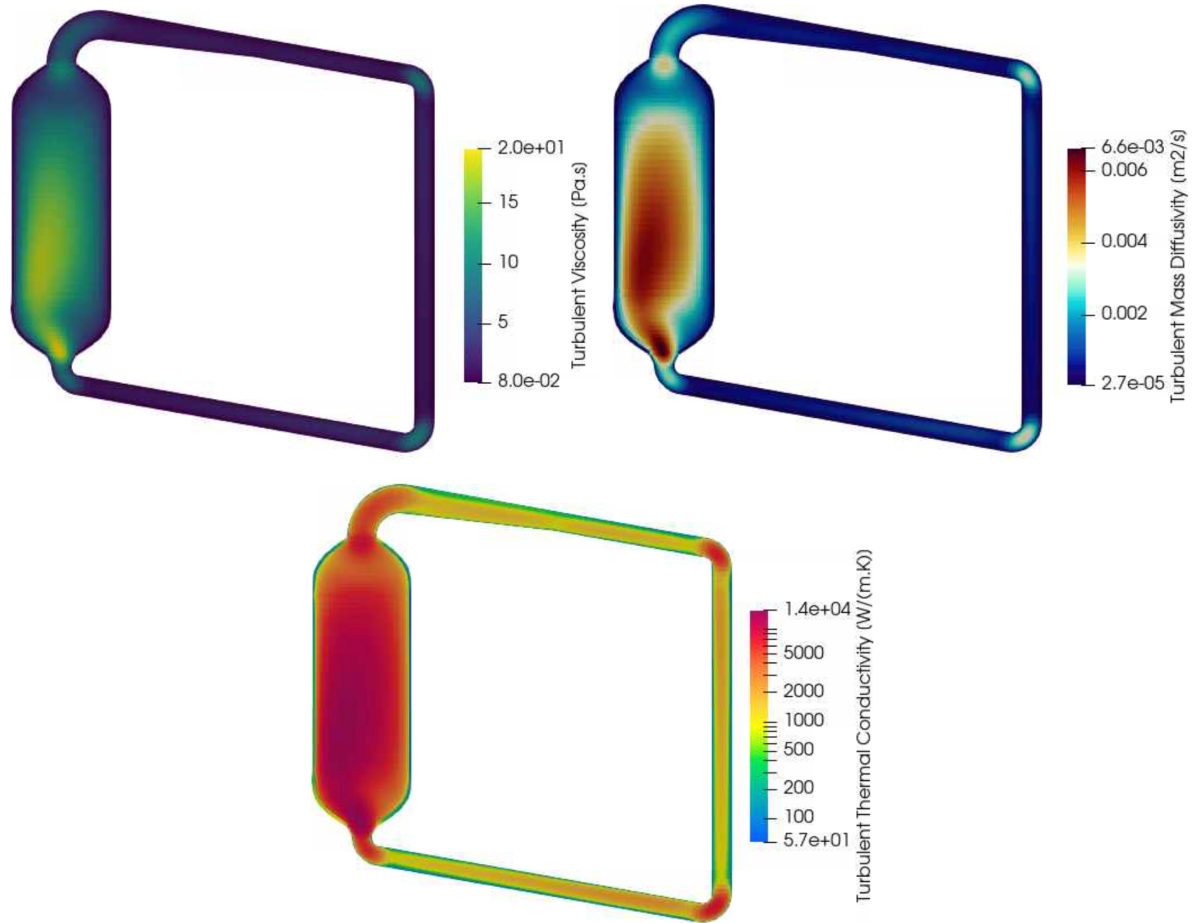


Figure 5-14. Turbulent diffusivity fields during the operation of the L-MSR. Top-left: dynamic turbulent viscosity. Top-right: turbulent mass diffusivity. Bottom: turbulence heat conductivity.

Figure 5-15 depicts the non-dimensional wall distance y^+ across wall-adjacent cells. By definition, $y^+ = \rho u_\tau y / \mu$, where y is the normal distance from the wall to the first computational point, ρ and μ are the local density and dynamic viscosity, and $u_\tau = \sqrt{\tau_w / \rho}$ is the friction velocity based on wall shear stress τ_w . The y^+ field is a primary indicator of whether the near-wall treatment is consistent with the modeling approach. If resolving the viscous sublayer with a low-Re treatment, most wall-adjacent nodes should satisfy $y^+ \lesssim 1-2$. If using log-law wall functions, the target band is typically $30 \lesssim y^+ \lesssim 200$ (or case-specific guidance from the chosen wall model).

Interpreting the map proceeds by identifying contiguous areas that fall within, below, or above the target range. Extended patches with y^+ well below the intended band suggest over-resolution relative to the wall model and potential underprediction of shear; conversely, very high y^+ values imply under-resolution and a risk of inaccurate wall shear and heat transfer. In the L-MSR geometry, elevated y^+ commonly appears along high-speed channels and at sharp turns, while reduced y^+ occurs near stagnation points and within recirculation pockets. A healthy distribution shows smooth gradients along streamwise directions and avoids checkerboarding or isolated spikes that could indicate mesh quality issues.

For documentation alongside Figure 5-15, it is useful to provide area-weighted statistics of y^+ (mean, median, and percentile bands), the percentage of wall area within the target range for the adopted treatment, and maximum y^+ values at critical interfaces (e.g., near the reflector and mixing plate). These summaries, together with the turbulence and transport fields in Figures 27 and 28, confirm that near-wall

shear and heat transfer are being modeled with appropriate fidelity at the steady-state operating point and establish a reliable baseline for subsequent transient simulations.

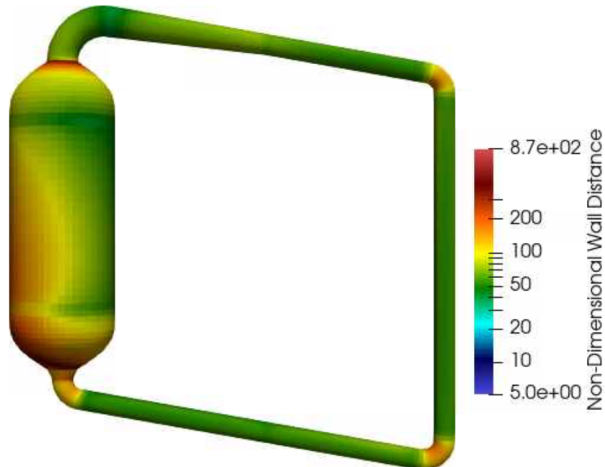


Figure 5-15. Non-dimensional wall distance.

Collectively, Figure 5-13–Figure 5-15 demonstrate that the surrogate turbulence fields, derived transport coefficients, and near-wall resolution form a self-consistent foundation for engineering-scale predictions at nominal conditions. The observed structure of k and ε (or ω), the aligned hot spots in μ_t , D_t , and k_t , and the y^+ distribution appropriate to the selected wall treatment together support credible estimates of mixing, heat transfer, and wall loading throughout the L-MSR flow domain.

Figure 5-16 provides a steady-state view of corrosion-relevant thermochemical proxies in the circulating fuel salt and at fluid–solid interfaces. The left panel shows a bulk redox indicator (e.g., an electrochemical potential field or an activity ratio for a controlling redox pair), while the right panel summarizes a wall-dissolution tendency index derived from the local departure from redox equilibrium. Together, these maps tie the thermal–hydraulic state to corrosion propensity: temperature and mixing set species activities and transport, which in turn shift equilibrium and govern interfacial reaction rates.

At thermodynamic equilibrium, the potential of a redox couple follows a Nernst-type relation, $E_{eq}(T, a_i) = E_0 + (R T / (n F)) \ln(Q)$, where Q is the ratio of oxidized to reduced activities for the controlling reaction, n is the electron number, F is Faraday's constant, R is the gas constant, and T is temperature. We define an overpotential $\eta = E_m - E_{eq}(T, a_i)$, where E_m represents the modeled redox state of the molten salt. Positive η favors anodic dissolution of susceptible alloying elements; negative η favors reduction/plate-out of noble and semi-noble species. In a Butler–Volmer form, the magnitude of the interfacial current scales approximately as $i \approx i_0 [\exp(\alpha_a F \eta / (R T)) - \exp(-\alpha_c F \eta / (R T))]$, linking the equilibrium departure to a reaction rate. The wall-dissolution index in the right panel is a proxy for this kinetics, highlighting locations at which η and temperature jointly increase corrosion risk.

Spatially, the bulk redox field correlates with temperature and mixing patterns. Hot, weakly mixed regions can shift E_{eq} and deplete local reducers, producing elevated η and a higher dissolution tendency. Conversely, zones of strong mixing and cooler inflow tend to suppress η by replenishing reductants and lowering activity ratios, reducing anodic driving forces. Near-wall gradients in the proxy field emphasize the role of mass-transfer boundary layers: thicker layers increase concentration polarization and can raise η at the surface even when the bulk is moderately reducing. This behavior explains the frequent co-location of high dissolution index with recirculation boundaries and regions of streamline sparsity seen elsewhere in the steady-state solution.

Recommended reporting alongside Figure 5-16 includes the distribution of η over wetted surfaces (area-weighted mean, percentiles, maxima), a summary of the bulk redox indicator (min/mean/max and volume fraction above threshold), and correlation coefficients between η and local wall temperature and shear. These metrics quantify how much of the corrosion risk is thermally driven versus transport limited and help prioritize mitigation strategies (e.g., enhanced mixing, targeted cooling, or redox-buffering additions).

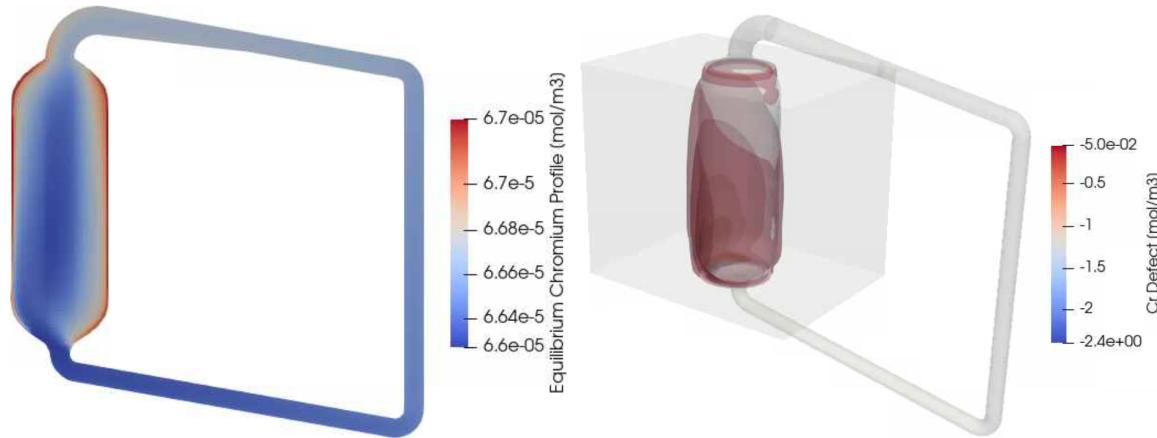


Figure 5-16. Example of corrosion results after 100,000 seconds of operation. Left: equilibrium dissolved chromium concentration in the fuel salt. Right: defect chromium concentration at the solid-liquid interface due to corrosion.

Figure 5-17 focuses on the transport and deposition of representative noble or semi-noble fission products and corrosion products. The left panel shows a wall-normal deposition (plate-out) flux $J_{\text{plate}}(r_w)$ [$\text{kg} \cdot \text{m}^{-2} \cdot \text{s}^{-1}$], while the right panel shows the corresponding bulk concentration field $C_{\text{metal}}(r)$ for the species family. These quantities are coupled: plate-out is driven by both interfacial kinetics and mass transfer through the near-wall layer, and the bulk concentration evolves via advection-diffusion-reaction along the primary flow paths.

A convenient representation for the deposition rate is $J_{\text{plate}} \approx k_m (C_b - C_{\text{eq}})$, where k_m is a mass-transfer coefficient, C_b is the bulk concentration adjacent to the wall, and C_{eq} is the near-wall equilibrium concentration implied by the local redox state. The coefficient k_m can be expressed through a Sherwood number $Sh = k_m L / D_{\text{eff}}$, where L is a characteristic length and D_{eff} is the effective diffusivity that includes turbulent transport ($D_{\text{eff}} = D_{\text{mol}} + D_{\text{t}}$). For internal turbulent flows, Sh typically scales with flow and property non-dimensional groups, for example, $Sh \propto Re^m \cdot Sc^n$, with $m \approx 0.8$ and $n \approx 0.3$ for many duct-like configurations. As a result, regions of high shear and elevated turbulent diffusivity (identified in the transport-coefficient fields) exhibit larger k_m and, for a given $(C_b - C_{\text{eq}})$, larger J_{plate} .

Interpreting the figure proceeds by linking the deposition map to both transport and chemistry. Where the right-panel $C_{\text{metal}}(r)$ is high and the local redox state makes C_{eq} low (chemically favorable reduction), the left-panel plate-out flux is elevated. Conversely, low bulk concentration or a near-equilibrium wall condition ($C_b \approx C_{\text{eq}}$) yields small J_{plate} even in zones with high k_m . The strongest plate-out footprints therefore tend to occur just downstream of high-source regions and along surfaces adjacent to coherent high- μ_t corridors that feed the wall with species-rich fluid. In contrast, recirculation pockets that are strongly cooled or redox buffered can exhibit suppressed deposition despite proximity to the source.

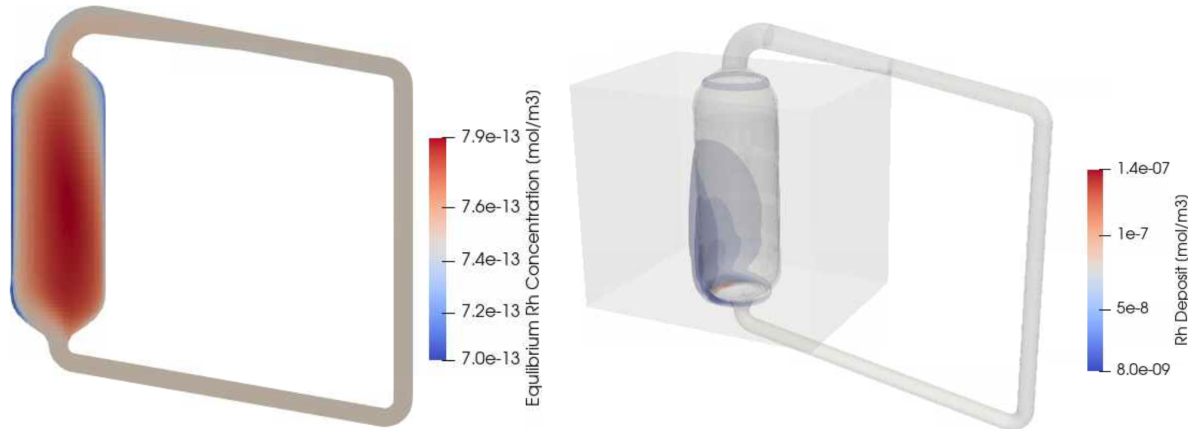


Figure 5-17. Example of noble metal plating results after 100,000 seconds of operation. Left: equilibrium dissolved rhodium concentration in the fuel salt. Right: rhodium concentration at the solid-liquid interface due to plating.

Together, Figure 5-16 and Figure 5-17 extend the steady-state analysis from purely thermal-hydraulic and neutronic consistency to the thermochemical dimension. The redox proxy and dissolution index establish where corrosion driving forces are strongest, while the noble-metal deposition and concentration fields identify how transport pathways convert those driving forces into material loss or plate-out. These views complete the steady-state baseline needed to initialize and interpret the thermochemistry-coupled transients discussed later.

5.3.4. Unprotected Pump-Driven Transients

This section analyzes pump-driven transients in the L-MSR using the fully coupled Griffin-Pronghorn model. Two scenarios are addressed: a full pump stop (initial stages and longer-term evolution) and a 50% pump power reduction (short-term and longer-term responses). The discussion follows the ordering of Figures 32–35.

5.3.4.1. Full Pump Stop — Figures 32 (Initial) and 33 (Longer-Term)

Immediately after the pump is tripped, active head addition collapses and the loop transitions through a mechanical coastdown to buoyancy-driven circulation. In the initial stages (Figure 5-18), the mass flow rate decays rapidly from its nominal value as the hydrodynamic torque and friction overcome rotor inertia. The core outlet temperature rises as convective removal weakens; the inlet temperature lags due to thermal capacitance in the loop and reflector. The core temperature rise produces negative reactivity via Doppler broadening and density feedbacks, biasing the neutron kinetics toward a net reduction in power. Concurrently, delayed-neutron-precursor (DNP) inventories shift: longer in-core residence increases the fraction of decays within the active region, effectively increasing the delayed contribution and lengthening the system's effective generation time. These two effects—negative thermal feedback and increased delayed hold-up—act together to moderate the power evolution during coastdown.

Streamline topology reorganizes as the pump head disappears. Recirculation near inlets strengthens temporarily, while high-shear corridors collapse. The near-wall heat-flux footprint shifts accordingly: areas previously cooled by high-throughput streams experience steeper local temperature gradients, whereas formerly stagnant corners see modest relief as buoyancy redistributes flow. The reflector temperature responds with a lag set by its thermal diffusivity, which spreads and attenuates transient wall heating. No flow reversal is observed under the modeled conditions; pressure differentials remain monotonic as the net head transitions from pump-dominated to buoyancy-dominated.

Over the longer term (Figure 5-19), the system approaches a natural-circulation (NC) equilibrium characterized by a lower, steady mass flow and a larger core temperature rise (ΔT) than in forced circulation. The outlet temperature peaks and then relaxes as increased wall and reflector heat capacity engagement and enhanced radiation/conduction to structures temper the rise. The neutronic power settles below nominal, bounded by the negative temperature coefficients and the sustained in-core DNP fraction under NC. Spatial fields (temperature, density, μ_t , y^+) smooth out as transient shear layers decay; the NC loop establishes stable ascending hot plumes and descending cooler return paths consistent with the Re–Gr–Pr regime of the geometry. The final NC state provides a conservative baseline for decay-heat removal and subsequent perturbations.

Suggested quantitative summaries to report with Figure 5-18–Figure 5-19 include: (i) time constants t_{63} and t_{95} for flow, outlet temperature, and power; (ii) peak outlet temperature and peak wall heat flux with their timestamps; (iii) integral energy balance checks; (iv) DNP inventories in core vs loop volumes and the transient effective delayed fraction; and (v) a comparison between the final NC mass flow and a one-dimensional NC estimate based on loop buoyancy head and calibrated friction losses.

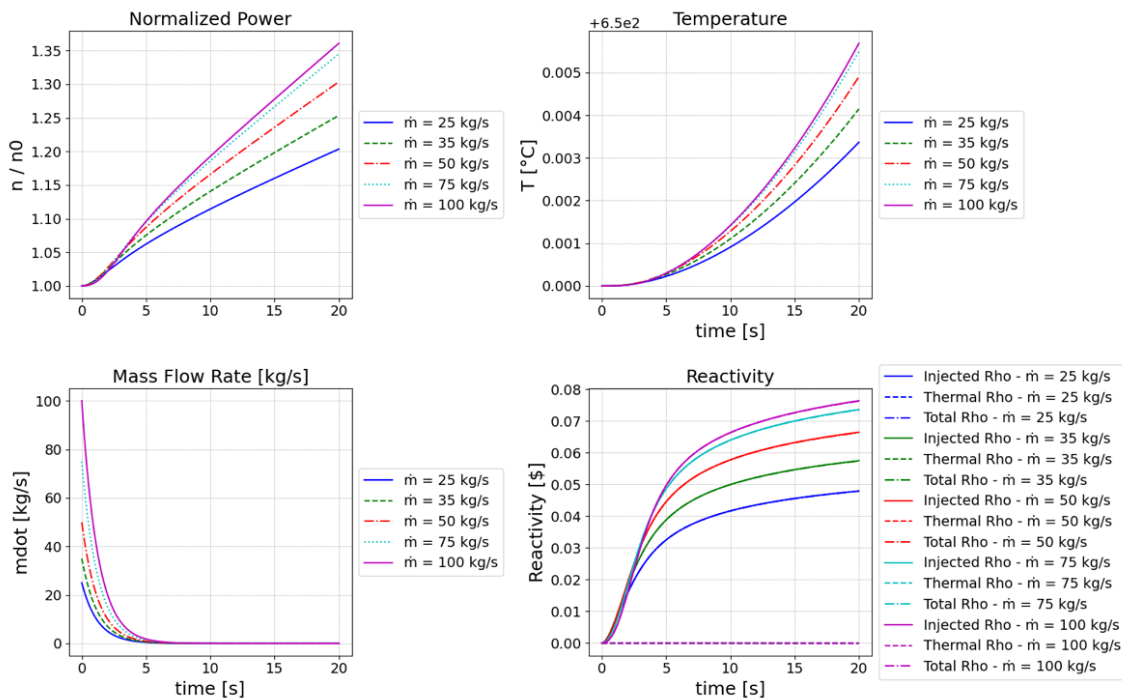


Figure 5-18. Initial stages of full pump stop transient.

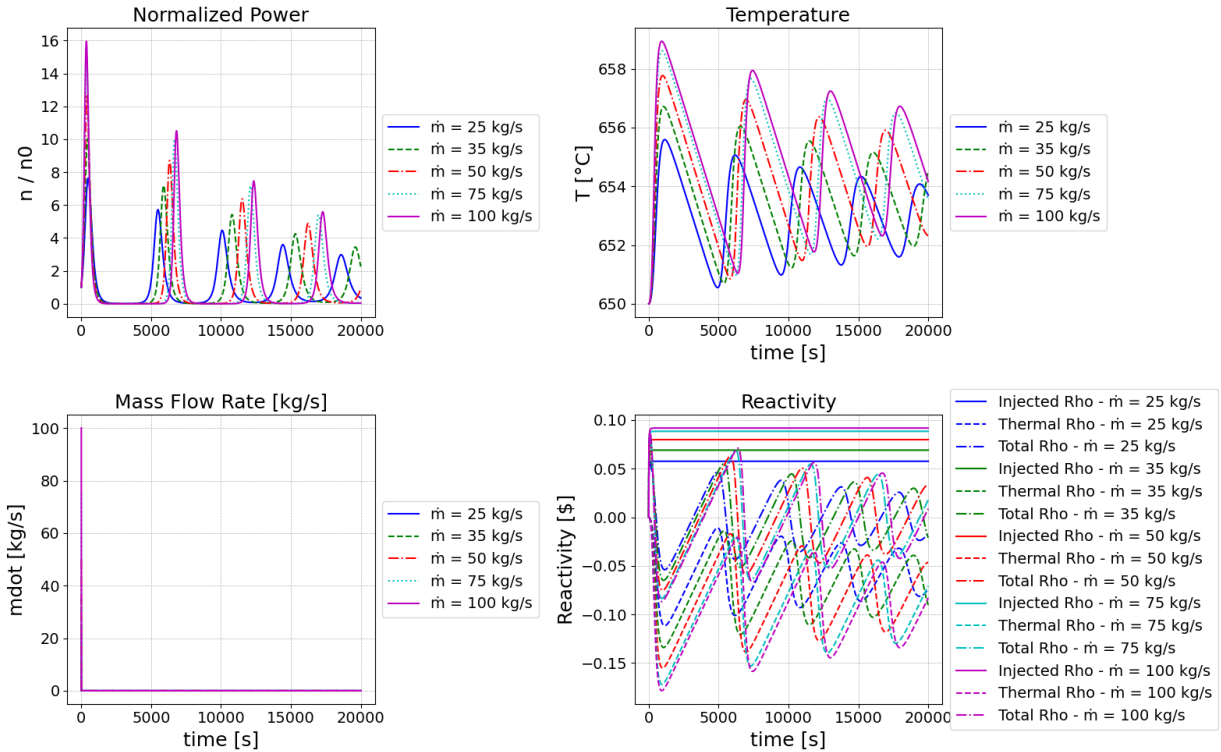


Figure 5-19. Longer-term evolution under full pump-stop transient.

5.3.4.2. 50% Pump Power Reduction — Figures 34 (Short-Term) and 35 (Longer-Term)

A programmed reduction to 50% pump power reduces head and flow without eliminating forced circulation. In the short term (Figure 5-20), the mass flow rate tracks the new pump head with minimal overshoot when the pump curve is well matched to the system resistance. Reduced throughput increases the core thermal rise, elevating the outlet temperature while the inlet temperature adjusts more gradually. The immediate neutronic response follows the thermal evolution: as the salt warms and expands, Doppler and density feedback introduce negative reactivity, resulting in a modest decrease in power when unconstrained, or corresponding control action if power-hold is active. DNP transport simultaneously shifts toward longer in-core residence, increasing the fraction of delayed decays within the core and slightly reducing promptness. Together, these effects produce a smooth, aperiodic approach to a new operating point.

On longer time scales (Figure 5-21), the system settles into a quasi-steady forced-circulation state at half pump power. The final mass flow is reduced relative to nominal, with a correspondingly larger ΔT across the core and slightly elevated wall and reflector temperatures compared to the baseline. Turbulence surrogates (e.g., k and ϵ or ω) and derived transport coefficients (μ_t , D_t , k_t) decrease in magnitude throughout the bulk, which modestly reduces scalar mixing and can increase thermal stratification. Near-wall y^+ values adjust in line with the lower shear; if wall functions are used, the distribution should remain within the model's recommended band to preserve heat-transfer accuracy. The power level stabilizes below nominal due to persistent negative temperature feedback; if a power controller maintains setpoint, the required reactivity insertion is small and well within anticipated control authority.

Recommended reporting with Figure 5-20-Figure 5-21 includes: (i) flow and head histories with the final-to-initial ratio; (ii) changes in outlet temperature, wall heat-flux statistics, and reflector temperature; (iii) the transient and final effective delayed fraction and group-wise DNP inventories; and (iv) recovered effective Nusselt numbers and turbulent transport multipliers relative to the nominal case. These metrics quantify how the 50% pump power reduction rebalances hydraulic, thermal, and kinetic timescales while maintaining comfortable margins.

Across both scenarios, the coupled results show hydraulically driven short-term responses, thermally dominated intermediate behavior, and stabilizing neutronic feedbacks. The full pump stop transitions to a robust natural-circulation regime with conservative heat removal, while the 50% pump power reduction yields a controlled downshift in flow, mixing, and wall loading with predictable shifts in DNP hold-up and temperature-coefficient reactivity. These findings establish validated envelopes for flow-loss events and inform controller design and thermal margin allocations.

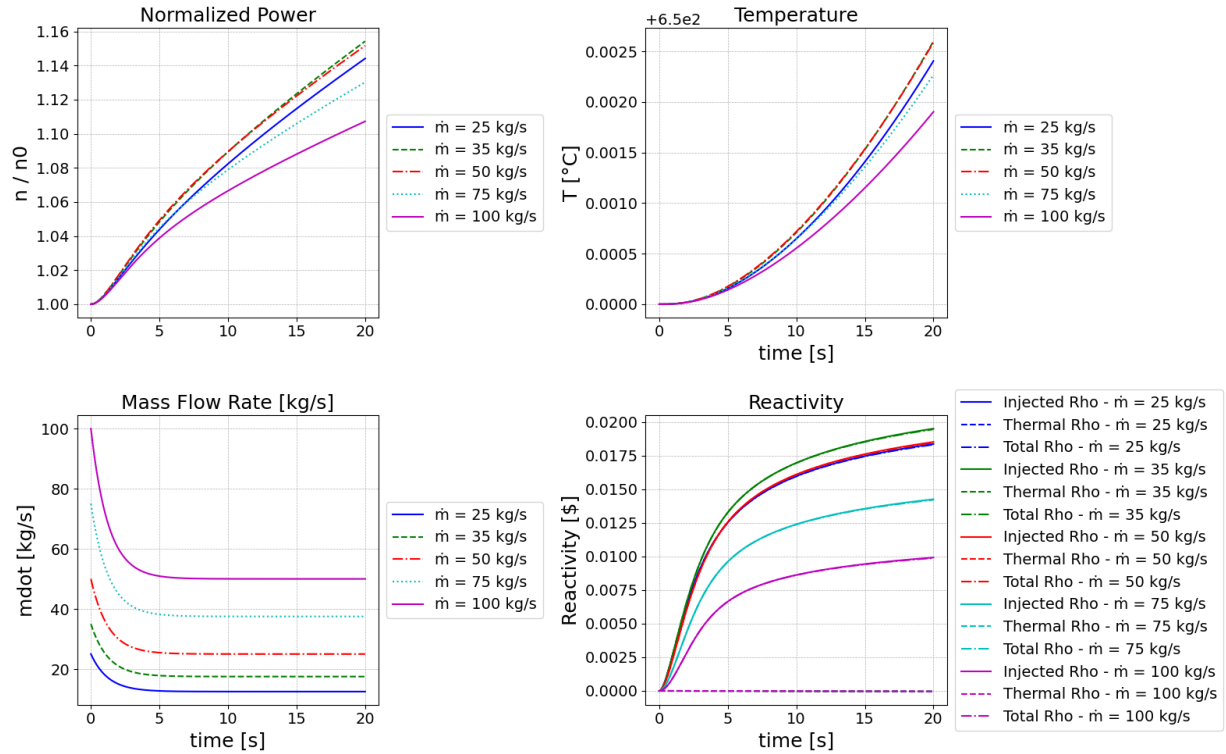


Figure 5-20. Short-term for pump power reduction to 50%.

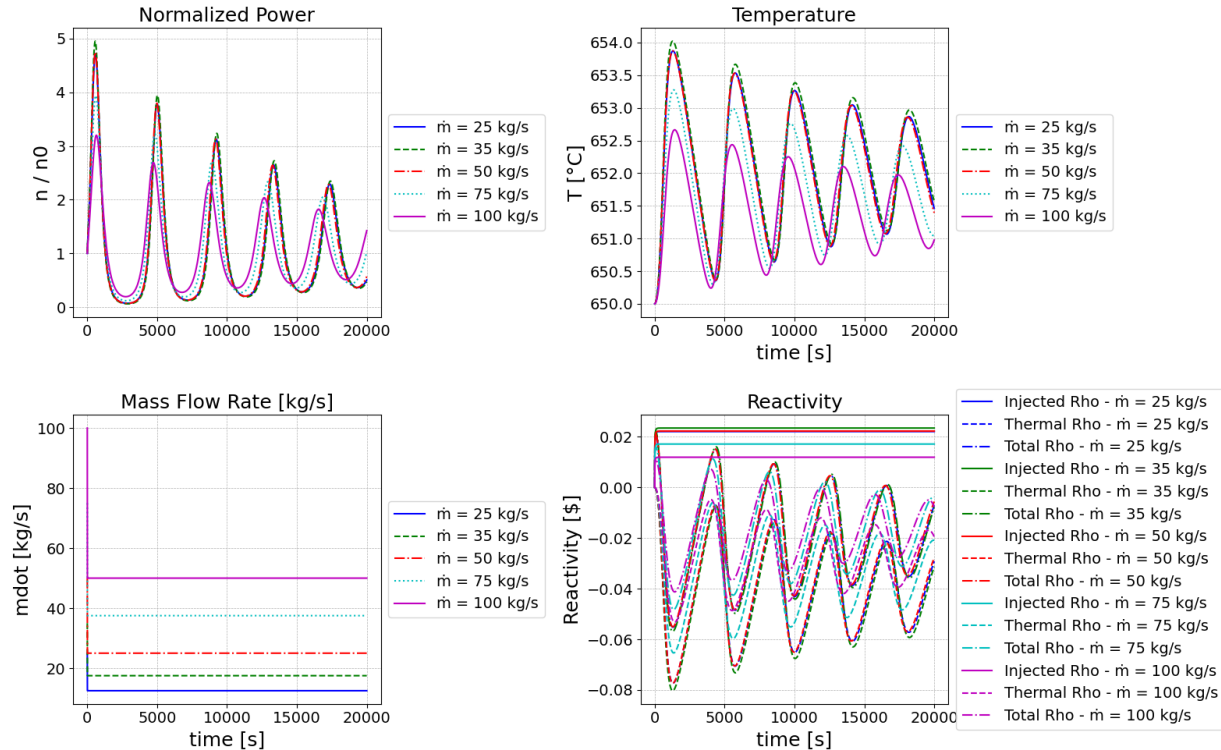


Figure 5-21. Long-term for pump power reduction to 50%.

5.3.5. Natural Circulation Operation

The scenario examined involves natural convection within the L-MSR prototype. This analysis simulates the transition to natural convection following the activation of the reactor shutdown system. Immediately after shutdown, reactor power is assumed to decrease instantaneously to 7% of its nominal thermal power. The spatial power distribution is derived using the neutron diffusion equation and is illustrated in Figure 5-22.

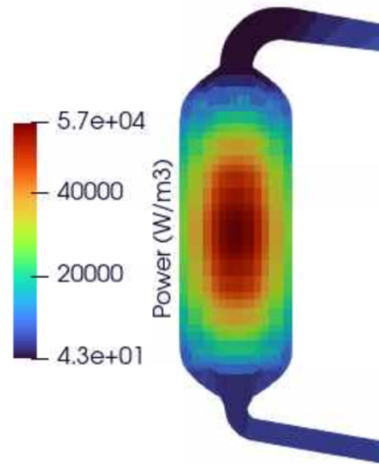


Figure 5-22. Decay power distribution in the L-MSR immediately after the shutdown.

A Dirichlet boundary condition of 850 K is applied at the external reactor core wall, which interfaces with the reflector. The L-MSR lacks heat exchangers and dissipates generated heat through radiation via the reflector walls while cooling the cavity containing the reactor core. This setup justifies the chosen boundary condition modeling approach.

A segregated transient solver utilizing the PIMPLE algorithm is employed. No-slip boundary conditions are applied to all reactor walls. Decay heat is modeled as a volumetric heat source within the core. The constant thermophysical properties used in this analysis are detailed in Table 5-7. The fuel salt density is defined as:

$$\rho(T) = \rho_0(1 - 3.26e^{-4}(T - 875)), \quad 5.6$$

The dynamic viscosity used in this study does not represent the actual value for the chloride salt intended for use in the MCRE. Instead, a chosen viscosity value facilitates the study of natural convection without requiring turbulence modeling. Future work will address the accurate representation of chloride salt viscosity and include turbulence modeling for natural convection. The computational mesh comprises approximately 26,000 hexahedral elements, with further details provided in ([Freile et al., 2025](#)).

Table 5-7. Thermophysical properties used for the natural convection case of the MCRE-prototype. Viscosity values do not correspond to the actual chloride salt.

Parameter	Value
Reference density [kg/m ³]	3279
Dynamic viscosity [Pa.s]	5.926
Specific Heat [J/kgK]	640
Thermal Conductivity [W/mK]	0.38

Natural convection in the L-MSR was simulated using Star-CCM+ (reference CFD code), employing identical computational domains and thermophysical properties. An implicit unsteady solver was utilized in the reference CFD code. The vertical velocity field distributions were compared with those obtained from Pronghorn, using the new boundary formulation at various transient stages for code-to-code comparison. Figure 5-23 shows the results for both Star-CCM+ and Pronghorn at 900 seconds and 1500 seconds after the transient initiation.

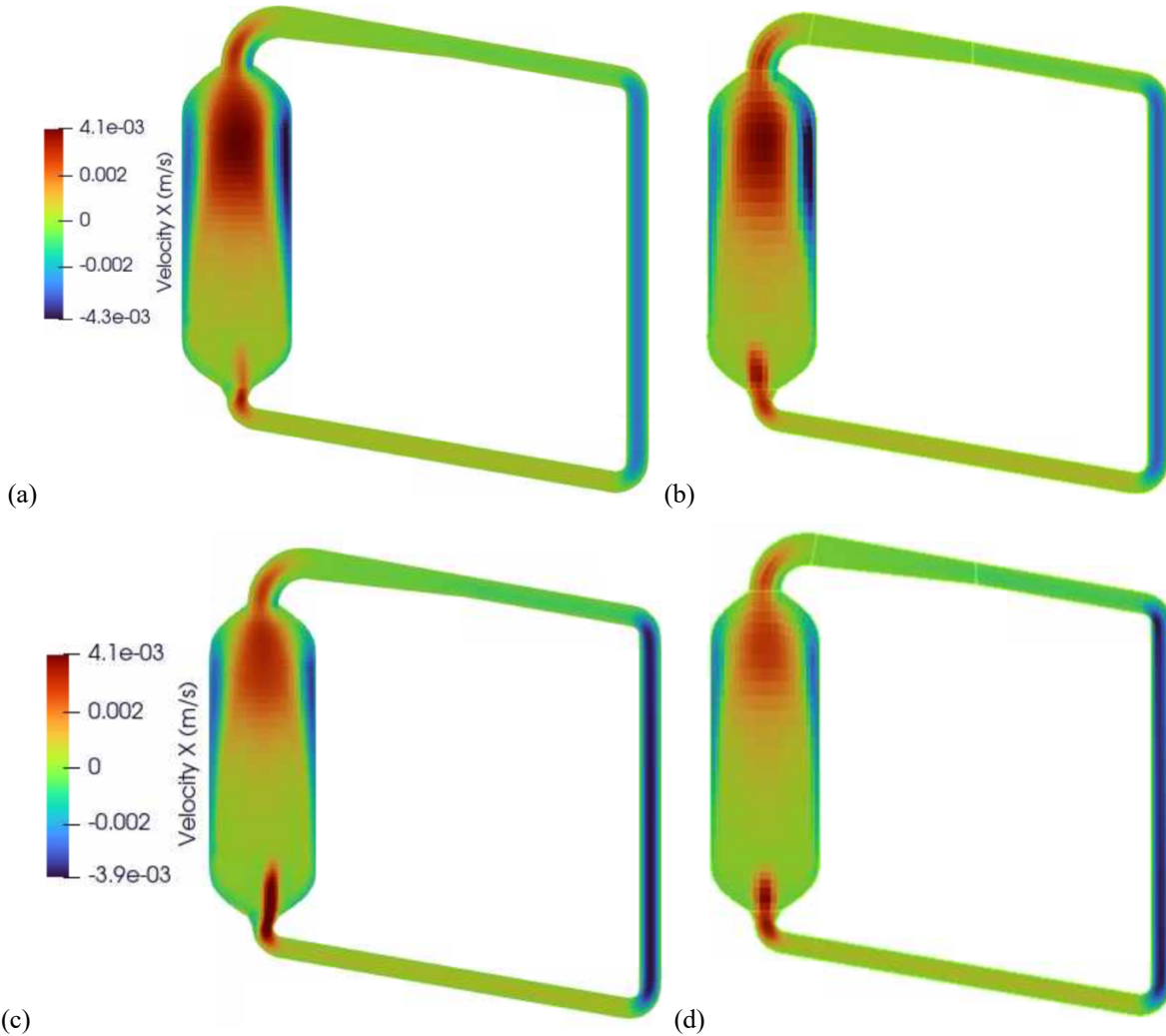


Figure 5-23. (a) PH at 900s. (b) Reference CFD at 900s. (c) PH at 1500s. (d) CFD at 1500s. Natural convection vertical velocity qualitative comparison between the Pronghorn and a reference CFD code for a decay-like heat power in MCRE at different stages of the transient.

During this transient, the salt within the reactor is heated in the core region. Due to density changes, the hotter salt rises from the core towards the top of the domain, while the colder salt descends towards the bottom. The salt ascends through the center of the core and descends along the reactor-reflector interface walls, cooling as it does so. As the transient advances, the temperature of the salt results in a stratified distribution. Figure 5-23 illustrates the final stratified temperature distribution. The final temperature values are conservative, based on the assumption of a constant 7% decay power. These values also assume the cooling system responsible for maintaining the cold sink at the reflector cavity operates continuously throughout the transient.

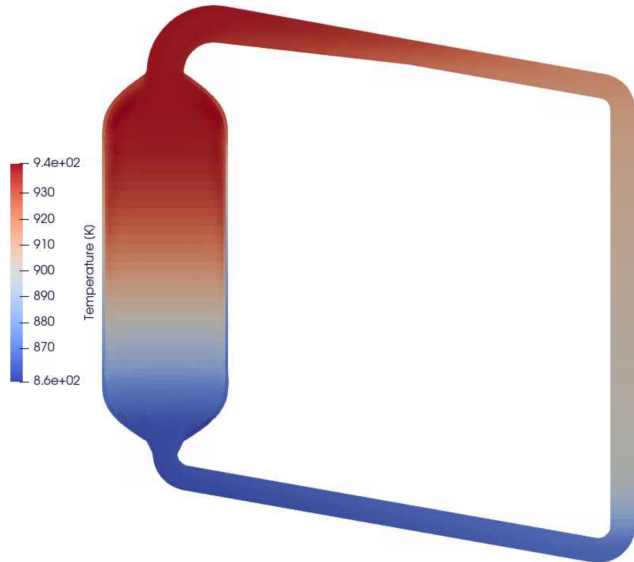


Figure 5-24. Final temperature distribution.

Figures Figure 5-23a and Figure 5-23b indicate that at 900 seconds, the velocity magnitude is greater than at 1500 seconds (Figure 5-23c and Figure 5-23d). This is due to the higher temperature gradient caused by a less uniform temperature distribution. As the transient progresses, the temperature fields become more uniform, reducing the buoyant head and resulting in decreased velocity magnitudes in the later stages. This qualitative comparison demonstrates good agreement between the reference CFD code and Pronghorn using the new pressure flux boundary condition formulation at both stages of the transient.

5.3.6. Flow Stop with Long-Term Salt Solidification and Re-Melting

This section examines salt solidification and subsequent re-melting during negative reactivity insertion events, with attention to both short-term and longer-term behavior. The transients begin from the coupled steady state and include step insertions corresponding to one, two, three, and four control elements. For each insertion magnitude, we discuss a short-term window in which thermal-hydraulic and neutronic variables reorganize rapidly, followed by a longer-term window where thermal inertia and feedbacks determine whether solidified regions persist or re-melt. The analysis integrates the space–time evolution of salt temperature, density, and mixing with the kinetics response (reactivity, power) and tracks the onset and retreat of solidification near cold structures.

Physically, negative reactivity insertion reduces fission power and, after a short delay set by thermal capacities and flow residence, lowers the bulk salt temperature. Cooling near high-conductivity solids and inflow paths can drop the local temperature toward or below the salt’s liquidus, producing incipient solidification at walls, corners, and in low-mixing pockets. As temperatures fall, the negative temperature coefficient introduces positive reactivity—a stabilizing feedback that partially restores power. Depending on the insertion depth, this feedback and decay heat can either re-melt the nascent solid regions or allow a quasi-steady frozen lens to persist until heat input rises.

5.3.6.1. One Control Element (≈ -700 pcm) Insertion: Short- and Long-Term

Following insertion of approximately -700 pcm, core power promptly depresses and the outlet temperature begins to fall. The near-wall regions adjacent to the reflector and entrance/exit features cool first; weakly mixed pockets register the earliest proximity to the liquidus. The kinetics response is

dominated by negative Doppler and density feedback during the initial cooldown, followed by a gradual partial reactivity recovery as temperatures decline (negative temperature coefficient). In the longer term, the net power settles modestly below nominal, the bulk temperature stabilizes above the liquidus, and any small, wall-adjacent solid fractions re-melt as diffusive heat from the core interior and positive feedback offset the initial cooling. The salt resumes fully liquid operation with no persistent blockage in in-core passages.

Diagnostics to report with the figure include: the minimum salt temperature and its location; time to minimum; the volume and surface area of any transient solid fraction; the time to complete re-melting; and a reactivity breakdown showing the transient positive offset arising from cooling feedback. These confirm that a -700 pcm insertion remains within reversible margins for thermal recovery.

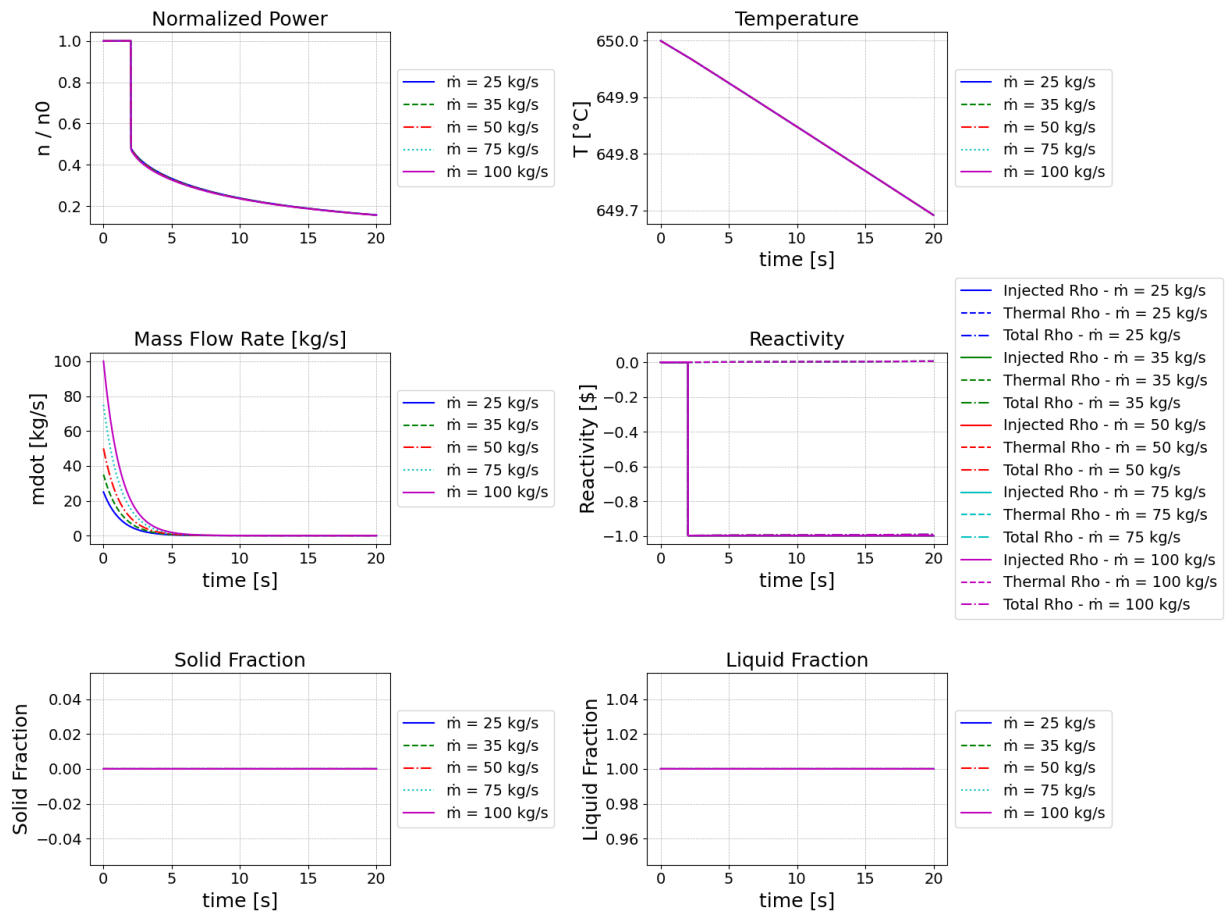


Figure 5-25. Short term evolution after a flow stop and a control rod insertion of one control element at 2 seconds. The injected reactivity is approximately -700 pcm.

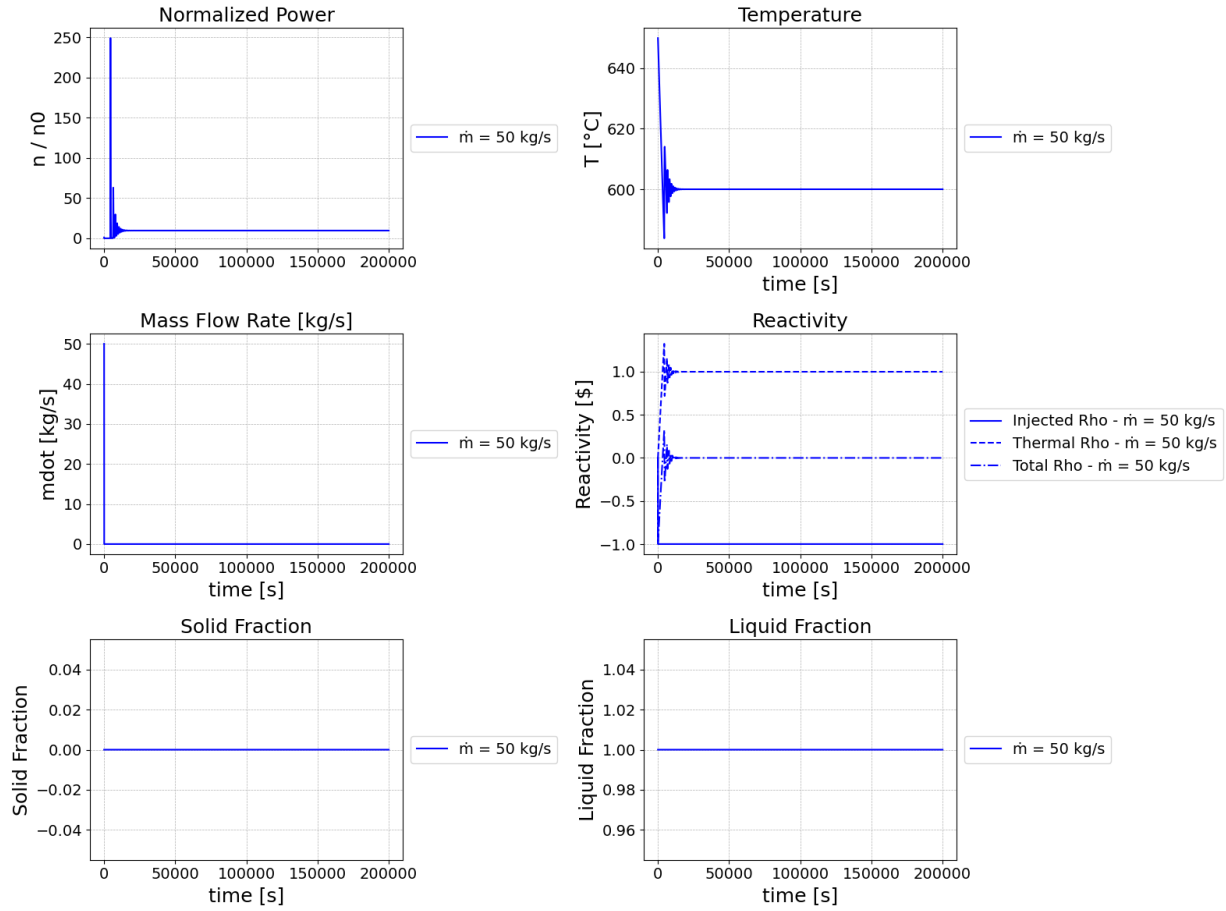


Figure 5-26. Long-term evolution of the reactor physics and thermophysical properties showcasing a reactivity insertion of one control element equating to approximately -700 pcm. We showcase only the case with 50 kg/s of mass flow rate since the long-term evolution for the other cases is very similar.

5.3.6.2. Two Control Elements ($\approx -1,400$ pcm): Short- and Long-Term

A $-1,400$ pcm step deepens the power depression and cools the salt more strongly than the one-element case. In the short term, the cooling front propagates from high-conductivity structures into the nearby salt, and small frozen patches can nucleate at the sharpest corners and in recirculation saddles where advection is weakest. The power minimum occurs before the temperature minimum due to finite thermal inertia; thereafter the negative temperature coefficient provides partial reactivity recovery, moderating the descent.

On the longer-term horizon, the system converges to a cooler, lower-power equilibrium than the one-element case. Whether all solid patches re-melt depends on the local balance between heat supplied from warmer core volumes and heat removed into surrounding structures. In typical operating margins, the frozen area contracts over time and re-melts completely as the feedback-restored power and spatial heat diffusion raise wall-adjacent temperatures. The mass-flow setting has a second-order influence on this long-term picture once the temperature field becomes diffusion-dominated; accordingly, the representative long-term figure emphasizes one flow case while noting that other flow conditions exhibit similar qualitative evolution.

Recommended metrics include the transient fraction of wetted perimeter experiencing $T < T_\ell$, the maximum solid thickness at peak cooling, the time integral of latent-heat release/absorption (as a proxy for solid mass formed and re-melted), and the evolution of group-wise delayed-neutron precursor inventories to verify that kinetics remain delayed-dominated throughout.

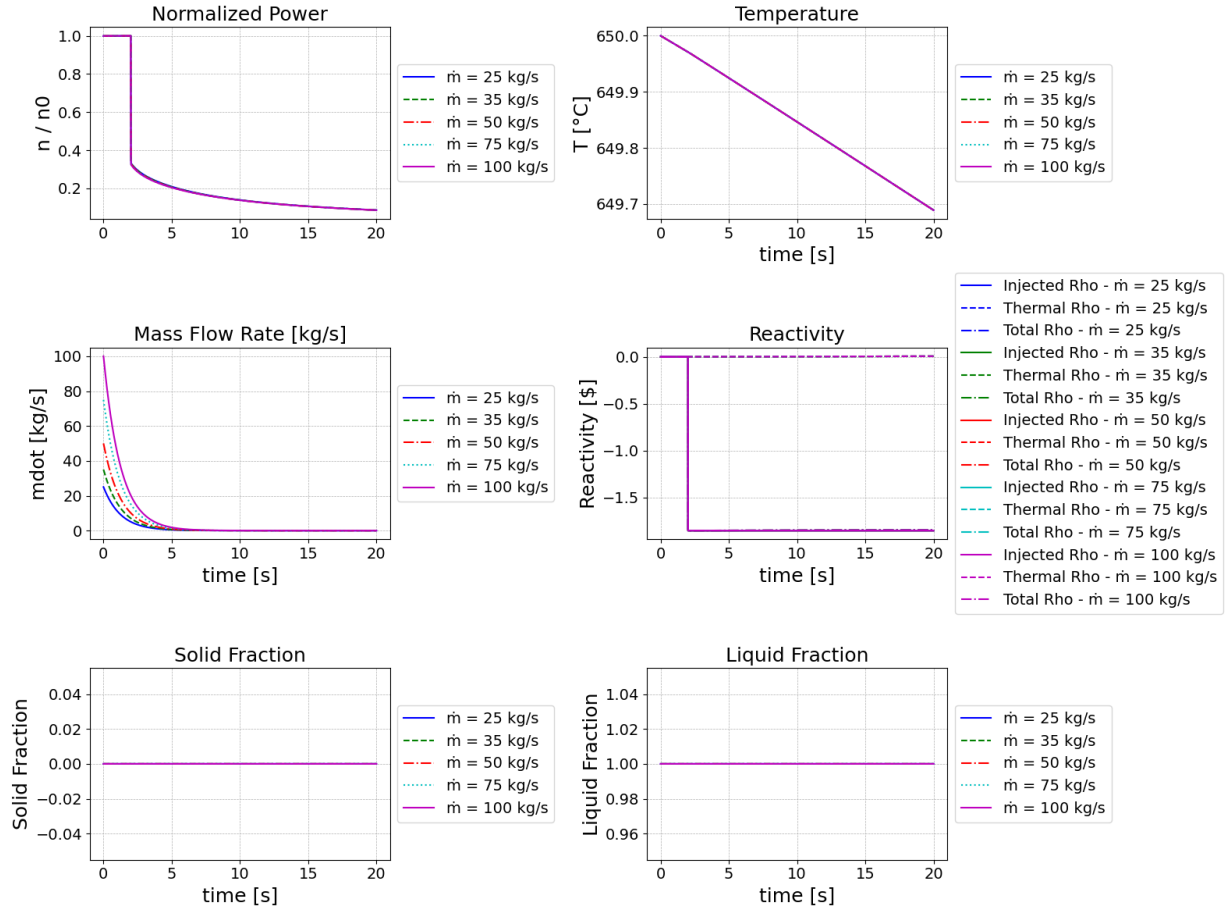


Figure 5-27. Short term evolution after a flow stop and a control rod insertion of two control elements at 2 seconds. The injected reactivity is approximately -1,400 pcm.

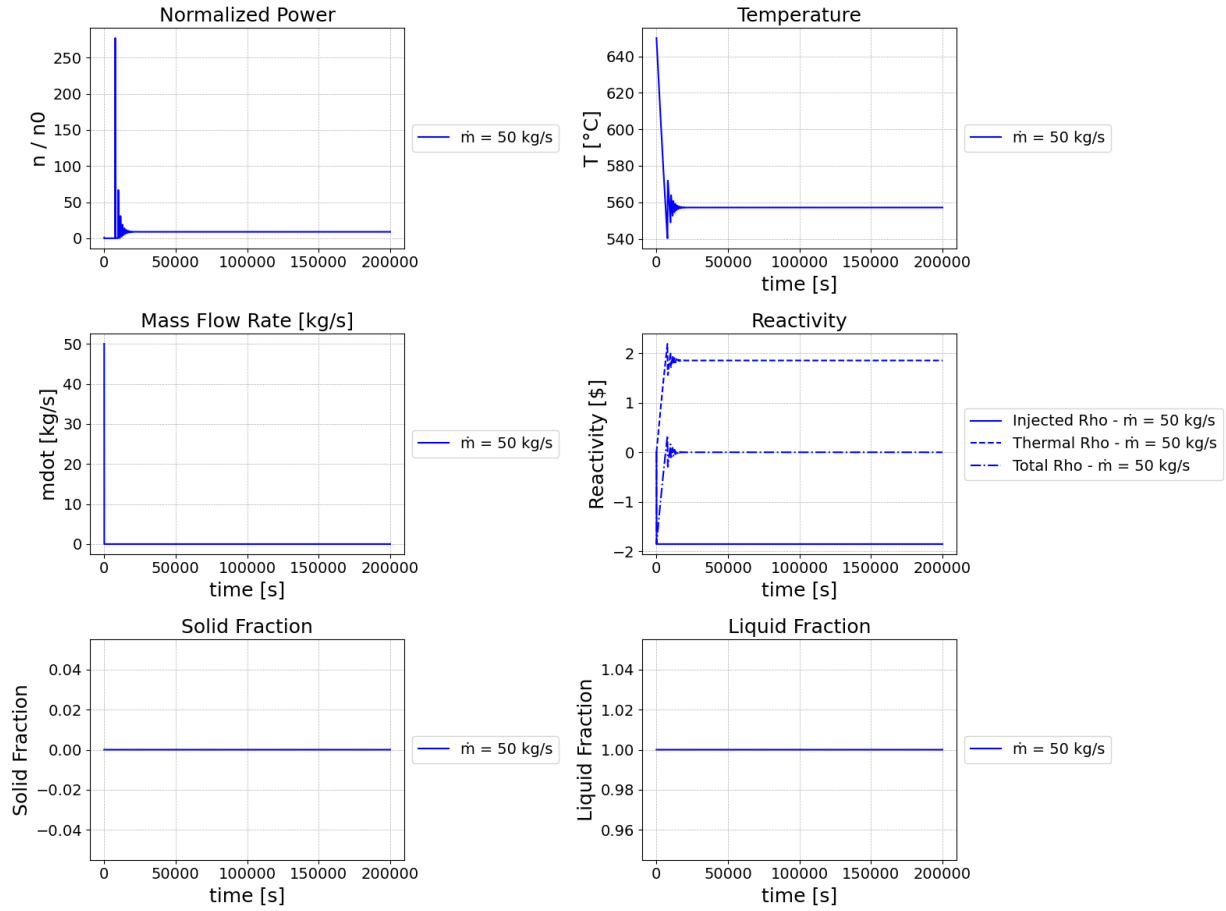


Figure 5-28. Long-term evolution of the reactor physics and thermophysical properties showcasing a reactivity insertion of two control elements equating to approximately $-1,400 \text{ pcm}$. We showcase only the case with 50 kg/s of mass flow rate since the long-term evolution for the other cases is very similar.

5.3.6.3. Three Control Elements ($\approx -2,100 \text{ pcm}$): Short- and Long-Term

At approximately $-2,100 \text{ pcm}$, the short-term response exhibits stronger cooling rates and wider regions flirting with the liquidus in the immediate vicinity of cold structures. The earliest solidification still appears at geometric stagnation features and along surfaces with sparse streamline coverage. Because power has been reduced more substantially, the reactivity recovery from the negative temperature coefficient is more pronounced in absolute value but occurs from a lower baseline, so the net power remains well below nominal for an extended interval.

Over longer times, two outcomes are observed depending on local heat-leak pathways: (i) complete re-melting as diffusive heat inflow from the core interior and feedback-restored fission power raise wall temperatures; or (ii) a quasi-steady, thin frozen lens that persists at select cold spots with weak thermal coupling to the hot interior. In either case, the frozen regions do not occlude primary flow passages in the modeled geometry, and the core remains hydraulically connected. Documenting the minimum temperature margin to the liquidus, the persistence time of any frozen lens, and the sensitivity to assumed thermal contact and emissivity values is recommended for this case.

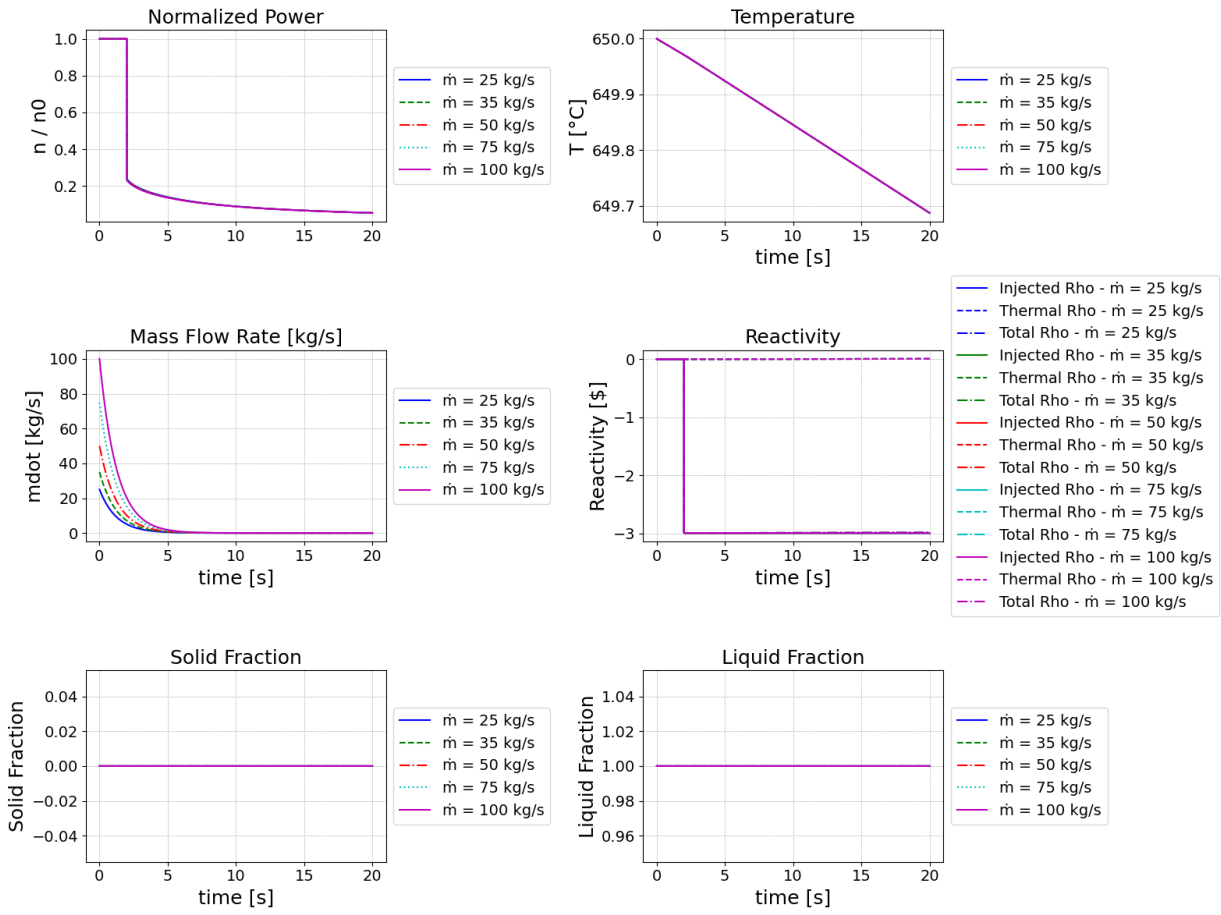


Figure 5-29. Short term evolution after a flow stop and a control rod insertion of three control elements at 2 seconds. The injected reactivity is approximately -2,100 pcm.

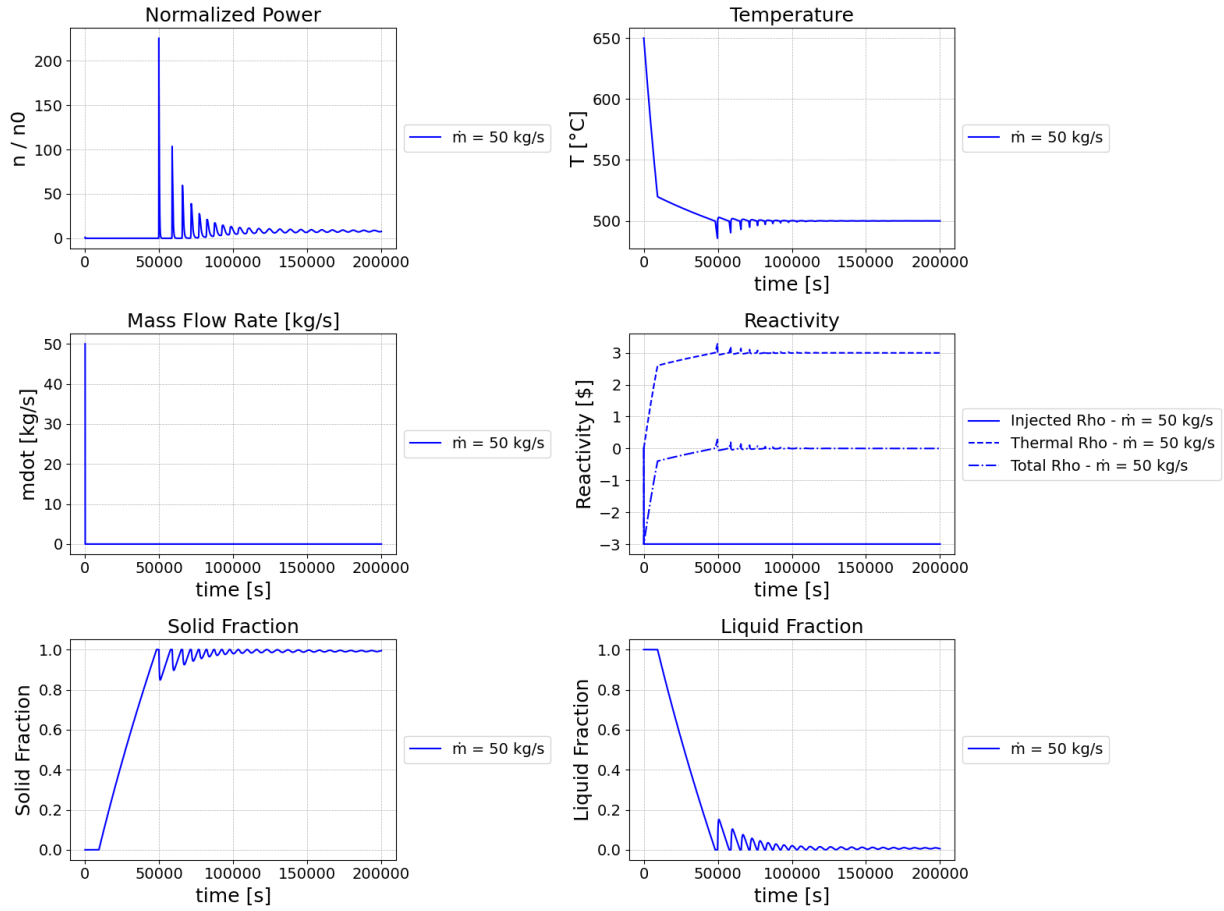


Figure 5-30. Long-term evolution of the reactor physics and thermophysical properties showcasing a reactivity insertion of three control elements equating to approximately $-2,100 \text{ pcm}$. We showcase only the case with 50 kg/s of mass flow rate since the long-term evolution for the other cases is very similar.

5.3.6.4. All Four Control Elements ($\approx -2,800 \text{ pcm}$): Short- and Long-Term

The $-2,800 \text{ pcm}$ scenario represents the most severe negative insertion considered. Short-term behavior shows the steepest power collapse and the fastest cooling near walls, increasing the areal extent of surfaces that momentarily dip below the liquidus. Thin, patchy frozen layers may form along the coldest reflector interfaces and at inlet and outlet features. The kinetics remain stable due to strong negative Doppler and density feedback that are amplified by the rapid temperature drop; nevertheless, overall power remains significantly depressed relative to nominal.

In the longer term, two competing mechanisms set the fate of solidified regions: rising reactivity from continued cooling, which gently elevates power, and thermal diffusion from the warmer core interior toward walls. In combination, these generally shrink the frozen area and, for the representative mass-flow condition, lead to gradual re-melting without loss of hydraulic connectivity. The final equilibrium features a cooler core with a larger ΔT to structures than at nominal conditions but a fully liquid salt phase. Reporting maximum frozen area fraction, latest time to complete re-melting, and peak wall thermal gradients helps establish engineering margins for this bounding case.

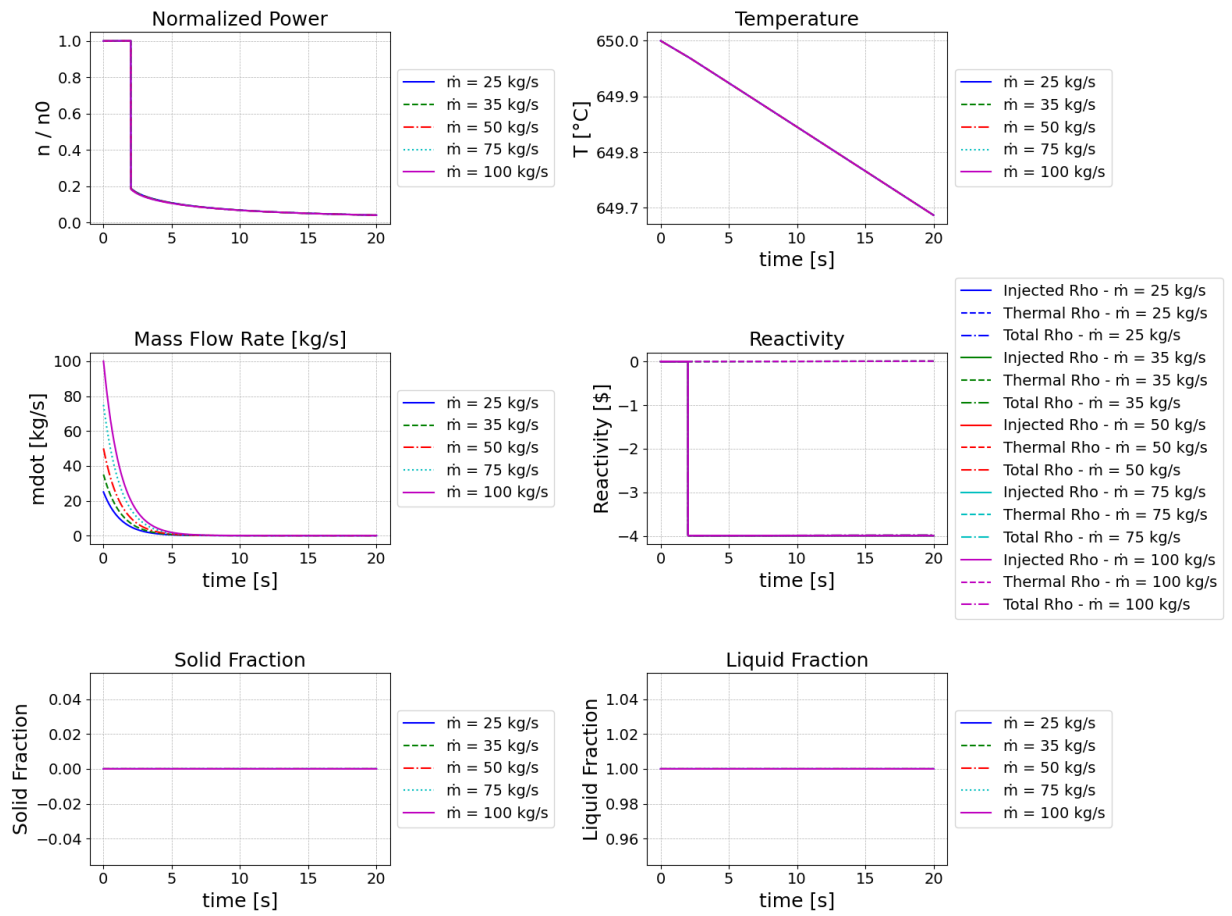


Figure 5-31. Short term evolution after a flow stop and a control rod insertion of all four control elements at 2 seconds. The injected reactivity is approximately -2,800 pcm.

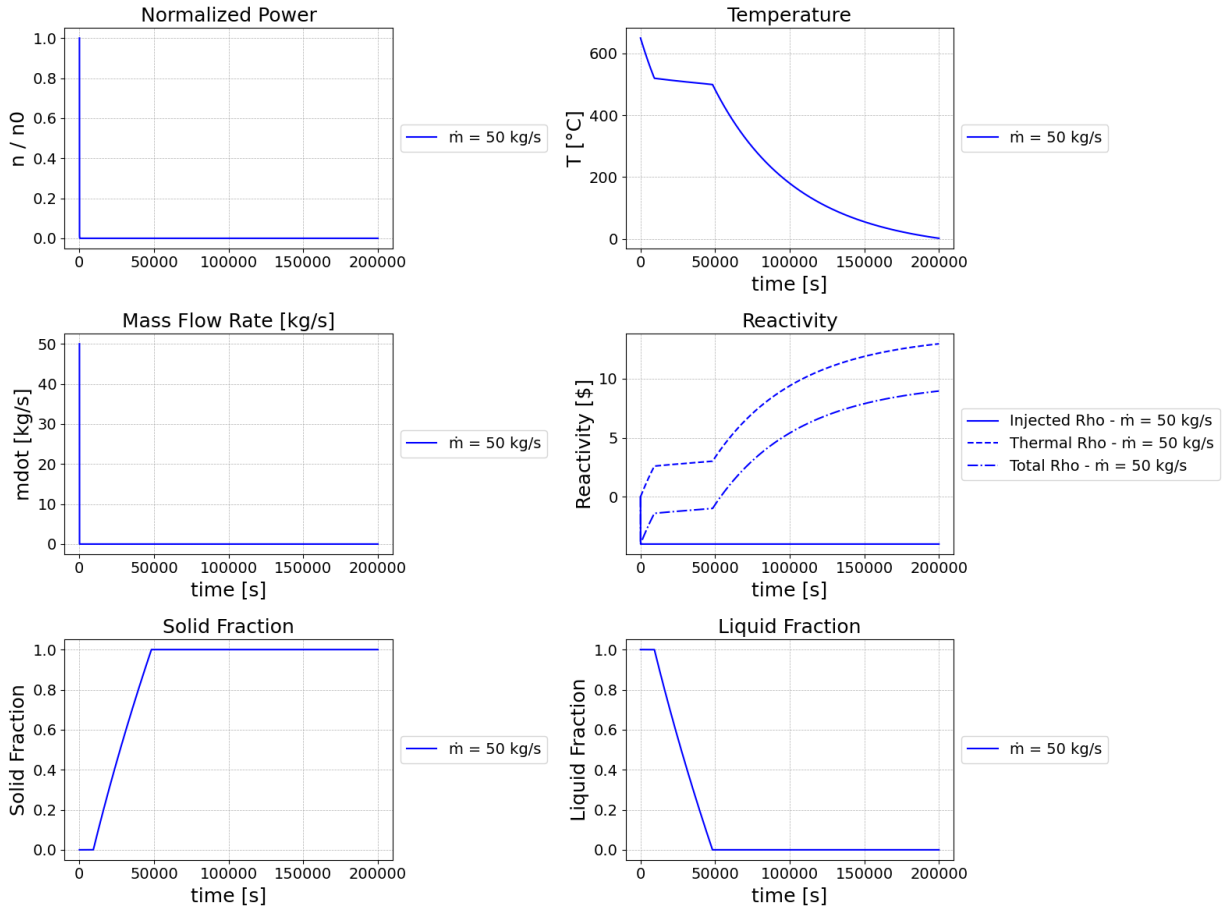


Figure 5-32. Long-term evolution of the reactor physics and thermophysical properties showcasing a reactivity insertion of two control elements equating to approximately $-2,800 \text{ pcm}$. We showcase only the case with 50 kg/s of mass flow rate since the long-term evolution for the other cases is very similar.

Across the suite of insertions, three robust patterns emerge. First, the location of first solidification is set by the interplay between structural heat sinking and local mixing—surfaces with high conductivity and sparse streamline coverage are most susceptible. Second, the negative temperature coefficient provides self-limiting feedback: deeper insertions cool more, which returns positive reactivity and arrests further cooling. Third, the long-term fate of solidification hinges on diffusive heat redistribution; once the transient advection patterns subside, temperature gradients relax and solid lenses either re-melt or equilibrate as very thin, localized features with negligible hydraulic impact.

For traceability, we recommend including with the figures: (i) time histories of power, reactivity components (Doppler, density), outlet and selected wall temperatures; (ii) maps of minimum attained temperature and time-of-first solidification; (iii) solid-fraction volume vs time and cumulative latent-heat integrals; and (iv) sensitivity sweeps of key properties (thermal conductivity of structures, salt heat capacity, assumed liquidus) to bracket uncertainty. These provide quantitative anchors to the qualitative trends and support design decisions for freeze plugs, cold traps, and wall temperature limits.

6. Conclusions and Future Work

6.1. Conclusions and Future Work for MSRE Integral Modeling

The preliminary results of this study underscore the efficacy of the initial multiphysics capability developed for MSRE. The coupled Griffin-Pronghorn model has demonstrated significant accuracy in both steady-state and transient scenarios, validated against historical data from the MSRE. The models were able to capture crucial reactor behaviors such as temperature feedback, reactivity losses, and delayed neutron precursor advection. The addition of void transport modeling further refined the accuracy of reactivity predictions during pump start-up transients. The natural circulation test results showed that the models could accurately simulate the reactor's power and temperature evolution even in the absence of active pumping. Furthermore, the Griffin-depletion calculations effectively replicated the changes in the redox potential of the fuel salt, although some biases were observed in the latter stages of reactor operation. These findings indicate that the current modeling approach is robust and reliable for simulating the behavior of MSRs under various conditions.

To enhance the accuracy and efficiency of future MSR simulations, several recommendations can be made. Firstly, it is crucial to incorporate void transport modeling in all future transient analyses of MSRs. This will improve the accuracy of reactivity predictions, particularly during pump start-up conditions, which are critical for ensuring reactor stability. Secondly, the Squirrel tool can be used for point kinetics modeling in scenarios where computational efficiency is a priority. Squirrel has shown sufficient accuracy in transient simulations, making it a valuable tool for rapid calculations. Thirdly, the use of active chemistry control for managing the redox potential of fuel salts should be continued. It is essential to ensure that the models account for the addition of reducing metals to maintain the desired UF₄ to UF₃ ratio. Additionally, further validation of the coupled Griffin-Pronghorn model against a broader range of experimental data is recommended to ensure its robustness across various operating conditions and reactor designs. Lastly, improving the current corrosion product modeling by developing and integrating a sophisticated alloy model within Thermochemica will better capture the thermochemical equilibrium between the fuel salt and structural materials.

The future work in the domain of MSR modeling and simulation should focus on several key areas to further enhance the understanding and predictive capabilities of these reactors. One area of exploration is the development of advanced void transport models. More sophisticated models are needed to capture the dynamic behavior of gas-liquid interactions in MSRs, particularly under varying operational conditions. Additionally, expanding the current 2-D R-Z model to a full 3-D simulation is a crucial step forward. This expansion will allow for a more detailed capture of spatial variations in reactor behavior, thereby improving the accuracy of localized predictions.

Further integration of Griffin, Pronghorn, and Squirrel with other advanced codes like GeN-Foam, MCNP, and Serpent is another critical area of future work. This integration will create a comprehensive multiphysics simulation framework for MSRs, enabling more holistic analyses. Conducting detailed sensitivity and uncertainty analyses is also essential. These analyses will help identify and quantify the key parameters that influence the reactor's performance and safety margins.

Material corrosion studies should be a significant focus of future research as well. Experimental and modeling studies on the corrosion behavior of structural materials in MSRs, with a focus on the impact of fuel salt composition and operational parameters on material degradation, will provide valuable insights. Developing dynamic chemistry control strategies that can adapt to real-time changes in reactor conditions will enhance the stability and longevity of the fuel salt.

High-fidelity experimental validation is another area that warrants attention. Collaborating with experimental facilities to obtain high-fidelity data for validating the models under various transient and

steady-state conditions, including newly designed MSR prototypes, will ensure the accuracy and reliability of the models. Studying the long-term behavior of MSRs, including the effects of prolonged operation on fuel salt composition, structural integrity, and overall reactor performance, will provide a comprehensive understanding of the reactor's lifecycle.

Exploring enhanced computational techniques, such as the use of machine learning and artificial intelligence, will optimize the computational efficiency and predictive accuracy of MSR simulations. Engaging with regulatory bodies and the public to communicate the advancements in MSR modeling and safety is also crucial. Addressing any concerns and ensuring transparent and informed decision-making will facilitate the development and deployment of next-generation nuclear reactors.

By addressing these recommendations and pursuing the outlined future work, the modeling and simulation of molten salt reactors will continue to advance, providing critical insights for the development and deployment of next-generation nuclear reactors. This comprehensive approach will ensure that the reactors are not only efficient and reliable but also safe and sustainable for the future.

6.1.1. Summary and Future Work for Xenon Transport

Based on the analyses and calculations discussed in the previous sections, the major findings for the Xenon transport calculations are summarized below:

1. There are significant improvements in the SAM code to simulate the important Xenon transport phenomena such as the mass transfer between the fuel salt and the bubble, as well as the mass transfer between the fuel salt and the graphite.
2. The SAM-Griffin MSRE model is updated with the state-of-the-art capability for Xenon transport calculation. This model is validated against the MSRE experiment. Good agreement is achieved for two cases: one with a high stripping efficiency and a low salt-to-bubble MTC, and the other with a low stripping efficiency and a high salt-to-bubble MTC.
3. Further resolving the stripping efficiency and the salt-to-bubble MTC would require high fidelity calculation or experiments.
4. In general, the SAM-Griffin coupling for Xenon poisoning model is successfully demonstrated and preliminarily validated against the experimental measurements.
5. One feature in SAM that is worth highlighting is the segregated species transport solver (Mui et al. 2024). This solver significantly reduces the amount of computational time on the SAM side without impact on the final results. For a standalone SAM Xenon transport calculation, the computational time is reduced from ~20 hours to ~2 hours.

There are still potential improvements of the modeling and methods needed for the Xenon transport calculation in the MSR primary loop. One subtle point is on the overestimation of the Xenon poisoning at low void fraction. The current SAM salt-to-graphite model seems to overpredict the Xe-135 concentration in the graphite, which results in large reactivity feedback. This seems suggesting the related MTC is too large. In addition, other steady state Xe poisoning experimental data is available for soluble cover gas (Helium). In this case, the cover gas dissolving into the salt need to be considered in the model. Another potential improvement in the model is on the Xe-135 absorption rate transfer. Currently, the Xe-135 absorption rate is specified as a user input that is pre-calculated with OpenMC, which can be calculated by Griffin and transferred to the SAM simulation. This may impact the result under transient when with Xe-135 concentration change and power level change. There is also transient experimental measurement on Xenon poisoning, which can be used to further validate the SAM-Griffin model.

6.2. Future Work for L-MSR Integral Modeling

Also, in this study, we successfully modeled the Lotus Molten Salt Reactor (L-MSR) using the MOOSE framework, based on the open-source specifications of the Molten Chloride Reactor Experiment (MCRE). The work demonstrated the capability of NEAMS tools to model steady-state conditions and various transient scenarios, including loss of flow circulation, over-circulation, overheating, overcooling, and density changes in the fuel salt and reflector. The geometric complexity of the L-MSR model was incrementally increased, starting from a simplified fluid domain and progressively incorporating additional components such as the reflector. The fluid dynamics domain was calibrated to match the reference Large Eddy Simulation (LES) model, ensuring accurate representation of pressure drops and flow rates. The implementation of a proportional-integral (PI) control system facilitated the calibration process, resulting in minimal discrepancies between the MOOSE model and the LES reference.

The results indicated that the majority of the pressure drop occurred at the pump choke, validating the importance of including this component in the model. The velocity field analysis highlighted expected flow patterns and revealed potential areas for improvement, such as boundary layer implementation. The study confirmed that the MOOSE model could maintain stable and consistent conditions during restarts, demonstrating its robustness and reliability.

Future work will focus on several key areas to further enhance the L-MSR model and explore additional scenarios. The next step involves coupling the thermal-hydraulics model with neutronics simulations to capture the complete multiphysics behavior of the L-MSR. This integration will provide a more comprehensive understanding of reactor performance under various operating conditions. Further investigation of more complex transients in the reactor core will be conducted to extend the applicability of NEAMS tools. Scenarios such as rapid reactivity insertions, transient overpower conditions, and emergency shutdowns will be modeled and analyzed.

The absence of boundary layers in the current velocity field analysis suggests potential for improvement. Implementing boundary layers will enhance the accuracy of flow and heat transfer predictions, particularly near solid surfaces. The pump is currently modeled with several assumptions and abstractions. Future work will refine the pump model to reduce uncertainties and improve the accuracy of flow characteristics and pressure drop predictions. Addressing uncertainties in the thermophysical properties of the fuel salt and reflector materials will be crucial. Sensitivity analyses and uncertainty quantification will help identify the impact of these properties on reactor performance.

Finally, where possible, experimental data will be used to validate the simulation results. Collaborations with experimental programs and facilities will provide valuable insights and data for model validation. By addressing these areas, we aim to enhance the fidelity and predictive capability of the L-MSR model, contributing to the advancement of molten salt reactor technologies and their potential deployment in the future.

6.3. Conclusions and Future Work for Depletion Modeling

Based on this exercise, the following recommendations can be considered for future development efforts in Griffin and Shift:

1. Enhancement of Griffin's microscopic depletion capability.
The current microscopic depletion approach in Griffin can simulate liquid-fueled molten salt reactors; however, it lacks essential capabilities for fractional removal of fission products and continuous addition of makeup fuel. To address these gaps, Griffin could incorporate functionality in the microscopic depletion modeling to:
 - a. Handle fractional removal of fission products explicitly.

- b. Allow for multiple distinct waste streams (e.g., separate streams for noble gases and noble metals and others).
 - c. Automatically track the decay and transmutation of isotopes in each waste stream.
- 2. Online cross-section generation in Griffin.
Implementing an online microscopic cross-section generation capability within Griffin would significantly streamline depletion modeling. This improvement would eliminate the current necessity of performing extensive initial depletion calculations using external Monte Carlo codes to generate microscopic cross sections as functions of irradiation time or burnup.
- 3. Fractional removal and fuel feed capabilities in Shift.
Currently, Shift does not support the fractional removal of fission products or the continuous addition of makeup fuel, limiting its direct applicability to molten salt reactor depletion modeling. Future development of these critical features would enhance Shift's capability for MSR analysis.
- 4. Single-region depletion option in Shift.
Shift inherently partitions depleted mixtures according to geometry cells, which complicates modeling depletion in a uniformly mixed, single-region fuel salt as required by MSRs. Therefore, an explicit option in Shift to perform depletion calculations using a single, uniformly mixed depletion region would be beneficial for MSRE depletion.
- 5. Improved microscopic cross-section generation in Shift for trace isotopes:
Shift's current microscopic cross-section generation has limitations, particularly for trace isotopes present at extremely low atomic densities. Specifically, microscopic scattering cross sections for these isotopes are often set to zero but changing this to allow for the tracking of trace isotopes would be an improvement in Shift cross-section generation methodology.

7. REFERENCES

- A. Houtzeel and F. F. Dyer, "A Study of Fission Products in the Molten Salt Reactor Experiment by Gamma Spectrometry," Oak Ridge National Laboratory, ORNL-TM-3151, August 1972.
- A. O. Ige and M. Sibiya, "State-of-the-Art in 1D Convolutional Neural Networks: A Survey," *IEEE Access*, vol. 12, pp. 144082–144105, 2024, doi: <https://doi.org/10.1109/access.2024.3433513>.
- Akner, M. (2021). Validating results from the molten salt reactor experiment by use of turbulent CFD simulations: a study of a modified U-tube shell-and-tube primary heat exchanger and radiator with molten salts.
- Besmann, T. M., & Schorne-Pinto, J. (2021). Developing practical models of complex salts for molten salt reactors. *Thermo*, 1(2), 168-178.
- Besmann, T. M., Schorne-Pinto, J., Aziziha, M., Mofrad, A. M., Booth, R. E., Yingling, J. A., ... & Hartanto, D. (2024). Applications of Thermochemical Modeling in Molten Salt Reactors. *Materials*, 17(2), 495.
- Betzler, B. R. 2021. "Liquid-fueled Molten Salt Reactor Depletion Modeling." Transactions of American Nuclear Society 124, 498-500. <https://doi.org/10.13182/T124-35170>
- Boyd, W., et al. 2019. "Multigroup Cross-Section Generation with the OpenMC Monte Carlo Particle Transport Code." Nuclear Technology 205 (7), 928-944. <https://doi.org/10.1080/00295450.2019.1571828>
- CKópházi, J., et al. 2009. "Development of a Three-Dimensional Time-Dependent Calculation Scheme for Molten Salt Reactors and Validation of the Measurement Data of the Molten Salt Reactor Experiment." Nuclear Science and Engineering 163 (2), 118–131.
- Engel, J. R., and R. C. Steffy. 1971. XENON BEHAVIOR IN THE MOLTEN SALT REACTOR EXPERIMENT. ORNL-TM-3464. United States. <https://doi.org/10.2172/4731186>.
- Engel, J. R., P. N. Haubenreich, and A. Houtzeel. 1969. SPRAY, MIST, BUBBLES, AND FOAM IN THE MOLTEN SALT REACTOR EXPERIMENT. United States. <https://doi.org/10.2172/4086308>.

- F. Pedregosa et al., Scikit-learn: Machine Learning in Python, JMLR 12, pp. 2825-2830, 2011.
- Fischer, P., Kerkemeier, S., Min, M., Lan, Y. H., Phillips, M., Rathnayake, T., ... & Warburton, T. (2022). NekRS, a GPU-accelerated spectral element Navier–Stokes solver. *Parallel Computing*, 114, 102982.
- Frederix, E. M. A., & Komen, E. M. J. (2023). Simulation of noble metal particle growth and removal in the molten salt fast reactor. *Nuclear Engineering and Design*, 415, 112690.
- Freile, R., German, P., & Tano, M. (2025). Evaluating turbulence modeling for thermal–hydraulics analysis of molten salt reactors. *Nuclear Engineering and Design*, 432, 113787.
- Gaston, Derek, Chris Newman, Glen Hansen, and Damien Lebrun-Grandié. 2009. “MOOSE: A Parallel Computational Framework for Coupled Systems of Nonlinear Equations.” *Nuclear Engineering and Design* 239 (10): 1768–78. <https://doi.org/10.1016/j.nucengdes.2009.05.021>.
- Guymon, R. H. 1973. MSRE Systems and Components Performance. United States. <https://doi.org/10.2172/4462915>.
- Hartanto, D., et al. 2023. “Molten Salt Reactor Experiment Simulation Using Shift/Griffin.” ORNL/TM-2023/3005, Oak Ridge National Laboratory, Oak Ridge, TN. <https://doi.org/10.2172/1997706>
- Henderson, S., Agca, C., McMurray, J. W., & Lefebvre, R. A. (2021). *Saline: An api for thermophysical properties* (No. ORNL/TM-2021/2239). Oak Ridge National Laboratory (ORNL), Oak Ridge, TN (United States).
- Hu R., et al. 2021. “FY21 SAM Developments for MSR Modeling.” ANL/NSE-21/74, Argonne National Laboratory, Lemont, IL. <https://doi.org/10.2172/1827965>.
- J. Reis, J. Seo, Y. Hassan; Molten salt flow visualization to characterize boundary layer behavior and heat transfer in a natural circulation loop. *Physics of Fluids* 1 March 2024; 36 (3): 033605. <https://doi.org/10.1063/5.0197276>
- Jaradat, M., & Ortensi, J. (2023). Thermal spectrum molten salt-fueled reactor reference plant model. Idaho National Laboratory, INL/RPT-23-72875 (07 2023).
- Kedl, R J, and A Houtzeel. 1967. DEVELOPMENT OF A MODEL FOR COMPUTING Xe135 MIGRATION IN THE MSRE. ORNL-4069. United States. <https://doi.org/10.2172/4363507>.
- L. M. Mentel, *mendeleev* - A Python resource for properties of chemical elements, ions and isotopes, 2014– . Available at: <https://github.com/lmmentel/mendeleev>.
- L. ZOU et al., “Code Validation of SAM Using Natural-Circulation Experimental Data from the Compact Integral Effects Test (CIET) Facility,” *Nucl. Eng. Des.*, 377, 111144 (2021); <https://doi.org/10.1016/j.nucengdes.2021.111144>;
- Lee, Kyoung O., Matthew A. Jessee, Aaron M. Graham, and David J. Kropaczek. 2024. “Coupled Neutronics and Species Transport Simulation of the Molten Salt Reactor Experiment.” *Nuclear Engineering and Design* 417 (February): 112824. <https://doi.org/10.1016/j.nucengdes.2023.112824>.
- Leppänen, J., et al. 2015. “The Serpent Monte Carlo code: Status, development and applications in 2013.” *Annals of Nuclear Energy* 82, 142-150. <https://doi.org/10.1016/j.anucene.2014.08.024>
- M. S. Sohal , M. A. Ebner , P. Sabharwall , and P. Sharpe , “ Engineering database of liquid salt thermophysical and thermochemical properties,” Technical Report No. INL/EXT-10-18297 (2010).
- Mui, Travis, Daniel J. O’Grady, Ling Zou, Rui Hu, and Robert K. Salko. 2024. SAM Code Improvements for Molten Salt Reactor Transient and Species Transport Modeling. United States. <https://doi.org/10.2172/2467506>.
- N. Termini, A. Birri, S. Henderson, and N. D. Ezell, “An Overview of the Molten Salt Thermal Properties Database—Thermophysical, Version 2.1.1 (MSTDB-TP v.2.1.1),” Jul. 2023, doi: <https://doi.org/10.2172/1988348>.
- Pandya, T. M., et al. 2022. “Two-step neutronics calculations with Shift and Griffin for advanced reactor systems.” *Annals of Nuclear Energy* 173, 109131. <https://doi.org/10.1016/j.anucene.2022.109131>

Pandya, T., et al. 2016. "Implementation, capabilities, and benchmarking of Shift, a massively parallel Monte Carlo radiation transport code." *Journal of Computational Physics* 308 (1), 239-272. <https://doi.org/10.1016/j.jcp.2015.12.037>

Pfahl, P., Jaradat, M. K., Tano, M., Freile, R. O., Walker, S., & Ortensi, J. (2025). Comparison of spatial dynamics and point kinetics approaches in multiphysics modeling of the molten salt reactor experiment. *Frontiers in Nuclear Engineering*, 4, 1617048.

Prince, B. E., Ball, S. J., Engel, J. R., Haubenreich, P. N., & Kerlin, T. W. (1968). ZERO-POWER PHYSICS EXPERIMENTS ON THE MOLTEN-SALT REACTOR EXPERIMENT (No. ORNL-4233). Oak Ridge National Lab.(ORNL), Oak Ridge, TN (United States).

R. Santini, L. Tadrist , J. Pantalone , and P. Cerisier, " Measurement of thermal conductivity of molten salts in the range 100–500 °C," *Int. J. Heat Mass Transfer* 27, 623–626 (1984). [https://doi.org/10.1016/0017-9310\(84\)90034-6](https://doi.org/10.1016/0017-9310(84)90034-6)

Robertson, R C. 1965. MSRE Design & Operations Report Part 1 Description of Reactor Design. United States. <https://doi.org/10.2172/4654707>.

Robertson, R. C. (1965). MSRE design & operations report part 1 description of reactor design (No. ORNL-TM-728). Oak Ridge National Lab.(ORNL), Oak Ridge, TN (United States).

Romano, P., et al. 2015. "OpenMC: A state-of-the-art Monte Carlo code for research and development." *Annals of Nuclear Energy* 82, 90-97. <https://doi.org/10.1016/j.anucene.2014.07.048>

S. Kiranyaz, "1D convolutional neural networks and applications: A survey," *Mechanical Systems and Signal Processing*, vol. 151, p. 107398, Apr. 2021, doi: <https://doi.org/10.1016/j.ymssp.2020.107398>.

S. Shahbazi and T. Fei, "Radiochemical Transport Analysis of Gamma Spectroscopic Data to Support Estimation of Molten Salt Reactor Off-Gas Inventories," *J Radioanal Nucl Chem (accepted)*, 2025.

Salko, Jr., Robert, T. Mui, R. Hu, and E. Merzari. 2021. Implementation of a Drift-Flux Model in SAM for Modeling of Passively Transported GAS in Molten Salt Reactors. United States. <https://doi.org/10.2172/1824950>.

Salko, R. K. Jr., Mui, T., Zou, L., & Hu, R. (2024). Implementation of a Drift Flux Model into SAM with Development of a Verification and Validation Test Suite for Modeling of Non-condensable Gas Mixtures. *Nuclear Technology*. Advance online publication. doi:10.1080/00295450.2024.2370189

T. Porter, M. M. Vaka, P. Steenblik, and D. Della Corte, "Computational methods to simulate molten salt thermophysical properties," *Communications Chemistry*, vol. 5, no. 1, pp. 1–15, Jun. 2022, doi: <https://doi.org/10.1038/s42004-022-00684-6>

Tanaka, R. S. (2017). Quantifying the adhesion of noble metal foulants on structural materials in a Molten Salt Reactor (Doctoral dissertation, Massachusetts Institute of Technology).

Termini, N., et al. 2023. "An Overview of the Molten Salt Thermal Properties Database—Thermophysical, Version 2.1.1 (MSTDB-TP v.2.1.1)." ORNL/TM-2023/2955, Oak Ridge National Laboratory, Oak Ridge, TN. <https://doi.org/10.2172/1988348>

Termini, Nick, Birri, Anthony, Henderson, Shane, & Ezell, N. Dianne Bull (2023). An Overview of the Molten Salt Thermal Properties Database—Thermophysical, Version 2.1.1 (MSTDB-TP v.2.1.1). <https://doi.org/10.2172/1988348>

Thoma, R. E. (1971). Chemical Aspects of MSRE Operations-ORNL-4658. Oak Ridge National Lab, Tenn.

Travis Mui and et. al. 2025. Integrated Molten Salt Reactor Modeling Capabilities in NEAMS Thermal Hydraulics Tools. To be published. Argonne National Laboratory.

Walker, S., et al. 2022. "Implementation of Isotopic Removal Capability in Griffin for Multi-Region MSR Depletion Analysis." *Transactions of American Nuclear Society* 127, 976-979. <https://doi.org/10.13182/T127-39645>

Walter, D., Cisnero, T., Goodrich, S., & Mausolff, Z. (2022). MCRE design description in support of external model development. TerraPower, LLC., MCRE-ENG-PRSNT-0029.

Wang, Y., et al. 2025. "Griffin: A MOOSE-based reactor physics application for multiphysics simulation of advanced nuclear reactors." *Annals of Nuclear Energy* 211, 110917. <https://doi.org/10.1016/j.anucene.2024.110917>

Website: <https://mstdb.ornl.gov/>. Accessed on: September 18, 2025

Wu, Chen, Xiaoquan Li, Jianhui Wu, et al. 2024. "Xenon Behavior Modeling for Molten Salt Reactors by Using Multiple Transport Mechanisms." *Progress in Nuclear Energy* 168 (March): 104987. <https://doi.org/10.1016/j.pnucene.2023.104987>.

Yuan, H., Hoyt, N., Saini, N., Dai, D., Shaver, D., Guo, J., & Lan, Y. H. (2024). MOSCATO Development and Integration in Fiscal Year 2024 (No. ANL/NSE-24/72). Argonne National Laboratory (ANL), Argonne, IL (United States).

Yuan, H., Yildiz, M. A., Merzari, E., Yu, Y., Obabko, A., Botha, G., ... & Nguyen, D. T. (2020). Spectral element applications in complex nuclear reactor geometries: Tet-to-hex meshing. *Nuclear Engineering and design*, 357, 110422.

Page intentionally left blank

